Titre: Title:	Development of a Coupled RANS-Stochastic Lagrangian Particle Model for Contrail Formation
Auteur: Author:	Justin Rigal
Date:	2025
Type:	Mémoire ou thèse / Dissertation or Thesis
Référence: Citation:	Rigal, J. (2025). Development of a Coupled RANS-Stochastic Lagrangian Particle Model for Contrail Formation [Mémoire de maîtrise, Polytechnique Montréal]. PolyPublie. https://publications.polymtl.ca/65815/

URL de PolyPublie: PolyPublie URL:	https://publications.polymtl.ca/65815/
Directeurs de recherche: Advisors:	Roberto Paoli
Programme: Program:	Génie aérospatial

POLYTECHNIQUE MONTRÉAL
affiliée à l'Université de Montréal

Development of a Coupled RANS-Stochastic Lagrangian Particle Model for Contrail Formation

JUSTIN RIGAL
Département de génie mécanique

Mémoire présenté en vue de l'obtention du diplôme de *Maîtrise ès sciences appliquées*
Génie aérospatial

Avril 2025

POLYTECHNIQUE MONTRÉAL
affiliée à l'Université de Montréal

Ce mémoire intitulé :

Development of a Coupled RANS-Stochastic Lagrangian Particle Model for Contrail Formation

présenté par **Justin RIGAL**
en vue de l'obtention du diplôme de *Maîtrise ès sciences appliquées*
a été dûment accepté par le jury d'examen constitué de :

Éric LAURENDEAU, président
Roberto PAOLI, membre et directeur de recherche
Bianca VIGGIANO, membre

DEDICATION

À toutes les personnes qui m'entourent,
vous serez toujours une source d'inspiration pour moi.

To all the people around me,
you will always be a source of inspiration for me.

ACKNOWLEDGEMENTS

I am deeply grateful for the help provided by my supervisor, Prof. Roberto Paoli. I thank him for his daily presence, his passionate interest in the topics we've discussed, but most importantly, for his kindness and patience with me! To a true friend, thank you!

I would also like to thank Prof. Eric Laurandeau for the time he dedicated to helping me understand CFD, as well as the students in his lab where I had the chance to grow: Guillaume, Charles, Simon, Pablo, Vincent, and especially Karim and Baptiste for your patience, your invaluable advice, and especially for all the good times we shared together!

Calculations were performed on Compute Canada/Calcul Quebec clusters.

I would like to acknowledge that the research project in which this master's thesis was carried out is funded by a Safran Aircraft Engine grant through the contract number #YOG-2023-0010, which also provided a team of engineers always available to help.

I am also very grateful to François Camilleri, who accompanied me during my internship at Safran Aircraft Engines in Moissy-Cramayel, as well as to Benedicte Cuenot, Edoardo Paladini, Nicolas Tantot, and Ismail Sekka for their valuable feedback and advice. This period was fascinating and highly appreciated.

Finally, I would like to warmly thank my friends, family, and Agathe, who supported me closely or from afar during my time in Canada and throughout the phases of hard work.

RÉSUMÉ

L'impact environnemental de l'aviation reste une préoccupation majeure, d'autant plus que l'Organisation de l'aviation civile internationale (OACI) prévoit une augmentation de 34% du trafic aérien commercial d'ici 2029 par rapport aux niveaux de 2019. Un facteur clé de cet impact est la formation des traînées de condensation (contrails, contraction de condensation trails en anglais) et des nuages cirrus induits, qui augmentent la couverture nuageuse et constituent l'une des principales sources d'incertitude dans l'effet climatique de l'aviation, potentiellement plus importante que les émissions de CO_2. Comprendre et prédire la formation de ces traînées est essentiel pour évaluer les stratégies d'atténuation possibles. Le régime de jet, qui constitue les premières secondes suivant l'échappement des moteurs et relie la conception de ces derniers à la caractérisation des particules de traînée initiales, est particulièrement pertinent pour les fabricants de moteurs d'avion et constitue le cœur de cette étude.

En raison des coûts élevés et des risques associés aux tests expérimentaux en vol, les simulations numériques sont devenues l'outil principal pour étudier la formation des contrails. Les modèles traditionnels s'appuient sur des descriptions détaillées du champ d'écoulement, de la microphysique et des effets radiatifs, souvent à l'aide de méthodes coûteuses en ressources de calcul, comme les simulations des grandes échelles de turbulence (LES en anglais). Des approches plus récentes, basées sur les équations de Navier-Stokes moyennées (RANS), offrent une plus grande efficacité numérique, mais elles approximent la composition instantanée des gaz entourant les particules et l'influence de celle-ci sur les processus microphysiques en utilisant sa moyenne locale. Cette simplification pourrait négliger l'impact des fluctuations turbulentes, potentiellement cruciales pour une prédiction précise de la formation des traînées. Bien que l'ampleur de l'influence de ces fluctuations ne soit pas encore pleinement évaluée, ce manque de connaissance a motivé le développement d'un nouveau cadre qui, tout en maintenant l'efficacité numérique, capture les effets stochastiques de la turbulence sur la croissance des particules de glace.

Ce travail propose un modèle hybride Stochastique Lagrangien-Eulérien, combinant le modèle simplifié de Langevin (SLM) pour les trajectoire turbulentes des particules couplé à un solveur eulerien des équations RANS ainsi qu'un modèle de turbulence pour les grandeurs moyennes du champ. Le processus de croissance des particules de glace est modélisé à l'aide d'un modèle simplifié de microphysique, où la composition instantanée est suivie le long des lignes de courant grâce au modèle d'échange par interaction avec la moyenne (IEM). Le cadre ainsi

développé offre une description plus précise des effets de la turbulence sur la microphysique sans sacrifier l'efficacité numérique.

Une simulation du jet d'un moteur CFM56-5B3 montre la capacité du modèle à considérer de manière réaliste les variations de trajectoire et de composition des particules. Les résultats mettent en évidence des différences significatives entre le modèle hybride et des versions intermédiaires de celui-ci, confirmant l'intérêt d'étudier les effets de la dispersion turbulente. La sensibilité du modèle à la température atmosphérique, à l'humidité relative sur glace et aux émissions de particules de suie a également été étudiée, montrant un comportement physique cohérent avec les effets attendus sur les traînées induites.

Ces résultats établissent une base pour le développement de modèles hybrides Stochastiques Lagrangiens-Eulériens pour la formation des contrails, en soulignant l'importance de modéliser avec précision les effets de la turbulence et en suggérant des pistes d'amélioration pour les simulations futures. Les recherches à venir se concentreront sur l'incorporation d'une densité de particules variables, sur le raffinement de la microphysique et sur l'extension du modèle pour inclure des configurations complètes d'aéronefs ainsi qu'une meilleure évolutivité. Un domaine clé pour le développement futur sera l'amélioration du modèle Lagrangien des particules, en particulier du modèle de mélange et du taux de relaxation de la turbulence prédit par le modèle $k - \omega$ SST. L'amélioration de ces aspects contribuera à accroître la précision et la fiabilité des résultats. À terme, cette approche pourrait améliorer significativement les cadres de simulation existants et fournir des évaluations plus précises de l'impact climatique de l'aviation.

ABSTRACT

The environmental and climatic impact of aviation remains a significant concern, with the International Civil Aviation Organization (ICAO) projecting a 34% increase in commercial air traffic by 2029 compared to the levels of 2019. A key factor contributing to this impact is the formation of contrails and contrail-induced cirrus clouds, which increase cloud coverage and are considered one of the largest sources of uncertainty in the aviation climate effect, potentially surpassing CO_2 emissions. Understanding and predicting contrail formation is essential for evaluating potential mitigation strategies. The jet regime, which occurs within seconds after engine exhaust and links engine design to early contrail particle formation, is particularly relevant for aircraft engine manufacturers and is the focus of this study.

Given the high costs and risks associated with in-flight experimental tests, numerical simulations have become the primary tool for studying contrail formation. Traditional models rely on detailed descriptions of the flow field, microphysics, and radiative effects, often using computationally expensive methods such as LES. More recent approaches based on Reynolds-averaged Navier–Stokes (RANS) equations offer greater computational efficiency but approximate the instantaneous gas composition surrounding particles and their effects on microphysical processes using their averaged counterparts. This approximation may overlook the impact of turbulent fluctuations, which could be critical for accurate contrail formation predictions. Although the degree of influence of these fluctuations is not yet fully assessed, this knowledge gap has led to the development of a new framework that, while maintaining computational efficiency, captures the stochastic effects of turbulence on the growth of ice particles.

This work introduces a hybrid Stochastic Lagrangian-Eulerian model, combining the Simplified Langevin Model for turbulence-induced particle trajectory variations with a RANS-based turbulence model to compute mean field quantities. The ice growth process is modeled using a simplified microphysical model, with instantaneous composition tracked along streamlines using the Interaction by Exchange with the Mean (IEM) mixing model. The resulting framework offers a more precise description of turbulence effects on microphysics without sacrificing computational efficiency.

A simulation of a CFM56-5B3 plume demonstrates the model's ability to realistically represent particle trajectory and composition variations. The results highlight significant differences between the hybrid model and intermediate versions, reinforcing the value of studying turbulence dispersion effects. The model sensitivity to atmospheric temperature, relative

humidity over ice, and soot particle emissions was also assessed, showing consistent physical behavior in line with expected contrail evolution patterns.

These findings establish a baseline for developing hybrid Stochastic Lagrangian-Eulerian models for contrail formation, emphasizing the importance of accurately modeling turbulence effects and suggesting areas for improvement in future simulations. Future research will focus on incorporating varying particle density, refining microphysics, and extending the model to include full aircraft configurations and enhanced scalability. A key area for further development will involve refining the turbulence trajectory model, particularly the mixing model and the turbulence relaxation rate as predicted by the $k - \omega$ SST model. Addressing these areas will improve the accuracy and reliability of the results. Ultimately, this approach has the potential to enhance current contrail simulation frameworks and provide more accurate assessments of the climatic impact of aviation.

TABLE OF CONTENTS

DEDICATION iii

ACKNOWLEDGEMENTS iv

RÉSUMÉ v

ABSTRACT vii

LIST OF TABLES xii

LIST OF FIGURES xiii

LIST OF SYMBOLS AND ACRONYMS xvi

CHAPTER 1 INTRODUCTION 1
1.1 Context 1
1.1.1 Climate Impact of Aviation 1
1.2 Theoretical and Research Framework 3
1.2.1 Impact of Atmospheric Conditions 3
1.2.2 Regimes of Evolution 4
1.3 Problem Statement 6
1.4 Research Objectives 7
1.5 Thesis Outline 7

CHAPTER 2 LITERATURE REVIEW 9
2.1 Physics of Contrails 9
2.1.1 Particle Motion 9
2.1.2 Ice Growth Rate 10
2.1.3 Nucleation 14
2.2 Numerical Approaches 14
2.2.1 Airflow 14
2.2.2 Particles Phase 15
2.3 Experimental Data 16

CHAPTER 3 NUMERICAL MODELING 17
3.1 Proposed Multi-Physics Numerical Integration 17
3.1.1 Monte Carlo Approach 17

3.2 Airflow Governing Equations . . . 18
3.2.1 Reynolds Averaged Navier Stokes . . . 19
3.2.2 Stochastic Differential Equation . . . 21
3.2.3 Differences Between Approaches . . . 28
3.2.4 Coupling with Mean Equation . . . 28
3.3 Numerical Implementation . . . 29
3.3.1 CHAMPS Software . . . 29
3.3.2 Lagrangian Implementation . . . 29
3.3.3 Contrail Simulation Procedure . . . 37
3.3.4 Parallel Processing . . . 38
3.4 Verification Tests . . . 39
3.4.1 Verification of the Gas-Phase RANS Solver . . . 39
3.4.2 Verification of the Species Transport Solver . . . 40

CHAPTER 4 CONTRAIL RESULTS . . . 44
4.1 Airflow Simulation of a CFM56-5B3 Plume . . . 44
4.1.1 Atmospheric Conditions . . . 44
4.1.2 Engine Operating Point . . . 45
4.1.3 Computational Domain . . . 46
4.1.4 Convergence Strategy and Numerical Stabilization . . . 49
4.1.5 Calibrated Airflow Results . . . 49
4.2 Base Case Exhaust Composition and Ambient Vapor Conditions . . . 50
4.2.1 Freestream Vapor Mass Fraction . . . 50
4.2.2 In-Flight Exhaust Composition . . . 51
4.3 Models Comparison . . . 53
4.3.1 Mean Velocity - Mean Composition . . . 54
4.3.2 Turbulent Velocity - Mean Composition . . . 57
4.3.3 Turbulent Velocity - Turbulent Composition . . . 61
4.4 Sensitivity Studies . . . 68
4.4.1 Cases Properties . . . 68
4.4.2 Soot Particles Emission Rate . . . 68
4.4.3 Atmospheric Relative Humidity . . . 71
4.4.4 Atmospheric Temperature . . . 72
4.4.5 Side-by-Side Comparison . . . 74

CHAPTER 5 CONCLUSION . . . 76
5.1 Summary of Works . . . 76

5.2 Limitations 77
5.3 Future Research 78

REFERENCES 79

LIST OF TABLES

Table 3.1	Interpolation method at particle position for each Eulerian field	30
Table 3.2	L2 error norms and convergence rates for species transport MMS test case	41
Table 4.1	Gas-phase : Freestream Conditions and Characteristic Numbers for the Simulation	45
Table 4.2	Gas-phase : Nozzle boundary and exhaust conditions for the CFM56-5B3 engine	45
Table 4.3	Contrail base-case : Exhaust Composition and Ambient Vapor Conditions	53
Table 4.4	Sensitivity studies cases : key parameters variations	68
Table 4.5	Sensitivity studies cases : engine operating point related parameters variations	69

LIST OF FIGURES

Figure 1.1 Radiative forcing from global aviation emissions. 2

Figure 1.2 Temperature-Water vapor pressure diagrams. a) Contrasting scenarios illustrating contrail formation and non-formation, b) depiction of a persistent contrail scenario 4

Figure 1.3 Classification of aircraft wake evolution into four regimes. 5

Figure 3.1 Workflow of the proposed contrail model 18

Figure 3.2 Computational particles seeding plane in the engine's core nozzle . . 31

Figure 3.3 a) Quadtree subdivision in 3 levels. b) Example of a 2D unstructured mesh storage in a 3 levels quadtree 32

Figure 3.4 Particle tracking : a) Find the element containing position Q_{n+1} given that position Q_n was known to be located in element e_1. b) Wall treatment. c) Periodicity treatment. 33

Figure 3.5 Parrallel data structure, showing the distribution of zones, particles, data zones, and statistical buffers across cores in multiple nodes. . . . 39

Figure 3.6 Comparison of CHAMPS and WIND. 42

Figure 3.7 Species transport MMS verification, from top to bottom : 6171, 41921 and 312667 3D elements. Left : 2D contour plots of $y_1(x, y, z = 0.5)$ for different mesh resolutions. Right : 1D centerline profiles of $y_1(x, y = 0.5, z = 0.5)$ compared with the exact solution. 43

Figure 4.1 Reconstructed aerodynamic profiles of the bypass and core nozzles from the CFM56-5B3. a) side view, b) isometric view with the 360 geometry for reference 46

Figure 4.2 Overview of the computational domain and boundary conditions. a) Full domain and buffer zones, b) Zoom on turbofan 47

Figure 4.3 Overview of the computational mesh. a) Side view of the full domain, b) Isometric view, c) Side view zoomed in on the turbofan, d) Rear view of the diamond-like mesh structure around the core plug. 48

Figure 4.4 Mean flow contours of : a) axial velocity, b) pressure, c) temperature 50

Figure 4.5 Normalized axial velocity profiles at various downstream locations. The dashed triangles indicate the extent of the primary and secondary potential cores. 51

Figure 4.6 Reconstructed trajectories of 40 particles seeded in the core following the mean velocity. Rotation is accounted for by tracking periodic boundary crossings with an initial offset. Colors distinguish individual trajectories. 55
Figure 4.7 Mean velocity - Mean composition model : Spatial distribution of particles, colored by crystal radius. a) Side view, b) Cross-sectional distribution 56
Figure 4.8 Mean velocity - Mean composition model : a) Evolution of the mean particle radius alongside mean saturation ratio over liquid water and over ice. b) Scatter plot of particles colored by life time in the thermodynamic diagram $T - p_{\mathrm{v}}$ 56
Figure 4.9 Contour plot of the model coefficient C_0 computed with equation (3.49) 57
Figure 4.10 Reconstructed trajectories of 40 particles seeded in the core nozzle following the velocity generated by the Langevin equation. a) Isometric view, b) View from behind. Rotation is accounted for by tracking periodic boundary crossings with an initial offset. Colors distinguish individual trajectories. 58
Figure 4.11 Comparison between RANS solver quantities and Eulerian particle statistics from the Langevin model. (a) Axial velocity normalized by the core nozzle excess velocity. (b) Turbulent kinetic energy normalized by the square of the freestream velocity. 59
Figure 4.12 Turbulent velocity - Mean composition model : Spatial distribution of particles, colored by crystal radius. a) Side view, b) Cross-sectional distribution 59
Figure 4.13 Turbulent velocity - Mean composition model : a) Evolution of the mean particle radius alongside mean saturation ratio over liquid water and over ice. b) Scatter plot of particles colored by life time in the thermodynamic diagram $T - p_{\mathrm{v}}$ 60
Figure 4.14 Turbulent velocity - Turbulent composition model : Spatial distribution of particles, colored by crystal radius. a) Side view, b) Cross-sectional distribution 62
Figure 4.15 Turbulent velocity - Turbulent composition model : a) Evolution of the mean particle radius alongside mean saturation ratio over liquid water and over ice. b) Scatter plot of particles colored by life time in the thermodynamic diagram $T - p_{\mathrm{v}}$ 63

Figure 4.16 Turbulent velocity - Turbulent composition model : Probability density function of particle radii at several downstream locations 64
Figure 4.17 Spatial distribution of particles, colored by crystal radius. a) Mean Velocity - Mean composition b) Turbulent Velocity - Mean composition, c) Turbulent Velocity - Turbulent composition, d) Cross-sectional distribution at x=220m 65
Figure 4.18 Comparison of the number of activated particles evolution for the three models 66
Figure 4.19 Comparison of the mean particle radius evolution for the three models 67
Figure 4.20 Dependence of contrail particle mean radius on soot particle emission rate at x=120m and x=220m. Cases S1, Ref and S2 70
Figure 4.21 Dependence of total ice mass flux on soot particle emission rate at x=120m and x=220m. Cases S1, Ref and S2 70
Figure 4.22 Dependence of contrail particle mean radius on freestream relative humidity over ice (RHI) at x=120m and x=220m. Cases R1, Ref and R2 71
Figure 4.23 Dependence of total ice mass flux on freestream relative humidity over ice (RHI) at x=120m and x=220m. Cases R1, Ref and R2 72
Figure 4.24 Dependence of contrail particle mean radius on freestream temperature at x=120m and x=220m. Cases T1, Ref and T2 73
Figure 4.25 Dependence of total ice mass flux on freestream temperature at x=120m and x=220m. Cases T1, Ref and T2 73
Figure 4.26 Side-by-side comparison of the mean contrail particle radius dependence on the three key parameters. 74
Figure 4.27 Side-by-side comparison of the total ice mass flux dependence on the three key parameters. 75

LIST OF SYMBOLS AND ACRONYMS

Symbols

C_D	Drag coefficient	-
C_0	Langevin model coefficient	-
$\mathcal{C}_0$	Universal Kolmogorov constant	-
C_ϕ	IEM model constant	-
c_p	Specific heat at constant pressure	J kg^{-1} K^{-1}
D	Molecular diffusivity	m^2 s^{-1}
$D_{\mathrm{bp}}, D_{\mathrm{core}}$	Bypass and core nozzle diameters	m
d_{v}	Collision diameter of vapor	m
dW	Wiener process	-
$\mathrm{EI}_n, \mathrm{EI}_m$	Number and mass Emission index	#/kg, kg kg^{-1}
e	Internal energy per unit mass	J kg^{-1}
$F_{\mathrm{v,I}}, F_{\mathrm{h,I}}$	Ventilation factors	-
G	Langevin model relaxation rate	s^{-1}
$\boldsymbol{I}_j$	Position vector of the j-th intersection encountered	m
Kn	Knudsen number	-
k	Turbulent kinetic energy	m^2 s^{-2}
k_B	Boltzmann's constant	J K^{-1}
L_I	Latent heat of sublimation per mol	J mol^{-1}
L_s	Latent heat of sublimation per unit of mass	J kg^{-1}
Ma	Mach number	-
M_m	Molar mass of species m	kg mol^{-1}
m	Mass	kg
$\overline{m_{\mathrm{a}}}$	Average mass of one air molecule	kg
N_A	Avogadro's number	mol^{-1}
$N_\#$	number of physical particles per computational particle	-
n	Number of moles	mol
P	Turbulence production term	kg m^{-1} s^{-3}
P_k	Production term of kinetic turbulent energy	J m^{-3} s^{-1}
Pr	Prandtl number	-
p	Pressure	Pa
R	Specific gas constant	J K^{-1} kg^{-1}

$\mathcal{R}$	Universal gas constant	J mol^{-1} K^{-1}
Re	Reynolds number	-
Re_λ	Taylor scale Reynolds number	-
RHI	Relative humidity over ice	%
r	Radius	m
Sc	Schmidt number	-
$S_{\text{comp}}, S_{\text{phys}}$	Computation and physical particles emission rate	#/s
S_m	Source term of species m	kg m^{-3} s^{-1}
T	Temperature	K
T'_j	Turbulent kinetic energy transport flux	kg s^{-3}
T_L	Integral time scale	s
t	Time	s
U_{rel}	Norm of the relative velocity of a particle	m s^{-1}
$\mathbf{u}$	Velocity vector	m s^{-1}
u_i	Velocity component in i-direction	m s^{-1}
v_{h}	Thermal speed of an air molecule	m s^{-1}
$\mathbf{x}$	Position vector of a particle	m
x_i	Position component in i-direction of a particle	m
$x_{\text{v}}, x_{\text{h}}$	Arguments of ventilation factors	-
y^+	Non dimensional wall coordinate	-
y_m	Mass ratio of species m	-

Greek Symbols

α	Accomodation coefficient	-
β^*	$k-\omega$ SST constant	-
χ	Crystal electrical capacitance	m
Δt	Numerical timestep	s
δ_{ij}	Kronecker symbol	-
ε	rate of turbulent energy dissipation	m^2 s^{-3}
γ_{CFL}	Timestep coefficient	-
κ	Thermal conductivity	J m^{-1} s^{-1} K^{-1}
$\lambda_{\text{v}}, \lambda_{\text{h}}$	Mean free path	m
μ	Dynamic viscosity	kg m^{-1} s^{-1}
ν	Kinematic viscosity	m^2 s^{-1}
Ω	Vorticity magnitude	s^{-1}

ω	rate of dissipation per unit of turbulent kinetic energy	s^{-1}
ω_v, ω_h	Collision and Sticking factors	-
ϕ	Generic scalar variable	-
ρ	Density	kg m^{-3}
σ	Surface tension	J m^{-2}
τ_D	Drag relaxation timescale	s
$\tau_{i,j}$	Viscous stress tensor component	$kg\,m^{-1}\,s^{-2}$
$\tau_{t_{i,j}}$	Reynolds stress tensor component	$kg\,m^{-1}\,s^{-2}$

Subscripts

a	Air
bp	Bypass nozzle
c	Crystal
core	Core nozzle
dry	Dry air
h	Thermal
I	Ice
liq	Liquid
m	Generic composition variable
soot	Soot particles
t	Turbulent
tot	Total pressure or temperature
v	Vapor
∞	Freestream

Superscripts

†	Corrected value
$'$	Fluctuating part of Reynolds decomposition
$''$	Fluctuating part of Favre decomposition
sat	Saturation condition
n	Iteration n

Operators

$\bar{\cdot}$	Reynolds or Ensemble averaged mean value
$\tilde{\cdot}$	Favre averaged mean value

Acronyms

CFD	Computational Fluid Dynamics
CHAMPS	CHApel Multi-Physics Simulation
DLR	Deutsches Zentrum für Luft- und Raumfahrt
ICAO	International Civil Aviation Organization
IEM	Interaction by Exchange with the Mean
MMS	Method of manufactured solutions
NASA	National Aeronautics and Space Administration
nvPM	Non-volatile particle matter
PDF	Probability Density Function
RANS	Reynolds Averaged Navier-Stokes
RF	Radiative Forcing
SAF	Sustainable Aviation Fuel
SFD	Selective Frequency Damping
UTLS	Upper troposphere and lower stratosphere
vPM	Volatile particle matter

CHAPTER 1 INTRODUCTION

1.1 Context

Long-haul flights spend extended periods in the upper troposphere and lower stratosphere (UTLS). Since aircraft engines release gases such as carbon dioxide and nitrogen oxides, along with particulate matter like soot, they alter the UTLS's low background concentrations, influencing the Earth's radiation balance [1]. Under specific atmospheric conditions, these emissions also lead to the formation of condensation trails (contrails), which are line-shaped ice clouds that can persist and contribute to increased cloud coverage.

1.1.1 Climate Impact of Aviation

With commercial air traffic projected to grow by 34% by 2029 compared to 2019 levels [2], concerns over its environmental and climatic impact remain pressing for scientists and policymakers [1, 3].

Aviation contribution to climate change is often assessed using radiative forcing (RF), which measures the net change in radiative flux due to alterations in atmospheric composition [1]. According to Lee et al. [3], aviation accounts for 2–14% of total anthropogenic RF (with 90% confidence). Figure 1.1 details the breakdown of RF contributions from global aviation emissions. Notably, it highlights that contrail-induced cirrus clouds represent the largest source of uncertainty in aviation climate impact, surpassing the combined estimation of all other factors. A similar conclusion was drawn by Paoli [1] based on an earlier version of this figure presented in Lee et al. [3].

These uncertainties have driven extensive research efforts into contrail formation and climate effects over the past two decades. Large-scale initiatives, such as the European Commission's QUANTIFY project (2005–2010) and the Federal Aviation Administration's ACCRI program (2010–2014), have been dedicated to improving contrail modeling and observations [1]. Ongoing investigations continue under projects like ECLIF3 (Emission and Climate Impact of Alternative Fuels), a collaboration involving the Deutsches Zentrum für Luft- und Raumfahrt (DLR), the National Aeronautics and Space Administration (NASA), and several industry partners, focusing on the in-flight study of exhaust and contrail characteristics [5].

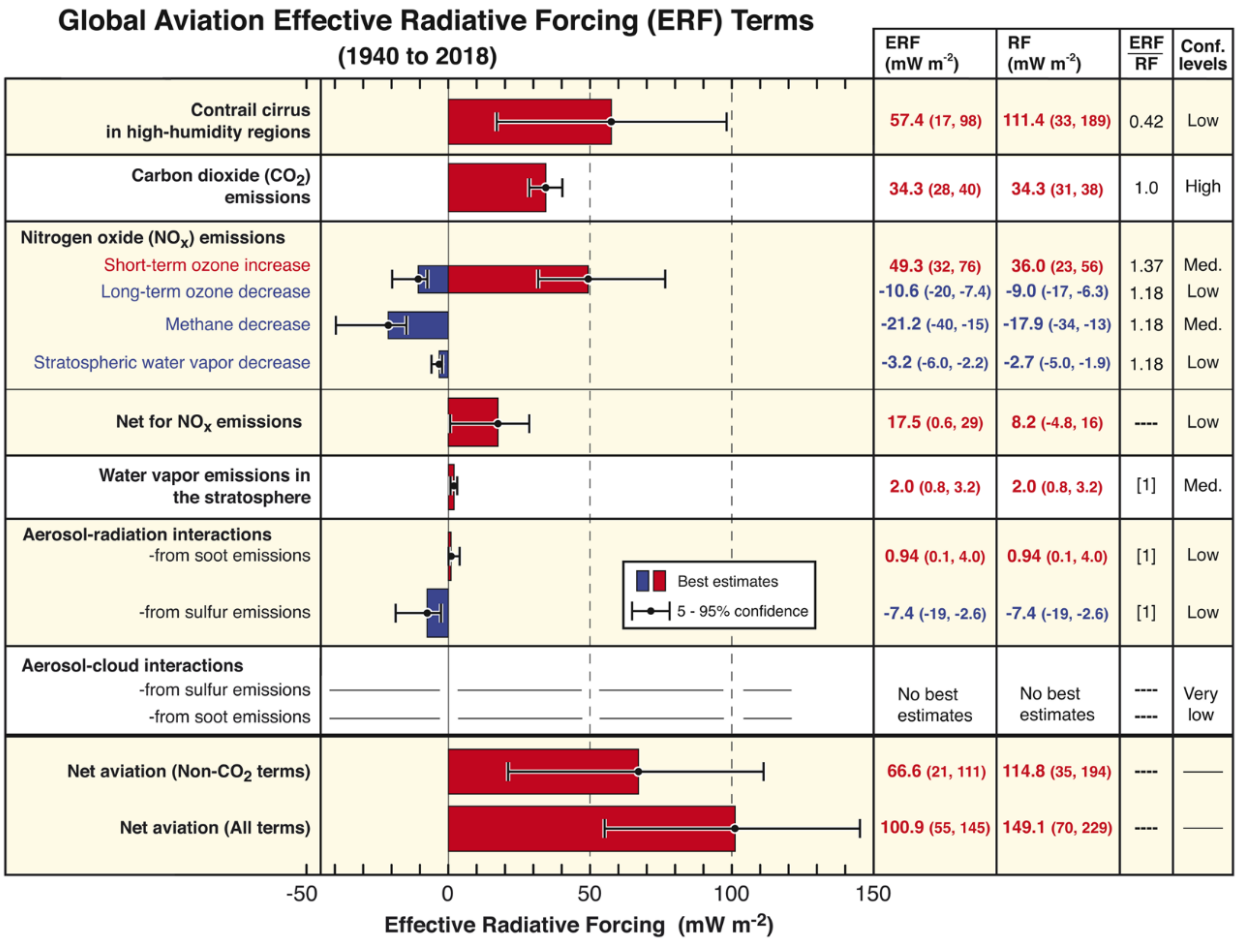

Figure 1.1 Radiative forcing from global aviation emissions. Figure adapted from Lee et al. [4] licensed under CC BY-NC 3.0

Mitigation Strategies

Efforts to mitigate aviation climate impact have primarily focused on reducing CO_2 emissions. A key strategy has been the introduction of Sustainable Aviation Fuels (SAF), which are produced from organic waste. Unlike fossil fuels, the CO_2 released from SAF combustion was first absorbed by plants, making SAF a more sustainable alternative.

However, non-CO_2 effects, particularly contrails, represent a major factor in aviation overall climate impact [4]. Addressing these effects complicates mitigation strategies, as reducing one type of emission may exacerbate another. In the case of SAF, however, their lower aromatic content not only reduces CO_2 emissions but also helps mitigate contrail formation by decreasing particulate matter in engine exhaust [6]. This dual benefit highlights a favorable outcome, though not all mitigation strategies yield such positive results. Some efforts can

involve trade-offs, where reducing one impact unintentionally worsens another.

Another strategy focuses directly on contrail prevention, with navigational avoidance of persistent contrails emerging as a promising approach. This method involves rerouting aircraft to bypass atmospheric regions where contrails are likely to persist (as discussed in Section 1.2.1). However, this comes with trade-offs: rerouting increases CO_2 emissions by forcing aircraft onto less efficient flight paths. Additionally, due to uncertainties in contrail formation predictions, rerouting could sometimes be ineffective—either because a contrail still forms on the new route or because a contrail would not have formed on the original route [4].

These challenges highlight the complex interdependencies between different mitigation strategies. Any approach aimed at reducing aviation climate impact must consider its effects on all emissions to avoid unintended consequences. This underscores the need for accurate predictive models to evaluate trade-offs effectively. Moreover, efficient computational tools are essential to ensure that predictive models can be easily employed to assess the impact of new strategies, even for emissions beyond contrails.

Finally, contrail-induced climate effects remain highly uncertain, as illustrated in Figure 1.1. Given these uncertainties, improving the accuracy of contrail prediction models is crucial for enabling informed and effective climate mitigation strategies.

1.2 Theoretical and Research Framework

1.2.1 Impact of Atmospheric Conditions

Contrail formation is highly sensitive to atmospheric conditions, particularly the surrounding temperature, pressure, and water vapor content. The growth of ice crystals in the contrail plume is governed by the ambient temperature and the saturation vapor pressures over liquid and ice. The following explains the basic growth mechanism, the initial trigger, and the persistency condition.

Growth Mechanism of Ice Crystals The growth of ice crystals in contrails is primarily driven by the deposition of water vapor on their surfaces. This process begins when the vapor pressure p_v exceeds the saturation vapor pressure over liquid water $p_{\mathrm{v,liq}}^{\mathrm{sat}}$. t this point, condensation occurs, and due to the lower vapor pressure over ice, freezing occurs almost immediately. Once the ice forms, the crystal continues to grow as long as p_v exceeds the saturation vapor pressure over ice, $p_{\mathrm{v,I}}^{\mathrm{sat}}$. Once p_v drops below $p_{\mathrm{v,I}}^{\mathrm{sat}}$, the ice crystals begin to sublimate, releasing water vapor back into the atmosphere.

The Schmidt-Appleman Criterion The Schmidt-Appleman, defined in [1] and reference therein, provides a necessary condition for the formation of contrails based on atmospheric conditions. Assuming a straight mixing line between the exhaust conditions and atmospheric conditions, it states that contrail formation will occur only if the mixing line presents a point where the water vapor is supersaturated with respect to liquid water. Figure 1.2 a) shows two scenarios, one in which a contrail forms and one where it does not.

Persistency Condition Additionally the described growth mechanism allows one to derive a criterion for which the induced contrail persists, which may eventually lead to cirrus formation. Since a partial pressure drop under the saturation pressure over ice triggers sublimation, the persistency condition requires that the ambient conditions maintain a saturation vapor pressure over ice : $p_{\mathrm{v},\infty} > p_{\mathrm{v,I}}^{\mathrm{sat}}(T_\infty)$. Regions of the atmosphere that satisfy this condition are referred to as ice supersaturated regions [1]. A persistent contrail configuration is depicted in Figure 1.2 b).

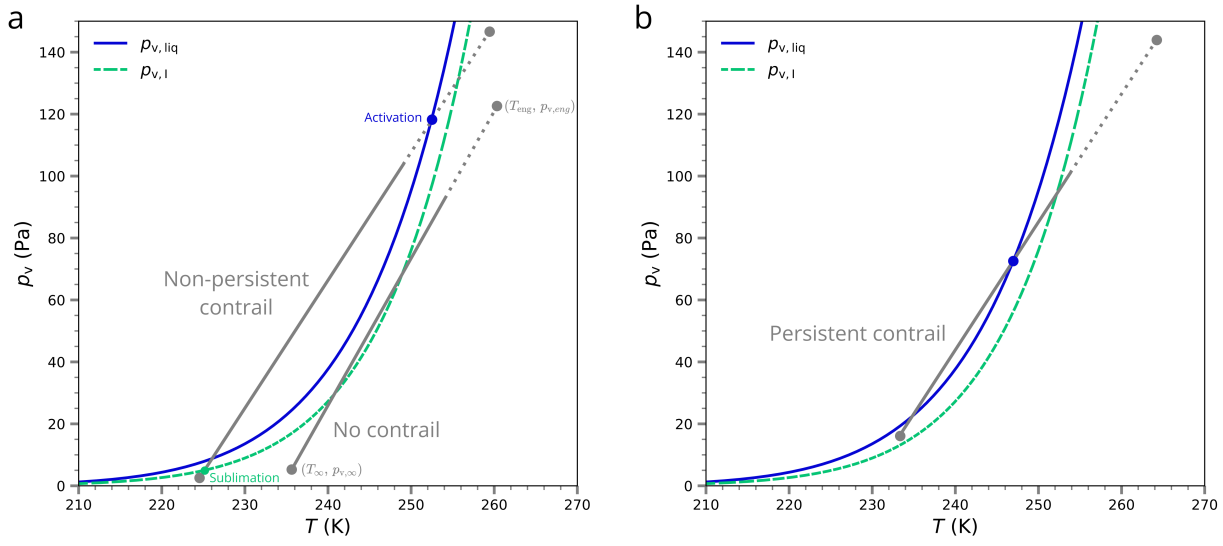

Figure 1.2 Temperature-Water vapor pressure diagrams. a) Contrasting scenarios illustrating contrail formation and non-formation, b) depiction of a persistent contrail scenario

1.2.2 Regimes of Evolution

Predicting the radiative forcing (RF) of aircraft-induced cloudiness presents significant challenges due to the wide range of time and space scales involved, as well as the varying physical mechanisms that dominate at each stage of contrail evolution. The aircraft wake evolution

can be classified into four distinct regimes: the jet regime, vortex regime, dissipation regime, and diffusion regime as presented in [1] and references therein.

In the jet regime, which occurs within the first few seconds after emission, microphysical phenomena such as ice nucleation and complex aerodynamic effects associated with the engine geometry dominate. The timescale for this phase is very short, lasting just a few seconds, and spans a distance of several wingspans. During the vortex regime, lasting from seconds to minutes, aerodynamic effects from the wingtip vortices interacting with the jet plume create a complex flow structure, extending the domain to hundreds of meters. Some studies extend their computational domains to include the initial stages of the vortex regime, as the interaction between the vortex and exhaust plume has important implications for contrail formation [7, 8]. As the wake enters the dissipation regime, which spans several minutes to hours, the vortex structures begin to disintegrate, and ice crystals are released into the surrounding atmosphere, where they sublimate or mix with the air. Finally, in the diffusion regime, which occurs over hours and spans much larger spatial scales (up to global scales), the contrail is influenced by atmospheric turbulence, radiative processes, and wind shear. This regime governs the horizontal and vertical spreading of the contrail and may result in the formation of cirrus clouds, contributing to long-term climate effects. Figure 1.3 illustrates these four regimes.

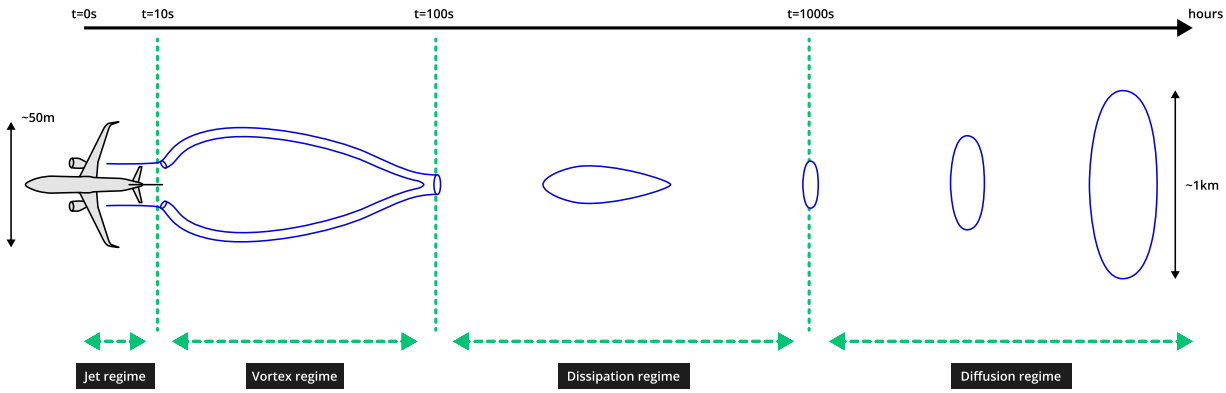

Figure 1.3 Classification of aircraft wake evolution into four regimes [1]

Given the vast differences in time and spatial scales, as well as the varying physical processes that dominate in each regime, it is clear that numerical simulations and experimental research must be split across these stages. A single model cannot adequately capture the full complexity of contrail formation and its subsequent evolution. As such, each regime must be modeled separately.

The present work focuses on the jet regime, which is particularly relevant for aircraft engine manufacturers. This regime allows for the linkage between engine design and the foundational conditions that influence the subsequent phases of contrail evolution.

1.3 Problem Statement

Contrail research has a long history, yet the climate impact of contrails remains imperfectly assessed [4]. While current mitigation strategies for aviation global impact primarily target other emission sources, some strategies—such as burning at lower temperatures to reduce pollutants, as seen in engines like the CFM LEAP [9]—can have an unexpected consequence: they may actually lead to increased contrail formation. In this case, lower soot emissions, which were once believed to always reduce contrail formation, can instead create conditions that enhance contrail persistence and coverage [10]. This paradox underscores the crucial need to deepen our understanding of contrail formation mechanisms. As industrial partners like Safran work to assess fleet impacts, simplified contrail prediction models based on routine flight data (e.g., meteorological measurements along flight routes) are becoming increasingly essential. These models rely on extensive simulation datasets to robustly interpolate contrail properties and accurately assess fleet-related impacts.

Experimental in-flight tests are rarely conducted due to the high costs and safety risks associated with formation flights [1]. Consequently, numerical simulation has become the main tool for flight-induced contrail research, despite the invaluable insights provided by limited experimental campaigns. Traditionally, contrail modeling has involved detailed descriptions of the flow field, particle trajectories, microphysics (including ice growth and chemistry), and sometimes radiative effects, often employing costly LES or hyper-detailed microphysical schemes. More recently, RANS-based approaches [7, 11] have been proposed to facilitate contrail emission analyzes and enable engineering design studies, such as investigating the nozzle chevron effect [12]. Although computationally efficient, these approaches must accurately capture the effects of turbulence on nonlinear microphysical processes of ice growth, effects that were previously resolved with higher fidelity in more detailed models [13].

In Section 1.2.1, we observed that the activation of the growth of ice particles is highly non-linear, with contrail formation triggered only when ambient conditions exceed a critical threshold. This type of nonlinearities in microphysical processes, combined with the dispersion of gas-phase properties induced by turbulence, calls for a fine-scale description of the carrier phase. Moreover, aerodynamical factors—such as plume and wake interactions (e.g., jet-vortex interactions [13, 14])—further motivate the inclusion of detailed geometries in simulations.

These two objectives—capturing fine-scale turbulence effects on microphysics and accounting for aerodynamical factors such as plume-wake interactions—have often been in conflict. In many studies, one aspect has been prioritized over the other, either by simplifying turbulence effects to focus on geometry or by incorporating aerodynamic influences through predefined inputs or separate simulations. Although the latter approach allows for some representation of aerodynamic effects, it lacks the flexibility to account for changes in geometry within a unified simulation framework. Bridging this gap remains a key challenge in contrail modeling, as both elements are crucial to accurately predict contrail formation and evolution.

1.4 Research Objectives

To provide the most precise input for later analyses, jet-regime contrail simulations must incorporate essential ice crystal growth mechanisms. This research presents a first version of a hybrid framework to assess the potential benefits of a stochastic approach. The goal is to maintain computational efficiency while including a more detailed representation of turbulence effects on a simplified model of ice growth. The specific objectives are :

1. Develop a hybrid Stochastic Lagrangian-Eulerian model for ice particle growth.
2. Demonstrate the model ability to capture key microphysical complexities while maintaining computational feasibility.
3. Evaluate the model ability to assess sensitivity to varying physical conditions.

Stochastic models [15] have been widely applied to reactive flows, such as flame ignition [16–18], and a similar RANS-Langevin framework has been explored to model particle residence times in cavities, albeit in a one-way coupling approach without reaction effects [19].

1.5 Thesis Outline

Chapter 2 provides a literature review of the physical phenomena governing contrail evolution, along with existing alternatives to numerical modeling, including LES, RANS, and both Lagrangian and Eulerian particle-phase approaches. It also briefly introduces the available experimental data. Chapter 3 presents a novel contrail modeling framework that combines the advantages of Finite Volume RANS with a Stochastic Lagrangian approach using Monte Carlo methods, highlighting key challenges in its implementation. Chapter 4 discusses the results, first comparing the proposed approach with the conventional RANS/Streamtrace Lagrangian method, followed by a sensitivity analysis under various physical conditions. Finally, Chapter

5 concludes the thesis by summarizing key findings, outlining the limitations of the method, and providing recommendations for future research.

CHAPTER 2 LITERATURE REVIEW

2.1 Physics of Contrails

2.1.1 Particle Motion

As said before, a contrail is made of a great amount of physical particles (approximately $10^{11}\,\#\,\mathrm{m}^{-3}$ at engine nozzle under cruise conditions according to [20]) first evolving in the wake of the aircraft and later in atmospheric winds. This particularity makes the study of contrails a multiphase problem. An initial study of the equations governing the movement of a particle [1] described by x_i^P and u_i^P, its position and velocity in i-direction, respectively, helps simplifying this aspect for jet regime simulations. These equations are initially

$$\frac{\mathrm{d}x_i^P}{\mathrm{d}t} = u_i^P \tag{2.1}$$

$$m\frac{\mathrm{d}u_i^P}{\mathrm{d}t} = C_D(Re)\frac{1}{2}\rho_\mathrm{a}\pi r^2 U_\mathrm{rel}u_{\mathrm{rel},i} + mg_i \tag{2.2}$$

where m, r and $u_{\mathrm{rel},i} = u_i - u_{\mathrm{a},i}^P$ are its mass, radius and relative velocity to air in i-direction, respectively. $C_D(Re)$ the drag coefficient as a function of the Reynolds number defined by $Re = \frac{\rho_\mathrm{a}U_\mathrm{rel}2r}{\mu}$, ρ_a the air density, U_{rel} the norm of $u_{\mathrm{rel},i}$ and μ the dynamic viscosity. Finally g_i denotes gravitational acceleration component in i-direction.

For small Reynolds values, $Re \ll 1$, drag coefficient is given by $C_D(Re) = 24/Re$ inducing (2.2) to simplify to

$$\frac{\mathrm{d}u_i^P}{\mathrm{d}t} = \tau_D^{-1}\left(u_i^P - u_{\mathrm{a},i}\right) = g_i \tag{2.3}$$

where

$$\tau_D = \frac{m}{6\pi\mu r} \tag{2.4}$$

is the timescale for the particle velocity to relax to the air velocity because of drag.

In the case of spherical ice crystals, this time simplifies to

$$\tau_D = \frac{\rho_I 4/3\pi r^3}{6\pi\mu r} = \frac{\rho_I 2r^2}{9\mu} \tag{2.5}$$

with ρ_I the ice density.

Similarly to [20–22] and using a radius of 1 µm which they agree to be a maximum for the jet regime, we estimate τ_D to be lower than 2×10^{-5} s which is negligible compared to the flow characteristic time. Thus we will consider the particles to have the velocity of the carrier phase. The movement of the contrail particles is described by

$$\begin{aligned} u_i^P &= u_{\mathrm{a},i} \\ \frac{\mathrm{d}x_i^P}{\mathrm{d}t} &= u_i^P \end{aligned} \tag{2.6}$$

From this point forward, the superscript P is omitted unless necessary to avoid ambiguity.

2.1.2 Ice Growth Rate

In order to assess the initial growth criterion as described in Section 1.2.1 the following fit for temperatures T between 123 K and 332 K, giving the saturation pressure over liquid water in Pa for T in K, and proposed by Murphy in [23]

$$\begin{aligned} p_{\mathrm{v,liq}}^{\mathrm{sat}} = &\exp\left(54.842763 - 6763.22/T - 4.210\,\ln(T) + 0.000367\,T\right. \\ &+ \tanh\left\{0.0415\,(T - 218.8)\right\}\left\{53.878 - 1331.22/T\right. \\ &\left.\left. -9.44523\,\ln\left(T\right) + 0.014025\,T\right\}\right) \end{aligned} \tag{2.7}$$

is used.

Once the criterion has been triggered, ice crystals grow by water deposition on their surface. This mechanism depend on the ambient temperature which cools the crystal and the rate of growth is related to the difference between the ambient vapor pressure p_{v} and the vapor pressure at its surface which is the saturation vapor pressure over ice $p_{\mathrm{v},I}^{\mathrm{sat}\,\dagger}$ corrected for surface curvature. Following [1, 24], mass growth rate can be expressed as

$$\frac{\mathrm{d}m_{\mathrm{c}}}{\mathrm{d}t} = \frac{4\pi\chi D_{\mathrm{v}}^{\dagger}\left(p_{\mathrm{v}} - p_{\mathrm{v},I}^{\mathrm{sat}\,\dagger}\right)}{\frac{D_{\mathrm{v}}^{\dagger} L_s p_{\mathrm{v},I}^{\mathrm{sat}\,\dagger}}{\kappa_{\mathrm{a}}^{\dagger} T}\left(\frac{L_s}{R_{\mathrm{v}} T} - 1\right) + R_{\mathrm{v}} T} \tag{2.8}$$

where χ is the crystal electrical capacitance which is a length function of the crystal shape only and accounts for the solution of steady diffusion. In the case of a spherical particle

$\chi = r_c$ the crystal radius. $D_v^\dagger$ and $\kappa_a^\dagger$ are respectively the molecular diffusion coefficient and the thermal conductivity of air. The † denotes here the corrections applied for collision geometry, sticking probability, and ventilation arround the crystal. L_s is the latent heat of sublimation in J kg^{-1}. $R_v = 461.52\,\mathrm{J.K^{-1}.kg^{-1}}$ is the specific gas constant for water vapor.

Molecular Diffusion

The molecular diffusion coefficient of a gas in air can be expressed

$$D_v = \frac{5}{16 N_A d_v^2 \rho_a} \sqrt{\frac{\mathcal{R} T M_a}{2\pi} \left(\frac{M_v + M_a}{M_a}\right)} \tag{2.9}$$

according to [24] where $N_A = 6.0221 \times 10^{23}\,\mathrm{mol^{-1}}$ is the Avogadro's number. $d_v = 3.11\,\text{Å}$ is the collision diameter of vapor. ρ_a the density of air. $\mathcal{R} = 8.3145\,\mathrm{J.mol^{-1}.K^{-1}}$ the universal gas constant. $M_a = 28.966\,\mathrm{g.mol^{-1}}$ and $M_v = 18.015\,\mathrm{g.mol^{-1}}$ are, respectively, molecular weight of air and vapor.

Corrected molecular diffusion is defined by

$$D_v^\dagger = D_v \omega_v F_{v,I} \tag{2.10}$$

with

$$\omega_v = \left\{ 1 + \left[\frac{1.33 + 0.71 \mathrm{Kn}_v^{-1}}{1 + \mathrm{Kn}_v^{-1}} + \frac{4\,(1 - \alpha_{v,I})}{3\alpha_{v,I}} \right] \mathrm{Kn}_v \right\}^{-1} \tag{2.11}$$

modeling the collision and sticking probabilities, with $\mathrm{Kn}_v = \frac{\lambda_v}{r_c}$ the Knudsen number of the condensing gas with respect to particles of radius r_c. $\lambda_v = \frac{M_a}{\pi N_A d_v^2 \rho_a} \sqrt{\frac{M_a}{M_a + M_v}}$ is the mean free path of a gas molecule. $\alpha_{v,I}$ the mass accomodation (sticking) coefficient which for water vapor deposition on ice is not well determined, however [25] propose to use 0.93 which is quite in agreement with the scattered experimental values compiled by [26], especially at low temperatures and is backed by more recent experiments [27].

and

$$F_v = \begin{cases} 1 + 0.14 x_v^2, & \text{if } x_v < 1.0, \\ 0.86 + 0.28 x_v, & \text{if } x_v \geq 1.0 \end{cases} \tag{2.12}$$

modeling the ventilation arround a particle moving in the airflow, with $x_v = Re_c^{1/2} Sc_v^{1/3}$,

where $Sc_\mathrm{v} = \frac{\nu_\mathrm{a}}{D_\mathrm{v}}$ is the gas Schmidt number with ν_a the kinematic viscosity of air and $Re_\mathrm{c} = 2r_\mathrm{c}U_\mathrm{rel}/\nu_\mathrm{a}$ is the crystal Reynolds number with U_rel the relative velocity of the crystal against the fluid (e.g. the terminal velocity of a falling crystal). In jet regime, because of the small size of crystals, U_rel is negligible as explained in 2.1.1. Because of that, ventilation have little to none impact on diffusion, in other words : $F_\mathrm{v} \approx 1$.

Thermal Conductivity Term

An interpolation of the thermal conductivity of moist air is given by

$$\kappa_\mathrm{dry} \approx 0.023807 + 7.1128 \times 10^{-5}\,(T - 273.15) \tag{2.13}$$

$$\kappa_\mathrm{v} \approx 0.015606 + 8.3680 \times 10^{-5}\,(T - 273.15) \tag{2.14}$$

$$\kappa_\mathrm{a} \approx \kappa_\mathrm{dry}\left[1 - \left(1.17 - 1.02\frac{\kappa_\mathrm{v}}{\kappa_\mathrm{dry}}\right)\frac{n_\mathrm{v}}{n_\mathrm{v} + n_\mathrm{dry}}\right] \tag{2.15}$$

where n_v and n_dry are the number of moles of water vapor and dry air, respectively.

Corrected thermal conductivity term is defined by

$$\kappa_\mathrm{a}^\dagger = \kappa_\mathrm{a}\omega_\mathrm{h}F_{\mathrm{h},I} \tag{2.16}$$

with

$$\omega_\mathrm{h} = \left\{1 + \left[\frac{1.33 + 0.71\mathrm{Kn}_\mathrm{h}^{-1}}{1 + \mathrm{Kn}_\mathrm{h}^{-1}} + \frac{4\,(1 - \alpha_{\mathrm{h,I}})}{3\alpha_{\mathrm{h,I}}}\right]\mathrm{Kn}_\mathrm{h}\right\}^{-1} \tag{2.17}$$

modeling the collision and sticking probabilities, with $\mathrm{Kn}_\mathrm{h} = \frac{\lambda_\mathrm{h}}{r_\mathrm{c}}$ the Knudsen number for energy where $\lambda_\mathrm{h} = \frac{3D_\mathrm{h}}{v_\mathrm{h}}$ is the thermal mean free path of air. $D_\mathrm{h} = \frac{\kappa_\mathrm{a}}{\rho_\mathrm{a}c_{p,a}}$ is the molecular thermal diffusivity with $c_{p,a} = c_{p,dry}\,(1 + 0.856y_\mathrm{v})$ the specific heat of moist air at constant pressure that uses $c_{p,dry} = 1004,67\ \mathrm{J.kg^{-1}.K^{-1}}$ the specific heat of dry air at constant pressure and $y_\mathrm{v} = \rho_\mathrm{v}/\rho_\mathrm{a}$ the mass ratio of vapor. $v_\mathrm{h} = \sqrt{\frac{8k_BT}{\pi\overline{m_\mathrm{a}}}}$ is the thermal speed of an air molecule with $k_B = 1.3807\times10^{-23}\ \mathrm{J.K^{-1}}$ the Boltzmann's constant and $\overline{m_\mathrm{a}} = 4.8096\times10^{-26}\ \mathrm{kg.molec^{-1}}$ is the average mass of one air molecule. $\alpha_{\mathrm{h,I}}$ is the thermal accomodation coefficient, we will use 0.96 [26], a value that is again backed by [27].

and $F_{\mathrm{h},I}$ defined similarly as $F_{\mathrm{v},I}$ with x_v replaced by $x_\mathrm{h} = Re_\mathrm{c}^{1/2}Pr^{1/3}$, where $Pr = \frac{\mu_\mathrm{a}c_{p,a}}{\kappa_\mathrm{a}}$ is the Prandtl number. Once again, because of the crystal size in jet regime, $F_\mathrm{h} \approx 1$.

Saturation Vapor Pressure

For low temperatures, saturation vapor pressure over ice is lower than over liquid. This implies that the pressure at the surface of the crystal is the saturation vapor pressure over ice. [23] proposed the following fit with T in K

$$p_{\mathrm{v},I}^{\mathrm{sat}} = \exp(9.550426 - 5723.265/T + 3.53068\,\ln(T) - 0.00728332\,T) \tag{2.18}$$

giving $p_{\mathrm{v},I}^{\mathrm{sat}}$ in Pa and valid for $T > 110\,\mathrm{K}$.

The saturation vapor pressure above a curved surface exceeds that of above a flat surface due to the increased tendency of molecules to escape from the curved interface and the impact of surface tension. We exploit the Kelvin's curvature correction [1, 24] given by

$$\frac{p_{\mathrm{v},I}^{\dagger}}{p_{\mathrm{v},I}} = \exp\left(\frac{2\sigma_{\mathrm{c}} M_{\mathrm{c}}}{r_{\mathrm{c}} \mathcal{R} T \rho_{\mathrm{c}}}\right) \tag{2.19}$$

where M_{c} and ρ_{c} are, respectively, the average crystal molar mass and the average crystal density. σ_{c} is the average crystal surface tension. The following fit is given in [28] for ice surface tension against vapor

$$\sigma_{\mathbf{i/v}} = 141 - 0.15T \tag{2.20}$$

where $\sigma_{\mathbf{i,v}}$ is in $\mathrm{erg.cm^{-2}} \equiv 10^{-3}\,\mathrm{J.m^{-2}}$ and T in K.

In the case of ice crystals $M_{\mathrm{c}} = M_{\mathrm{v}}$ and the following fit is given in [26] for ice density in the range of -180 to 0°C

$$\rho_I = 0.9167 - 1.75 \times 10^{-4} T - 5.0 \times 10^{-7} T^2 \tag{2.21}$$

where ρ_I is in $\mathrm{g.cm^{-3}} \equiv 10^3\,\mathrm{kg.m^{-3}}$ and T in °C.

Latent Heat of Sublimation

Exploiting data on the molar heat capacity of ice, [23] proposed the following fit with T in K

$$L_I = 46782.5 + 35.8925T - 0.07414T^2 + 541.5\exp\left\{-(T/123.75)^2\right\} \tag{2.22}$$

giving L_I the latent heat of sublimation per mol in J $\mathrm{mol^{-1}}$ and valid for $T > 30\,\mathrm{K}$.

Because Eq.(2.8) requires the latent heat of sublimation per unit of mass, the simple following relation have to be applied,

$$L_s = L_I / M_{\mathrm{v}} \tag{2.23}$$

2.1.3 Nucleation

Because of Kelvin's curvature correction, equation (2.19), and its impact on equation (2.8), a minimum particle size is required for ice growth to be actually positive. Nucleation denotes the processes by which a particle reaches this required radius [1]. They include a wide set of particles interactions events, with other particles (e.g., coagulation) or with chemicals (e.g., H_2SO_4 coating) [14, 29].

Contrail-suitable nuclei can originate from different types of particles. Research distinguishes two main categories: non-volatile particles (nvPM), which primarily consist of carbon aggregates such as soot particles, and volatile particles (vPM), which are chemical droplets formed from unburned fuel residues. While soot emissions have long been considered the dominant contributor to ice crystal nucleation, recent studies suggest that in modern engines, such as the CFM LEAP series, reduced soot emissions can lead to a transition where volatile particle nucleation becomes significant, potentially even yielding a higher number of ice particles [10].

In this study, we focus exclusively on soot particles, assuming a mean radius in the exhaust of the engine. This choice is justified by the fact that the CFM56 engine soot particles emissions still falls within the range where non-volatile particle nucleation prevails. Moreover, this simplification is sufficient to highlight the interest of the novel approach introduced in this work.

2.2 Numerical Approaches

2.2.1 Airflow

The ambient airflow is an important parameter for contrail particle evolution, because it dictates the turbulent mixing of plume with ambient air, cooling down the exhaust gases and spreading particles and species. The simplest approach to airflow is used for comprehensive parcel models [29], which considers the history of plume dilution and assumes uniform mixing across the plume cross section. However, since early stages of contrail formation occur in the near field of the aircraft, where the airflow is highly non-uniform because of the engine characteristics and later because of the vortexes created by the aircraft, it was proposed

to consider a more detailed description of the carrier phase [1, 7, 13, 14, 20–22, 30]. Often a detailed model of fluid transport was the counterpart to a simplified microphysical model, with the reverse being true [1]. It is only recently that attempts to do both simultaneously have been carried out.

RANS

The most used approach to model the gas carrier phase is the Reynolds Averaged Navier Stokes which provides the mean flow variables [7, 20, 31]. It is especially used to handle geometries impact on contrail because thanks to its relative low cost of computation, it makes it possible to have large domain with a reasonable ammount of cells and so geometries like engines or even full aircraft. However it implies to model turbulence, and all its effects on properties like temperature and concentrations.

LES

A more detailled approach is Large Eddy Simulation where only the small turbulence scales are modeled (the subgrid scales). Because greater scales are solved, it provides most of the fluctuations for the gas properties and velocity, allowing to catch directly the main effects of those fluctuations on non-linear terms without having to model them (activation for example can depend on a very singular set of properties, allowing the ice crystal to keep growing later, where with averaged properties it would never had been activated). But the downside of this method is definitely its cost, making it difficult to apply to a large set of ambient conditions. Additionally, geometries were never included in the domain directly because of the computationnal cost it would imply. Instead, initial conditions were either derived from correlations (eg turbofan jet plume and wingtip vortex [13, 14]), measured data [21, 32] or from associated precomputation with RANS [33, 34].

2.2.2 Particles Phase

Several approach to represent the particle phase were considered.

Eulerian

Because of the relatively high density of particles [22] modeled the particle phase by an eulerian transport model. He so added the mean radius aswell as a particle density conservative scalar to the existing set of cell variables in the RANS framework. This allowed him to consider the turbulence effect on convection by exploiting the boussinesq hypothesis to diffuse

the particles aswell. However, turbulence effects on the particle growth non-linearities were still not taken into account because of the averaging of scalar inputs and particle radius.

Lagrangian

The most spread option remains unsurprisingly the Lagrangian particle tracking [14, 20], because it is more natural. In this approach, sample of particles are tracked, each of the computational particles representing a set of physical particles in order to remove vapor from the gas and sometimes to apply a drag force on the carrier phase. [35] proposed a complete ice particles model, applied in cirrus, involving all microphysical processes, leading the path to fine simulation of contrail particles evolution.

2.3 Experimental Data

Experimental data play a crucial role in validating numerical models of contrail formation and evolution, yet obtaining such measurements remains challenging due to the complexity and cost of dedicated flight campaigns. In situ observations require aircraft to operate in the wake of contrail-generating flights, posing operational and safety constraints, particularly in the near field. As a result, experimental efforts are based on a combination of flight campaigns, remote sensing techniques, and laboratory studies to provide key parameters such as particle concentration, ice water content, and optical properties at various wake ages [1] and references therein.

The recent ECLIF 2 and 3 campaigns, in which a DLR A320 was chased by NASA's DC-8 Airborne Science Laboratory and an Airbus A350-941 was followed by a DLR Dassault Falcon 20-E5, respectively, provided extensive measurements of contrail formation and particulate emissions [5,36]. These campaigns characterized key metrics such as the apparent ice emission index, contrail optical depth, and ice particle diameter under varying atmospheric conditions, including temperature and humidity [36], and investigated the impact of alternative fuels [5, 37, 38]. Notably, for the first time, emissions were measured in the near field (100–200 m behind the aircraft) [5], whereas contrail properties were assessed at distances exceeding 5 nautical miles. The total number of non-volatile particles per kilogram of fuel burned confirmed the range of values used in our simulations for soot emissions. However, since the measured contrails were between 40 s and 140 s old, ice particle measurements are not directly comparable to our results without intermediate modeling of the vortex regime.

CHAPTER 3 NUMERICAL MODELING

3.1 Proposed Multi-Physics Numerical Integration

We developed a multi-physics framework based on a hybrid implementation combining finite-volume and particle-based methods. The workflow and the information exchanged between sub-models are illustrated in Figure 3.1.

The finite-volume solver serves two distinct purposes. First, it is used to run RANS simulations of the jet plume in the Eulerian domain, providing the aerodynamic flow-field in terms of cell-centered values of mean density, velocity, temperature, and pressure. These fields are subsequently used to resolve the conservation equations for the mean species mass fractions.

The Lagrangian particle-based method is constructed to model the dispersed phase consisting of soot particles and ice crystals. Numerical tracers, each representing a set of real soot particles, are advected using the Modified Simplified Langevin Model which uses the interpolated mean flow quantities from the underlying mesh as inputs. On each tracer, ice growth is computed, while scalar evolution is obtained from the IEM model. This stage provides scalar properties for each particle, enabling statistical post-processing of the associated PDFs. More importantly, this stage provides closure to the mean species equations by providing the mean sink term. This term is derived by time-averaging the water vapor consumption of the particles passing through a given cell.

This strategy is motivated by the good results the Stochastic Lagrangian approach had for reactive flows [16–18,39], but is modified by introducing coupling to mean Eulerian equations to prevent the need to compute non-reactive fluid particles to carry water from the freestream to the region of interest.

3.1.1 Monte Carlo Approach

The Monte Carlo method is a statistical approach widely used to solve stochastic differential equations. It models probability density functions (PDFs) of fluctuating properties through a large number of independent realizations. In our framework, this method provides a natural representation of turbulent fluctuations and nonlinear interactions by sampling individual particle trajectories. Moments required for coupling with the Eulerian phase, are directly computed from particles.

In the following, we contrast the averaged equations, which require statistical modeling, with

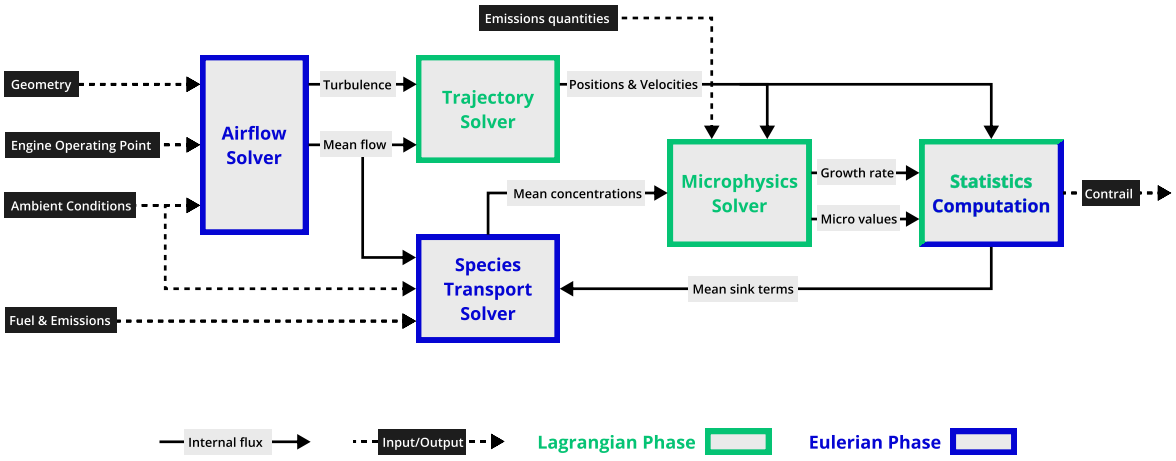

Figure 3.1 Workflow of the proposed contrail model

the stochastic differential approach, which inherently generates these statistics through the modeling of random processes.

3.2 Airflow Governing Equations

Airflow is governed by the compressible Navier Stokes equations for a perfect gas, which, in the absence of gravity, read [40].

$$\frac{\partial \rho}{\partial t} + \frac{\partial \rho u_j}{\partial x_j} = 0 \tag{3.1}$$

$$\frac{\partial \rho u_i}{\partial t} + \frac{\partial \rho u_i u_j}{\partial x_j} = -\frac{\partial p}{\partial x_i} + \frac{\partial \tau_{i,j}}{\partial x_j} \qquad i = 1, 2, 3 \tag{3.2}$$

$$\frac{\partial (\rho E)}{\partial t} + \frac{\partial \rho E u_j}{\partial x_j} = -\frac{\partial u_j\, p}{\partial x_j} + \frac{\partial u_i\, \tau_{ij}}{\partial x_j} + \frac{\partial}{\partial x_j}\left(\kappa_\mathrm{a} \frac{\partial T}{\partial x_j}\right) \tag{3.3}$$

where the viscous stress tensor is given by $\tau_{ij} = \mu\left(\frac{\partial u_i}{\partial x_j} + \frac{\partial u_j}{\partial x_i}\right) - \frac{2}{3}\mu \frac{\partial u_k}{\partial x_k}\delta_{ij}$ The air thermal conductivity κ_a and viscosity μ are related through the Prandtl number $Pr = \frac{c_p \mu}{\kappa_\mathrm{a}}$ that is set to 0.707 in this study.

In a mixture of N_s chemical species, Eqs 3.1-3.3 are complemented by the transport equations for the species mass fractions y_m:

$$\frac{\partial \rho y_m}{\partial t} + \frac{\partial \rho u_j y_m}{\partial x_j} = \frac{\partial}{\partial x_j}\left(\rho D_m \frac{\partial y_m}{\partial x_j}\right) + S_m \qquad m = 1, .., N_s - 1 \tag{3.4}$$

Where D_m and S_m are, respectively, the mass fraction, the diffusivity coefficient and the mass source term for species m. Similarly to the Prandtl number we define the Schmidt number $Sc_m = \frac{\mu}{\rho D_m}$. Because $\sum_{m=1}^{N_s} y_m = 1$, the last species mass fraction is given by

$$y_{N_s} = 1 - \sum_{m=1}^{N_s - 1} y_m \tag{3.5}$$

In this work, the only two constituent considered are dry air and water vapor, denoted respectively a and v. The equation for vapor transport is solved giving y_v, with $Sc_\mathrm{v} = 0.72$ [21] and S_v being the water consumption by ice crystals growth and will be defined later in 3.2.4. y_a is then given by (3.5).

At high Reynolds these equations, coupled with complex geometries, makes it impossible to obtain analytical solutions. This leads to numerical simulation which still has it loads of challenges because of the required precision needed to capture turbulence complexities. Several approaches to handle turbulence exists, we will explore two of them in the following subsections.

3.2.1 Reynolds Averaged Navier Stokes

For compressible flows, Reynolds Averaged Navier Stokes (RANS) equations are classically obtained by applying the Favre average operator $\tilde{\phi}$ to any variable ϕ:

$$\widetilde{\phi} = \frac{\overline{\rho\phi}}{\overline{\rho}} \tag{3.6}$$

$$\phi'' = \phi - \widetilde{\phi} \tag{3.7}$$

where the bar denotes the ensemble average. For statistically stationary turbulent flows, this can be expressed as a time average over a sufficiently long time interval T:

$$\overline{\phi} = \frac{1}{T}\int_T \phi \, dt \tag{3.8}$$

$$\phi' = \phi - \overline{\phi} \tag{3.9}$$

where ϕ and ϕ' denote the mean and fluctuating components of the flow. We note that $\overline{\phi'} = 0$ but that $\overline{\phi''} \neq 0$ in general.

Navier Stokes Equations

Applying Eqs. 3.6-3.9 to the conservation equations Eqs. 3.1-3.4 yields [40]

$$\frac{\partial \overline{\rho}\,\widetilde{u_j}}{\partial x_j} = 0 \tag{3.10}$$

$$\forall i \quad \frac{\partial \overline{\rho}\,\widetilde{u_j}\,\widetilde{u_i}}{\partial x_j} = -\frac{\partial \overline{p}}{\partial x_i} + \frac{\partial \overline{\tau}_{i,j}}{\partial x_j} - \frac{\partial \overline{\rho u_i'' u_j''}}{\partial x_j} \tag{3.11}$$

$$\frac{\partial \overline{\rho}\,\widetilde{u_j}\widetilde{E}}{\partial x_j} = -\frac{\partial \widetilde{u_i}\,\overline{p}}{\partial x_j} - \frac{\partial \overline{u_i'' p}}{\partial x_j} - \frac{\partial \overline{\rho u_i'' E''}}{\partial x_j} + \frac{\partial \overline{u_i \tau_{i,j}}}{\partial x_j} + \frac{\partial}{\partial x_j}\left(\kappa_{\mathrm{a}} \frac{\partial \overline{T}}{\partial x_j}\right) \tag{3.12}$$

where the unclosed terms $\overline{\rho u_i'' u_j''}, \overline{u_i'' E''}, \overline{u_i \tau_{ij}}$, etc. are modeled using a Boussinesq Eddy-Viscosity assumption [40]. In particular, the Reynolds stress tensor $\tau_{t_{i,j}} = -\overline{\rho u_i'' u_j''}$ is modeled as

$$\tau_{t_{i,j}} = \mu_t \left(\frac{\partial \widetilde{u_i}}{\partial x_j} + \frac{\partial \widetilde{u_j}}{\partial x_i} - \frac{2}{3}\frac{\partial \widetilde{u_k}}{\partial x_k}\delta_{ij}\right) - \frac{2}{3}\overline{\rho} k \delta_{ij} \tag{3.13}$$

where $k = \frac{\widetilde{u_i'' u_j''}}{2}$ is the turbulent kinetic energy and μ_t the turbulent viscosity.

Species Transport

In the same manner, averaging the species transport equations (3.4) yields

$$\forall m \quad \frac{\partial \rho \widetilde{u_j} \widetilde{y_m}}{\partial x_j} = \frac{\partial}{\partial x_j}\left(\overline{\rho} D_m \frac{\partial \widetilde{y_m}}{\partial x_j} - \overline{\rho}\widetilde{u_j'' y_m''}\right) + \overline{S_m} \tag{3.14}$$

where the turbulent diffusion terms are once again closed via the Boussinesq Eddy-Viscosity assumption:

$$\overline{\rho}\widetilde{u_j'' y_m''} = -\frac{\mu_t}{Sc_t}\frac{\partial \widetilde{y_m}}{\partial x_j} \tag{3.15}$$

where Sc_t is the turbulent Schmidt number, set to 0.9 in this work. [7, 11].

Turbulence Model

In this work, we used the k $-\,\omega$ SST turbulence model, which is well known for its versatility in treating mixed internal-external flows configurations such as nozzle-jet flows. The model blends between the classical k $-\,\omega$ near the wall and k $-\,\varepsilon$ away from the wall. Furthermore,

it appears a natural choice for the proposed hybrid Eulerian-Lagrangian stochastic model that requires knowledge of the local turbulent kinetic energy k and turbulent frequency or dissipation rate ω as discussed in the next section. Several variants of $\mathrm{k}-\omega$ SST exist, in this work we use the following equations,

$$\frac{\partial\left(\overline{\rho}k\right)}{\partial t}+\frac{\partial\left(\overline{\rho}\,\widetilde{u_i}k\right)}{\partial x_i}=P-\beta^*\overline{\rho}\omega k+\frac{\partial}{\partial x_j}\left[\left(\mu+\sigma_k\mu_t\right)\frac{\partial k}{\partial x_j}\right] \tag{3.16}$$

$$\frac{\partial\left(\overline{\rho}\omega\right)}{\partial t}+\frac{\partial\left(\overline{\rho}\,\widetilde{u_i}\omega\right)}{\partial x_i}=\frac{\gamma}{\nu_t}P-\beta\overline{\rho}\omega^2+\frac{\partial}{\partial x_j}\left[\left(\mu+\sigma_\omega\mu_t\right)\frac{\partial\omega}{\partial x_j}\right]+2\left(1-F_1\right)\frac{\overline{\rho}\sigma_{\omega 2}}{\omega}\frac{\partial k}{\partial x_j}\frac{\partial\omega}{\partial x_j} \tag{3.17}$$

where P is the production term given by

$$P=\tau_{t_{i,j}}\frac{\partial\widetilde{u_i}}{\partial x_j} \tag{3.18}$$

and the turbulent eddy viscosity is modeled as :

$$\mu_t=\frac{\overline{\rho}a_1k}{max\left(a_1\omega,\Omega F_2\right)} \tag{3.19}$$

In the equations above, Ω is the vorticity magnitude, F_1 and F_2 denote functions blending the model between $\mathrm{k}-\omega$ and $\mathrm{k}-\epsilon$, while $a_1,\beta,\beta^*,\gamma,\sigma_k,\sigma_{\omega+2}$ are model constants provided in [41].

3.2.2 Stochastic Differential Equation

In this section, we present the Lagrangian stochastic model that is coupled to the Finite Volume solver described above. For notational ease, we omit the explicit spatial and temporal dependence of a given property ϕ (e.g. temperature) associated with particle P, which is denoted by ϕ^P. Hence, throughout the following analysis, ϕ^p should be read as $\phi(t,\mathbf{x}^P(t))$. The ensemble average over all Lagrangian realizations ϕ^p and its fluctuation are defined, respectively, as

$$\overline{\phi}=\frac{1}{N_P}\sum_{P=1}^{N_P}\phi^p \tag{3.20}$$

$$\phi'=\phi^P-\overline{\phi} \tag{3.21}$$

The superscript P is now omitted unless necessary to avoid ambiguity.

We assume that $\rho' \ll \overline{\rho}$ since the effects of compressibility on turbulent fluctuations are limited in the present configuration and their inclusion would overly complicate the development and calibration of the stochastic model. Compressible extensions exist in the literature but only for applications to fully reactive flows such as in combustion [42]). This assumption, called the Morkovin's hypothesis [40] may be questionable at the nozzle exit because of the strong mixing between the hot core (lower density) flow and the cold (higher density) coflow. Note that the mean density variations and compressibility effects are accounted for in the model via the coupling with the mean-flow Favre-average equations resolved by the RANS model defined in Sec. 3.2.4.

The Navier Stokes equations and the species transport equations can be recast in a Lagrangian formulation that is better suited to stochastic model. Using the mass conservation equation (3.1), the fluid particle velocity increment is given by

$$\begin{aligned}\rho\frac{du_i}{dt} &= \rho\frac{\partial u_i}{\partial t} + \rho u_j\frac{\partial u_i}{\partial x_j} \\ &= \frac{\partial \rho u_i}{\partial t} + \frac{\partial \rho u_j u_i}{\partial x_j} - u_i\left(\frac{\partial \rho}{\partial t} + \frac{\partial \rho u_j}{\partial x_j}\right) \\ &= \frac{\partial \rho u_i}{\partial t} + \frac{\partial \rho u_j u_i}{\partial x_j}\end{aligned} \tag{3.22}$$

and similarly for any conserved scalar ϕ,

$$\rho\frac{d\phi}{dt} = \frac{\partial \rho\phi}{\partial t} + \frac{\partial \rho u_j\phi}{\partial x_j} \tag{3.23}$$

Dividing equations (3.2) and (3.4) by ρ, and separating the known terms on the left-hand side of the equations from the unknown terms on the right-hand side yields

$$\frac{du_i}{dt} + \frac{1}{\rho}\left(\frac{\partial \overline{p}}{\partial x_i} - \frac{\partial \overline{\tau_{i,j}}}{\partial x_j}\right) = \frac{1}{\rho}\left(-\frac{\partial p'}{\partial x_i} + \frac{\partial \tau'_{i,j}}{\partial x_j}\right) \tag{3.24}$$

$$\frac{dy_m}{dt} - \frac{\partial}{\partial x_j}\left(\frac{\mu}{Sc_m}\frac{\partial \overline{y_m}}{\partial x_j}\right) - \frac{1}{\rho}S_m = \frac{\partial}{\partial x_j}\left(\frac{\mu}{Sc_m}\frac{\partial y'_m}{\partial x_j}\right) \tag{3.25}$$

where ensemble averages are derived from the one-point, one-time Eulerian joint PDF of every particle properties which is generated by the model. In the velocity equation (3.24), the right hand side is a random force that combines the fluctuating pressure gradient and

the viscous stresses. Similarly in the scalar equation (3.25), the right-hand side represents molecular or thermal diffusion [15]. These unknowns are time-dependent random processes that require modeling. In this work, we explore the Langevin equation for the fluctuating force and the Interaction by Exchange with the Mean (IEM) model for the scalar diffusion.

The Langevin Model

The Langevin model is obtained by replacing the fluctuating force in equation (3.24) by a stochastic process. In its general form, it is given by the following stochastic differential equation (SDE) [43],

$$du_i = -\frac{1}{\rho}\frac{\partial \overline{p}}{\partial x_i}dt + \frac{1}{\rho}\frac{\partial \overline{\tau_{i,j}}}{\partial x_j}dt + G_{i,j}\left(u_j - \overline{u_j}\right)dt + b\,dW_i \tag{3.26}$$

where G_{ij} is a relaxation rate towards the mean and $dW_i \equiv \sqrt{dt}N_i|_t^{t+dt}(0,1)$ is a Wiener process, which is a sequence of normal random walks between times t and $t+dt$ with zero mean and variance dt. We seek to determine the relations between $G_{i,j}$, b and the flow statistics.

A property of Kolmogorov theory states that, at a high Reynolds number, the velocity increment variance over a time interval in the inertial range depends only on this interval duration and ε the turbulent kinetic energy dissipation rate. The Langevin equation is consistent with that property given that b is taken to be,

$$b = \left(C_0\,\varepsilon\right)^{1/2} \tag{3.27}$$

where C_0 is a universal Kolmogorov constant [15].

Mean Flow In order to verify that the mean flow equations generated by the Langevin equation correspond to the mean Navier-Stokes equations, we apply the ensemble average operator to both side of equation (3.26), yielding,

$$\overline{du_i} = -\frac{1}{\rho}\frac{\partial \overline{p}}{\partial x_i}dt + \frac{1}{\rho}\frac{\partial \overline{\tau_{i,j}}}{\partial x_j}dt \tag{3.28}$$

An important hidden aspect in the above equation is the definition of the velocity increment,

$$du_i \equiv u_i(t+dt, \mathbf{x}(t+dt)) - u_i(t, \mathbf{x}(t)) \tag{3.29}$$

which involves the evaluation of u_i at two different times (t and $t+dt$) and positions ($\mathbf{x}(t)$) and $\mathbf{x}(t+dt)$) where $\mathbf{x}$ is the vector of components x_i. However, because the ensemble average operator is conditioned at one given time and position, the increment du_i needs to be developed by using a Taylor expansion around t and $\mathbf{x}(t)$,

$$du_i = \left(\frac{\partial u_i}{\partial t} + \frac{dx_j}{dt}\frac{\partial u_i}{\partial x_j}\right)dt = \left(\frac{\partial u_i}{\partial t} + u_j\frac{\partial u_i}{\partial x_j}\right)dt \tag{3.30}$$

Multiplying by ρ, using our hypothesis $\rho = \overline{\rho}$, and exploiting the mass conservation equation, $\frac{\partial \rho}{\partial t} + \frac{\partial \rho u_j}{\partial x_j} = 0$, then taking the ensemble average we get

$$\rho\overline{du_i} = \left(\frac{\partial \rho\overline{u_i}}{\partial t} + \frac{\partial \rho\overline{u_i u_j}}{\partial x_j}\right)dt \tag{3.31}$$

Substituting it into the equation (3.28) and exploiting the decomposition (3.21) yields

$$\frac{\partial \rho\overline{u_i}}{\partial t} + \frac{\partial \rho\overline{u_i u_j}}{\partial x_j} = -\frac{\partial \overline{p}}{\partial x_i} + \frac{\partial \overline{\tau_{i,j}}}{\partial x_j} - \frac{\partial \rho\overline{u_i' u_j'}}{\partial x_j} \tag{3.32}$$

which correspond to the ensemble-averaged Navier-Stokes equations, wherein the final term on the right-hand side represents the Reynolds stresses.

It is instructive to compare the ensemble average of velocity increments, $\overline{du_i}$, with the increments of the ensemble-averaged velocity, $d\overline{u_i}$, given by

$$\begin{aligned}\rho\, d\overline{u_i} = \left(\rho\frac{\partial \overline{u_i}}{\partial t} + \rho u_j\frac{\partial \overline{u_i}}{\partial x_j}\right)dt &= \left(\frac{\partial \rho\overline{u_i}}{\partial t} + \frac{\partial \rho u_j\overline{u_i}}{\partial x_j}\right)dt \\ &= \left(\frac{\partial \rho\overline{u_i}}{\partial t} + \frac{\partial \rho\overline{u_j u_i}}{\partial x_j} + \frac{\partial \rho u_j'\overline{u_i}}{\partial x_j}\right)dt\end{aligned} \tag{3.33}$$

Inserting (3.32) into the above equation also gives

$$\rho\, d\overline{u_i} = \left(-\frac{\partial \overline{p}}{\partial x_i} + \frac{\partial \overline{\tau_{i,j}}}{\partial x_j} - \frac{\partial \rho\overline{u_i' u_j'}}{\partial x_j} + \frac{\partial \rho u_j'\overline{u_i}}{\partial x_j}\right)dt \tag{3.34}$$

Reynolds Stresses We look to compare the second-order statistics $\overline{u_i' u_j'}$ generated by the Langevin equation to the Reynolds stresses obtained from the Navier-Stokes equations. We first express the increments of the fluctuating component of velocity du_i' by subtracting equation (3.34) from equation (3.26)

$$
\begin{aligned}
du_i &= du_i - d\overline{u_i} \\
&= G_{i,k}u_k dt + b\, dW_i - \frac{1}{\rho}\left(-\frac{\partial \rho \overline{u_i' u_k'}}{\partial x_k} + \frac{\partial \rho u_k' \overline{u_i}}{\partial x_k}\right) dt
\end{aligned}
\tag{3.35}
$$

We then exploit the identity

$$
\begin{aligned}
d\left(u_i' u_j'\right) &\equiv u_i'(t+dt, \mathbf{x}(t+dt))\, u_j'(t+dt, \mathbf{x}(t+dt)) - u_i'(t, \mathbf{x}(t))\, u_j'(t, \mathbf{x}(t)) \\
&= u_i'\, du_j' + u_j'\, du_i' + du_i' du_j'
\end{aligned}
\tag{3.36}
$$

where $du_i' du_j' = b^2 dW_i dW_j$ because all terms in the product are $\mathcal{O}(dt^2)$ except for the product of Wiener processes, that is $\mathcal{O}(dt)$. Finally, using (3.35), we obtain

$$
\begin{aligned}
d\left(u_i' u_j'\right) =& \frac{1}{\rho}\left(u_i' \frac{\partial \rho \overline{u_j' u_k'}}{\partial x_k} + u_j' \frac{\partial \rho \overline{u_i' u_k'}}{\partial x_k} - u_i' \frac{\partial \rho u_k' \overline{u_j}}{\partial x_k} - u_j' \frac{\partial \rho u_k' \overline{u_i}}{\partial x_k}\right) dt \\
&+ \left(u_i' G_{j,k} u_k' + u_j' G_{i,k} u_k'\right) dt + b\left(u_i' dW_j + u_j' dW_i\right) + b^2 dW_i dW_j
\end{aligned}
\tag{3.37}
$$

Following the same reasoning as before, the ensemble average of the increment can be expressed as

$$
\rho \overline{d(u_i' u_j')} = \left(\frac{\partial \rho \overline{u_i' u_j'}}{\partial t} + \frac{\partial \rho \overline{u_i' u_j'}\, \overline{u_k}}{\partial x_k} + \frac{\partial \rho \overline{u_i' u_j' u_k'}}{\partial x_k}\right) dt \tag{3.38}
$$

Finally, by averaging equation (3.37) and applying the divergence-free condition to the fluctuating velocity field, one obtains the Reynolds stress transport equation by the mean velocity generated by the Langevin model

$$
\begin{aligned}
\frac{\partial \rho \overline{u_i' u_j'}}{\partial t} + \frac{\partial \rho \overline{u_k}\, \overline{u_i' u_j'}}{\partial x_k} =& -\left(\frac{\partial \rho \overline{u_i' u_j' u_k'}}{\partial x_k} + \rho \overline{u_i' u_k'} \frac{\partial \overline{u_j}}{\partial x_k} + \rho \overline{u_j' u_k'} \frac{\partial \overline{u_i}}{\partial x_k}\right) \\
&+ \rho\left(\overline{u_i' u_k'} G_{j,k} + \overline{u_j' u_k'} G_{i,k} + b^2 \delta_{i,j}\right)
\end{aligned}
\tag{3.39}
$$

where we used the properties: $\overline{u_i'} = 0$, $\overline{u_i' dW_j} = 0$, and $\overline{dW_i dW_j} = \delta_{i,j}$ acknowledging that the Wiener processes are uncorrelated between t and t + dt.

Kinetic Energy The transport equation of turbulent kinetic energy by the mean velocity $k = 1/2\overline{u_i' u_i'}$ is derived from equation (3.39), taking $i = j$ and summing over the indices i

$$
\frac{\partial \rho k}{\partial t} + \frac{\partial \rho \overline{u_k} k}{\partial x_k} = -\frac{1}{2}\frac{\partial \rho \overline{u_i' u_i' u_k'}}{\partial x_k} - \rho \overline{u_i' u_k'} \frac{\partial \overline{u_i}}{\partial x_k} + \rho \overline{u_i' u_k'} G_{i,k} + \frac{3}{2}\rho C_0 \varepsilon \tag{3.40}
$$

where b was replaced by the equation (3.27).

Calibration The Kolmogorov theory of local isotropy at high Reynolds number pushes to search for isotropic tensor $G_{i,j} = G\delta_{i,j}$ among all possible choices. This results in the simplified Langevin model [15, 18, 19, 39, 44, 45]

$$du_i = -\frac{1}{\rho}\frac{\partial \overline{p}}{\partial x_i}dt + \frac{1}{\rho}\frac{\partial \overline{\tau_{i,j}}}{\partial x_j}dt + G\left(u_i - \overline{u_i}\right)dt + b\,dW_i \tag{3.41}$$

and leads to

$$\frac{\partial \rho k}{\partial t} + \frac{\partial \rho \overline{u_k} k}{\partial x_k} = -\frac{1}{2}\frac{\partial \rho \overline{u_i' u_i' u_k'}}{\partial x_k} - \rho \overline{u_i' u_k'}\frac{\partial \overline{u_i}}{\partial x_k} + \rho 2kG + \frac{3}{2}\rho C_0 \varepsilon \tag{3.42}$$

The last calibration step is to compare this equation with another transport equation for the turbulent kinetic energy. In his paper, Pope [15] considers two cases of homogeneous turbulence. The stationary case, $\frac{\partial \rho k}{\partial t} + \frac{\partial \rho \overline{u_k} k}{\partial x_k} = 0$, yields

$$0 = \rho 2kG + \frac{3}{2}\rho C_0 \varepsilon \tag{3.43}$$

Gradients are null because of homogeneity. The relaxation rate is then given by

$$G = -\frac{3}{4}C_0\frac{\varepsilon}{k} \tag{3.44}$$

For the decaying case, $\frac{\partial \rho k}{\partial t} + \frac{\partial \rho \overline{u_k} k}{\partial x_k} = -\rho\varepsilon$, the same process provides

$$G = -\left(\frac{1}{2} + \frac{3}{4}C_0\right)\frac{\varepsilon}{k} \tag{3.45}$$

In the idea of extending the use of the Langevin equation to a coupled RANS stochastic Lagrangian framework, we propose a third calibration associated with the transport equation for k from the $\mathrm{k}-\omega$ SST model (3.16). Remarking that $P = \tau_{t_{i,j}}\frac{\partial \widetilde{u_i}}{\partial x_j}$, with $\tau_{t_{i,j}} = -\rho\overline{u_i' u_j'}$, and that $\omega = \varepsilon/\left(\beta^* k\right)$, we get

$$-\frac{1}{2}\frac{\partial \rho \overline{u_i' u_i' u_j'}}{\partial x_j} + \rho 2kG + \frac{3}{2}\rho C_0 \varepsilon = -\rho\varepsilon + \frac{\partial}{\partial x_j}\left[\left(\mu + \sigma_k \mu_t\right)\frac{\partial k}{\partial x_j}\right] \tag{3.46}$$

So far, the above expression is exact. However, the parameter G cannot be determined since, in general, we do not have access to turbulent transport individually. The term $-\sigma_k \mu_t \frac{\partial k}{\partial x_j}$

models the unknown flux $T'_j = \frac{1}{2}\rho\overline{u'_i u'_i u'_j} + \overline{u'_j p'}$ [44], which includes turbulent transport and pressure transport of turbulent kinetic energy. Insights could arise from Reynolds transport models, such as the Lumley model, which proposes the following assumption $\overline{u'_j p'} = -\frac{1}{5}\rho\overline{u'_i u'_i u'_j}$. However, DNS results have shown that in most flows this comparison is nontrivial [46]. Given this uncertainty, we follow the common approach in several other Reynolds stress models and neglect pressure transport [44]. This allows to calibrate G as

$$G = -\left(\frac{1}{2} + \frac{3}{4}C_0\right)\frac{\varepsilon}{k} + \frac{1}{2\rho k}\frac{\partial}{\partial x_j}\left[\mu\frac{\partial k}{\partial x_j}\right] \tag{3.47}$$

The first term is identical to the homogeneous decaying turbulence relaxation coefficient. The last term is the new contribution of non-homogeneous turbulence compatible with $\mathrm{k}-\omega$ SST (and can be easily generalized to any 2-equations eddy viscosity model).

Reynolds Number Dependence A defining parameter of this model is C_0. We introduced it earlier as the Kolmogorov Constant, however the Kolmogorov hypotheses requires only

$$C_0(Re_\lambda) \underset{Re_\lambda \to \infty}{=} \mathcal{C}_0 \tag{3.48}$$

where $\mathcal{C}_0 = 6.5$ is the actual Kolmogorov Constant and Re_λ is the Taylor scale Reynolds number. Because of that allowed freedom, the coefficient was set to several values, notably as a tuning parameter to fit over experimental results [16,19]. Exploiting DNS data, Pope [15] proposed the following empirical fit that allows to generalize its definition,

$$C_0(Re_\lambda) = \frac{6.5}{\left(1 + 140R_\lambda^{-4/3}\right)^{3/4}} \tag{3.49}$$

Finally we compute $Re_\lambda \approx \sqrt{\frac{20k}{3\nu\beta^*\omega}}$. A contour plot of C_0 is given in Figure 4.9.

IEM Equation

The Interaction by Exchange with the Mean model proposes to model the scalar diffusion term from equation (3.25), by a relaxation to the mean value of the scalar at the particle location. It is given by

$$\frac{dy_m}{dt} - \frac{\partial}{\partial x_j}\left(\frac{\mu}{Sc_m}\frac{\partial\overline{y_m}}{\partial x_j}\right) - \frac{1}{\rho}S_m = -\omega_m\left(y_m - \overline{y_m}\right) \tag{3.50}$$

where ω_m is the turbulent mixing rate. Similarly to what was done for the Langevin equation, we can show that this equation provides the correct mean equation. The expression for the scalar relaxation rate is given in [47] by

$$\omega_m = \frac{1}{2} C_\phi \frac{\varepsilon}{k} \tag{3.51}$$

where C_ϕ is a model constant called the mechanical-to-scalar timescale ratio. It is traditionally set at 2.0 [16], however, other values have been used in PDF calculations [18,39] with a limited impact on simulation results even for combustion [17].

3.2.3 Differences Between Approaches

The RANS and Lagrangian approaches differ in the quantities requiring modeling. In the RANS approach, terms that depend on fluctuating components require modeling. In the stochastic Lagrangian approach we model the physical processes that would require a coherent spatial definition of the instantaneous properties (e.g., the gradient of the instantaneous pressure).

In particular, the computation of the chemical source term $S_m\left(y_1, \ldots, y_{N_s}\right)$ is direct in the Lagrangian approach, while its ensemble average $\overline{S_m}$ which appears in RANS, equation (3.14), requires modeling. In previous RANS simulations of contrail formation [7, 20], mean source terms were modeled based on their computation over average properties. However,

$$\overline{S_m\left(y_1, \ldots, y_{N_s}\right)} \neq S_m\left(\overline{y_1}, \ldots, \overline{y_{N_s}}\right) \tag{3.52}$$

in general, particularly as the ice accretion rate exhibits significant non-linearity, discontinuities, and historical dependencies (activation).

3.2.4 Coupling with Mean Equation

The first coupling arises from the ensemble-averaged terms appearing in equations (3.26) and (3.50). Full Lagrangian approaches usually fill the domain with particles, allowing to directly compute the mean properties, using, for example, a particle/mesh method [15–17]. Existing coupled frameworks proposed to feed a finite-volume RANS solver with the Reynolds stress generated by the Lagrangian model, which are then closed by the mean properties obtained [45, 48]. However, these approaches require a large amount of computational particles, including in regions where no contrail particle would reside. Instead, the proposed framework—similarly to the approach described in [19]—supplies the mean quantities

$\overline{\rho}, \overline{u_j}, \frac{\partial \overline{p}}{\partial x_i}, \frac{\partial \overline{\tau_{i,j}}}{\partial x_i}, \overline{T}, \overline{y_m}, k, \varepsilon$ and $\frac{\partial}{\partial x_j}\left[\mu \frac{\partial k}{\partial x_j}\right]$ from the RANS solver to the Lagrangian setup, with the approximation that $\overline{\phi} \approx \widetilde{\phi}$ in the region of interest.

The second coupling stems from the coherence requirement between the IEM model (3.50) and the RANS equation for vapor transport (3.14). To that end, the mean vapor consumption is determined from the particles, thereby achieving closure with the RANS equation.

3.3 Numerical Implementation

3.3.1 CHAMPS Software

CHApel Multi-Physics Simulation (CHAMPS) is a solver developed in Chapel [49] at Polytechnique Montréal [50] to address complex multi-physics phenomena, such as aircraft icing [51]. Its computational fluid dynamics (CFD) solver employs a cell-centered finite-volume approach to solve the compressible RANS equations on unstructured meshes. Convective fluxes are discretized using a Roe scheme [52]. Second-order accuracy is achieved via gradient computations with a Weighted Least Squares method [40], in combination with limiters. Time integration is performed using an implicit Symmetric Gauss-Seidel (SGS) scheme [40]. Interfaces and boundary conditions are applied via ghost cells [40]. The solver is parallelized over multi-node, multi-core architectures, a feature natively supported by Chapel.

For this work, we extended the finite-volume solver with a RANS species transport module that handles an arbitrary number of species, using an upwind convective scheme with gradient-based facet interpolation.

3.3.2 Lagrangian Implementation

Due to the exceedingly large amount of physical particles within the engine plume—for example, around 10^{11} $\#/\mathrm{m}^3$ soot particles at the nozzle exit—each computational particle in the Lagrangian framework represents $N_\#$ actual particles [12, 14].

The integration of particle trajectories presents significant challenges associated with Eulerian-Lagrangian coupling. Lagrangian equations necessitate the interpolation of values from the finite-volume mesh, making it crucial to identify the element enclosing a particle. Additionally, the relaxation term in the Langevin equation introduces stiffness, which requires a robust integration scheme, similar to how drag forces are handled with larger particles [51].

Properties Interpolation

Mean flow properties are required to integrate the trajectory, they are listed in Section 3.2.4. Given a particle at position x_i and the element that contains it, we either use the cell-centered value or, when the gradient of a field is computed and used for the convective fluxes of the finite-volume solver, we extrapolate its value at the position of the particle x_i by

$$\phi\left(x_i\right) = \phi_{\mathrm{cc}} + \left.\frac{\partial \phi}{\partial x_j}\right|_{\mathrm{cc}} \left(x_{j,\mathrm{p}} - x_{j,\mathrm{cc}}\right) \tag{3.53}$$

where the subscript cc denotes a cell-centered value. Computing further gradients has yielded unsatisfactory outcomes, particularly in extrapolating the pressure gradient, due to the emergence of inconsistent spurious terms near regions of significant change, such as shocks.

The interpolation method for each term is summarized in Table 3.1.

Table 3.1 Interpolation method at particle position for each Eulerian field

Variable	Interpolation Method	Variable	Interpolation Method
$\overline{\rho}$	Gradient extrapolation	$\overline{u_j}$	Gradient extrapolation
$\overline{y_m}$	Gradient extrapolation	$\frac{\partial \overline{p}}{\partial x_i}$	Cell-centered
$\frac{\partial \overline{\tau_{i,j}}}{\partial x_i}$	Cell-centered	k	Cell-centered
ε	Cell-centered	$\frac{\partial}{\partial x_j}\left[\mu \frac{\partial k}{\partial x_j}\right]$	Cell-centered

Particle Seeding

Figure 3.2 shows the cross-sectional area of the engine's core nozzle—whose geometry is defined in 4.1.3—at which the computational particles are initially seeded following a random uniform distribution.

Emission Rate Computational particles are introduced at a seeding rate of $S_{\mathrm{comp}}(\#/\mathrm{s})$. Given a physical emission rate of particles—such as soot particles—denoted by $S_{\mathrm{phys}}(\#/\mathrm{s})$, each computational particle represents a group of physical particles. The number of physical particles modeled by a single computational particle is determined as

$$N_{\#} = \frac{S_{\mathrm{phys}}}{S_{\mathrm{comp}}} \tag{3.54}$$

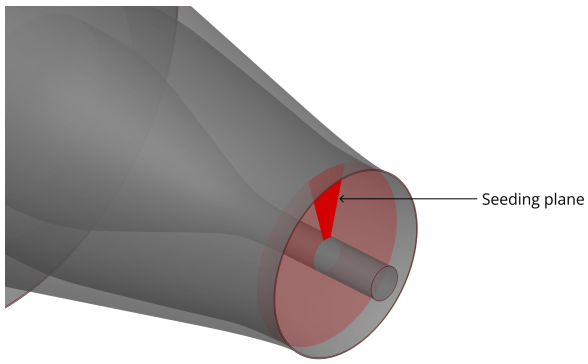

Figure 3.2 Computational particles seeding plane in the engine's core nozzle

QO Tree Randomness implies that the Eulerian mesh cell containing the newly seeded particle is unknown. Because the involved meshes generally contain a very large number of elements, a bulk search is impossible. Instead, an efficient "QO tree" search algorithm can be used [53]. QO trees refers to quadtrees and octrees that are, respectively, 2D and 3D data structures, used to store objects prior to a search [54]. Figure 3.3 a) illustrates a 3-level quadtree, an initial bounded box is then subdivided into all dimensions by 2 at each level. Then each mesh cell is stored in the smallest box that contains it [54] as shown in Figure 3.3 b). Ultimately, the corresponding cell for a particle is found through a recursive search within the box containing its position, commencing at the lowest level of the constructed QO tree.

In this study, the most natural initial bounding box is the one that contains the seeding cross section of the engine. This box is extended by the maximum edge length of the mesh, ensuring coverage of all elements intersected by the plane. An octree is the standard approach for storing 3D mesh cells, nevertheless, due to the significantly smaller third dimension of our bounding box, lower levels would contain no elements, rendering the algorithm ineffective. We thus propose the "flat octree" concept, essentially a quadtree with a constant third dimension size. This adjustment enables efficient particle seeding within a 2D plane.

Initial Properties Once the element has been identified, initial properties are interpolated from the mean phase. The velocity is then adjusted to introduce the expected initial variance by scaling a random normal perturbation with the interpolated kinetic turbulence intensity. This results in

$$u_i^0 = \overline{u_i}(\mathbf{x}^0) \; + \sqrt{2/3\, k(\mathbf{x}^0)}\, N_i \tag{3.55}$$

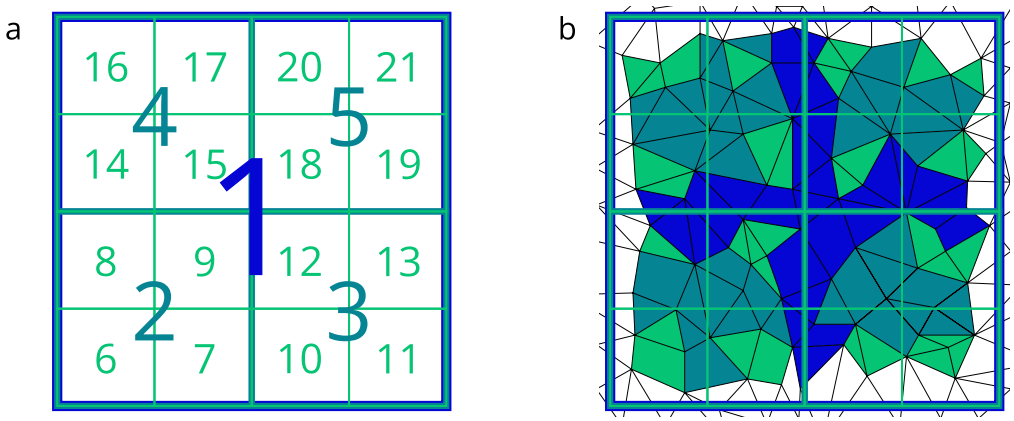

Figure 3.3 a) Quadtree subdivision in 3 levels. b) Example of a 2D unstructured mesh storage in a 3 levels quadtree

Particle Tracking

After a particle is initially localized within the mesh, trajectory integration can begin. However, it is necessary to update the element that contains the particle at each subsequent position, which requires a particle tracking algorithm. In CHAMPS, a Lagrangian approach to wing icing [51] uses a facet-to-facet algorithm [55]. However, since the Langevin equation requires a specific timestep, as detailed in 3.3.2, we cannot rely on this method, as it imposes an element-dependent timestep. Instead, we use the algorithm detailed by Haselbacher in [56].

Figure 3.4 a) illustrates the algorithm. Consider a particle in position $\mathbf{x}_n$ and known to be in cell e_1. To find the element containing the next position $\mathbf{x}_{n+1}$ the following procedure is applied: Starting from position $\boldsymbol{I}_0 = \mathbf{x}_n$, identify the facets of the elements whose outward normals point in the same direction as the particle evolves. Next, compute the intersection point with each facet plane without checking whether the point lies inside the facet at this stage. Finally, select the facet that is first intersected and use a facet-to-element connectivity table to identify the next element. Update the position $\boldsymbol{I}_j$ to the intersection point and iterate until the next intersection is further than the remaining distance to $\mathbf{x}_{n+1}$.

If a particle hits walls or a boundary of symmetry, then its next position $\mathbf{x}^p_{n+1}$ is reflected back into the domain, yielding the new position $\mathbf{x}_{n+1}$, its direction flipped, and the algorithm continues from $\boldsymbol{I}_{j+1} = \boldsymbol{I}_j$. If it crosses a periodic boundary, then its position is transformed into the other side of the domain (e.g., for a rotational periodicity, the position is rotated by the defining angle), its direction is transformed as well, and the algorithm continues from the transformed point of intersection on the associated facet on the other side of the domain.

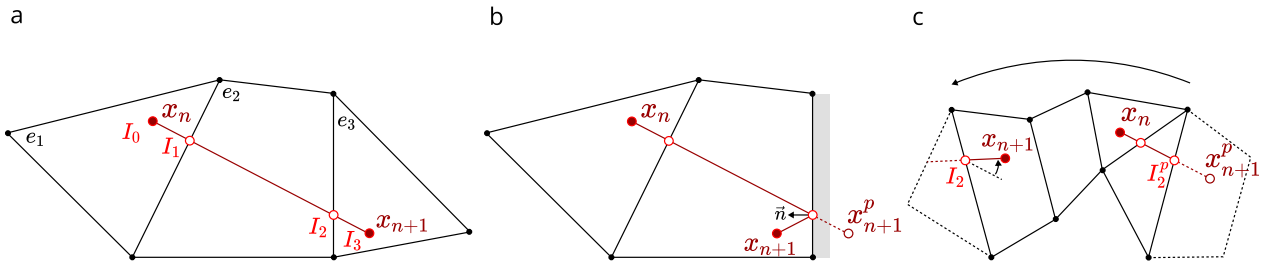

Figure 3.4 Particle tracking : a) Find the element containing position Q_{n+1} given that position Q_n was known to be located in element e_1. b) Wall treatment. c) Periodicity treatment.

Figure 3.4 b) and c) give examples of these specific treatments.

Numerical Integration

Crank-Nicolson Method A Crank-Nicolson method [57] is used to integrate the differential equations of velocity, position, and composition. This method is numerically stable and is based on the trapezoidal rule, allowing a second-order convergence in time. Its principle can be summarized by the following discretization of the differential equation $\frac{d\phi}{dt} = F_\phi$:

$$\frac{\phi^{n+1} - \phi^n}{\Delta t} = \frac{1}{2}\left[F_\phi^{n+1} + F_\phi^n\right] \tag{3.56}$$

Crucially, it relies only on the current timestep Δt, ensuring a straightforward treatment of the Wiener process, whose discretized form explicitly depends on Δt.

Velocity and Position The discretization of the Simplified Langevin Model (3.41) and the associated position equation yields

$$u_i^{n+1} = u_i^n + \frac{1}{2}\left[\overline{F_i}^n + \overline{F_i}^{n+1} + G^n\left(u_i^n - \overline{u_i}^n\right) + G^{n+1}\left(u_i^{n+1} - \overline{u_i}^{n+1}\right)\right]\Delta t + \frac{b^n + b^{n+1}}{2}\sqrt{\Delta t}\, N_i \tag{3.57}$$

$$x_i^{n+1} = x_i^n + \frac{1}{2}\left[u_i^n + u_i^{n+1}\right]\Delta t \tag{3.58}$$

where $\overline{F_i}^n = -\frac{1}{\overline{\rho}}\frac{\partial \overline{p}}{\partial x_i} + \frac{1}{\overline{\rho}}\frac{\partial \overline{\tau_{i,j}}}{\partial x_j}$ and G^n are, respectively, the mean force and the relaxation rate, evaluated at the position $\mathbf{x}^n$. N_i is a new sample from a standard normal distribution at each iteration, in each direction.

The relaxation term in the velocity equation is treated analytically by rearranging equa-

tion (3.57) as

$$u_i^{n+1} = \frac{u_i^n + \frac{1}{2}\left[\overline{F_i}^n + \overline{F_i}^{n+1} + G^n\left(u_i^n - \overline{u_i}^n\right) - G^{n+1}\overline{u_i}^{n+1}\right]\Delta t + \frac{b^n + b^{n+1}}{2}\sqrt{\Delta t}\, N_i}{1 - G^{n+1}\Delta t/2} \tag{3.59}$$

However, the dependence on the next position $\mathbf{x}^{n+1}$ cannot be handled explicitly and requires an iterative solver to resolve the coupling. To that end Algorithm 1 was implemented

Algorithm 1 Velocity and Position Update Algorithm

$u_i^{n+1,0} \leftarrow$ First guess with $\overline{F_i}^n, \overline{u_i}^n, G_i^n$
$x_i^{n+1,0} \leftarrow x_i^n + u_i^{n+1,0}\Delta t$
$p \leftarrow 0$
while p < Max steps **do**
    $\overline{F_i}^{n+1,p}, \overline{u_i}^{n+1,p}, G_i^{n+1,p} \leftarrow$ Interpolation at $x_i^{n+1,p}$
    $u_i^{n+1,p+1} \leftarrow$ Equation 3.59 with $\overline{F_i}^{n+1,p}, \overline{u_i}^{n+1,p}, G_i^{n+1,p}$
    $x_i^{n+1,p+1} \leftarrow x_i^n + \frac{1}{2}\left[u_i^n + u_i^{n+1,p+1}\right]\Delta t$
    if Converged **then Break** ▷ Exit the loop if converged
end while

Note that the particle-tracking process, as well as the transformation of position and velocity vectors due to boundary treatment, are not explicitly written in the algorithm.

Ice Growth and Composition Similarly to the velocity-position equation system, the discretization of ice growth and the IEM equations (3.50) for vapor and temperature yields

$$m_{\mathrm{c}}^{n+1} = m_{\mathrm{c}}^n + \frac{1}{2}\left[\frac{dm_{\mathrm{c}}}{dt}^n + \frac{dm_{\mathrm{c}}}{dt}^{n+1}\right]\Delta t \tag{3.60}$$

$$y_{\mathrm{v}}^{n+1} = \frac{y_{\mathrm{v}}^n + \frac{1}{2}\left[\frac{1}{\overline{\rho}^n}S_{\mathrm{v}}^n + \frac{1}{\overline{\rho}^{n+1}}S_{\mathrm{v}}^{n+1} - \omega_{\mathrm{v}}^n\left(y_{\mathrm{v}}^n - \overline{y_{\mathrm{v}}}^n\right) + \omega_{\mathrm{v}}^{n+1}\overline{y_{\mathrm{v}}}^{n+1}\right]\Delta t}{1 + \omega_{\mathrm{v}}^{n+1}\Delta t/2} \tag{3.61}$$

$$T^{n+1} = \frac{T^n + \frac{1}{2}\left[-\omega_T^n\left(T^n - \overline{T}^n\right) + \omega_T^{n+1}\overline{T}^{n+1}\right]\Delta t}{1 + \omega_T^{n+1}\Delta t/2} \tag{3.62}$$

$$p^n = \overline{\rho}\, R\, T^n \tag{3.63}$$

where the relaxation terms were treated analytically. $\frac{dm_{\mathrm{c}}}{dt}^n$ is given by equation (2.8) and involves T^n, p^n, y_{v}^n, $\overline{\rho}^n$ and m_{c}^n itself. The mean viscous diffusion terms were neglected, a reasonable assumption at high Reynolds number.

Since y_{v} is an intensive mass fraction and m_{c} is an extensive property, we introduce a fluid mass m_f for each computational particle. This fluid mass is defined by the fluid mass that crosses the seeding plane, divided by the number of computational particles emitted during the same period. The source term S_{v}, representing vapor depletion by ice growth, is then expressed as

$$S_{\mathrm{v}} = -\frac{1}{m_f/\overline{\rho}} \frac{dm_{\mathrm{c}}}{dt} N_{\#} \tag{3.64}$$

where $m_f/\overline{\rho}$ represents the current volume represented by the computational fluid particle.

The dependence on position $\mathbf{x}^{n+1}$ is fixed in this context because this integration is processed after the new position is found. However, the coupling between y_{v}^{n+1} and m_{c}^{n+1} requires the use of a similar algorithm as for the integration of velocity and position.

Convergence For velocity-position iterations, convergence is defined as a tolerance in $|\mathrm{u}^{n+1,p+1} - \mathrm{u}^{n+1,p}|$. For ice growth and composition, the difference $\left|\frac{dm_{\mathrm{c}}}{dt}^{n+1,p+1} - \frac{dm_{\mathrm{c}}}{dt}^{n+1,p}\right|$ is monitored. Due to discontinuities in the mesh between cells or in the mass growth rate at activation, the solver may encounter convergence difficulties. To address this, a timestep halving strategy was implemented.

Lagrangian Time Step

To compute the local Lagrangian time step, three criteria are combined. First, a convective CFL-based time step [58], Δt_{CFL}, is computed from the finite-volume fluxes and tuned with the coefficient γ_{CFL}, allowing control of the maximum number of cells skipped. Second, a time step based on gradients, Δt_{grad}, is determined by taking the inverse of the Frobenius norm of the local velocity gradient multiplied by the coefficient γ_{grad},

$$\Delta t_{\mathrm{grad}} = \gamma_{\mathrm{grad}} \left(\frac{\partial u_i}{\partial x_j} \frac{\partial u_i}{\partial x_j} \right)^{-1/2} \tag{3.65}$$

This term allows to consider, independently of the cell size, the variation rate of the mean velocity. Third, based on the recommendations of Pope [15, 19], the time step used to solve the Langevin equation should be considerably smaller than the integral time scale of the average flow field $T_L = \frac{4}{3C_0\beta^*\omega}$. Thus, using the coefficient, $\gamma_{\mathrm{T_L}}$, we define the time step

$$\Delta t_{\mathrm{T_L}} = \gamma_{\mathrm{T_L}} \frac{4}{3C_0\beta^*\omega} \tag{3.66}$$

The final local time step is chosen as the minimum of these three values

$$\Delta t = \min\left(\Delta t_{\mathrm{CFL}}, \Delta t_{\mathrm{grad}}, \Delta t_{\mathrm{T_L}}\right) \tag{3.67}$$

but is bounded below by a minimum allowable time step to prevent excessively small values. In our computations, γ_{CFL} was set to 100 to prevent excessively high timesteps in freestream regions with low gradients and low turbulent kinetic energy. Both γ_{grad} and $\gamma_{\mathrm{T_L}}$ were set to 1×10^{-2}, ensuring proper resolution of the Langevin equation.

Mean Fields Computation

To compute the mean fields from the Lagrangian particles—which serve both as coupling variables for the RANS solver and as statistical one-point outputs for post processing—we employ a weighted averaging procedure based on the residence time of each computational particle in the cells. For a given cell, the mean of a property ϕ^P, where the superscript P here denotes the evaluation while the particle is in the cell, is calculated as

$$\overline{\phi} = \frac{\sum_P \phi^P \Delta t^P_{cell}}{\sum_P \Delta t^P_{cell}} \tag{3.68}$$

where Δt^P_{cell} is the residence time of particle P in the cell. Note that while this represents the ensemble average over computed particles, it does not equal the theoretical ensemble average since only particles emerging from the core nozzle are simulated.

For the vapor depletion term and the contrail particle density, alternative formulas are used

$$\overline{S_{\mathrm{v}}} = \frac{\sum_P -\frac{dm_{\mathrm{c}}}{dt}^P N_{\#} \Delta t^P_{cell}}{T} \tag{3.69}$$

$$\overline{n_{\#}} = \frac{\sum_P N_{\#} \Delta t^P_{cell}}{T\, V_{cell}} \tag{3.70}$$

Unlike the previous statistics, this approach yields the true ensemble average, because non-computed particles (which would have $N_{\#} = 0$) would not contribute to these sums.

Numerically, these sums are computed on the fly at each iteration. While tracking the particle (see Figure 3.4), the fraction of the trajectory spent in each cell is used to weight the total time step. The particle properties are then linearly interpolated from t^n to t^{n+1}, and the corresponding contributions are added to each sum.

3.3.3 Contrail Simulation Procedure

As shown in Figure 3.1, the airflow solver can be executed as a pre-processing step, enabling the contrail simulation to focus on the coupling between the time-accurate Lagrangian phase and the steady-state mean species transport.

This simulation then follows a multiphase approach to ensure the statistical reliability of contrail results.

Initial Population Phase In this first phase, only the trajectory solver is active, allowing computational particles to be seeded and transported by the flow without microphysical interactions. The phase continues until the total number of particles in the domain stabilizes, indicating a balance between inflow and outflow. This step ensures that the coupling terms, when later activated, accurately represent the particle density.

Coupled Microphysics and Eulerian Interaction Microphysical processes are then activated, and the Lagrangian solver is coupled with the Eulerian species solver. Depending on the case, contrail ice particles either restart from a previously computed mean radius or start from the soot core size. At this stage, the simulation enters a fully coupled phase, where the contrail particles interact with the surrounding vapor field, consuming water vapor as they grow.

After several coupled iterations, the flow undergoes a first domain turnover, meaning that the initially seeded particles, which had an unrealistic initial radius, have completely exited the computational domain. Shortly after this, the mean vapor field reaches a statistical steady state, ensuring that the contrail particle properties are representative of physical conditions rather than being influenced by transient initialization effects.

During this phase, only the coupling terms (e.g., mean vapor sink term) are subject to statistical reduction and inter-node communication at each iteration, as explained in Section 3.3.4. This avoids unnecessary data transfers by delaying the reduction of all other statistics at the final writing step, significantly reducing communication overhead.

Post-Processing Phase In the final phase, a set of particles is simulated while the mean vapor field remains frozen. This approach ensures that particle trajectories and microphysics can be analyzed with steady mean flow. These passive particles serve as the primary dataset for statistical analysis. However, for one-point statistics (e.g., local mean radius or vapor mass fraction variance), the precomputed Eulerian statistical fields—accumulated throughout the

coupled phase—are used instead. To ensure accuracy, contributions from the first domain turnover are excluded from the final statistics.

3.3.4 Parallel Processing

Eulerian phase is associated with a partition of the mesh, referred to as a zone, which is assigned to each core for localized computation. The Lagrangian particle approach introduces additional computational challenges compared to standard Eulerian simulations, as particles move freely across subdomain boundaries, requiring efficient load balancing.

Statistics Computation Parallel computing enables the simulation to be distributed across multiple cores and nodes, thereby reducing overall computation time. However, when many cores update shared variables simultaneously, there is a risk of race conditions. To mitigate this, we introduce the concept of *Statistical Zones*—dedicated buffers that hold local statistical accumulations (e.g., particle residence time) for each core's assigned Eulerian subdomain. These buffers are sized to match the corresponding zones on neighboring cores, ensuring that statistical updates remain isolated until a safe, controlled reduction operation is performed.

Eulerian Data Availability At the multi-node level, a key challenge is ensuring that each node has access to essential Eulerian field data, such as the mean flow velocity, which would typically be stored in the memory of a single node. To address this, we establish *Data Zones*, which are lightweight copies of the required fields that are transferred at the start of the simulation and remain static throughout the computation. The only exception is the species mass fractions, which are updated periodically to ensure accurate tracking of vapor consumption.

Communications are minimized by performing local reductions of the statistical buffers before updating only the pertinent regions in foreign nodes. In the same way, when fetching updated species mass fractions, a mask is generated to identify cells that have encountered particles and their immediate neighbors. This targeted approach avoids the overhead of copying the entire domain, while ensuring that the relevant region is updated prior to each subsequent Lagrangian iteration.

The different data structures stored in each node's memory are illustrated in Figure 3.5.

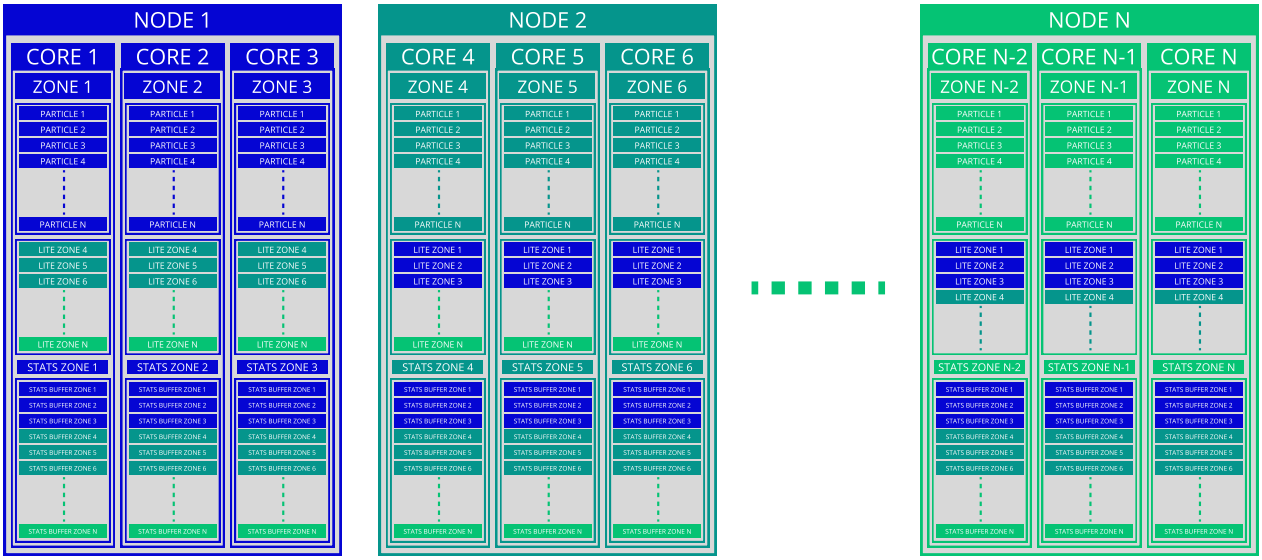

Figure 3.5 Parrallel data structure, showing the distribution of zones, particles, data zones, and statistical buffers across cores in multiple nodes.

3.4 Verification Tests

Two verification cases were conducted to evaluate the finite-volume solver. Since CHAMPS has been used primarily for external aerodynamics, its ability to handle hybrid internal external flows was assessed using the 'Axisymmetric Nearsonic Jet' case from the NASA Langley Research Center Turbulence Modeling Resource [59,60]. The second test verified the performance of the newly developed species transport solver using a method of manufactured solutions (MMS).

3.4.1 Verification of the Gas-Phase RANS Solver

To assess the accuracy of the gas-phase implementation, we compared the numerical results obtained with CHAMPS against computational results from the WIND solver [61], which itself has been validated against experimental measurements.

Computational Setup

The test case consists of a near-sonic jet issuing from the Acoustic Research Nozzle 2 (ARN2) with an exit radius of 25.4 mm (1 inch). The jet operates at an exit Mach number of 0.985, exhausting into a low-speed background flow of Mach 0.01. The computational domain is designed as an axisymmetric periodic grid, following the reference setup provided by NASA. The governing equations are solved using the $k-\omega$ SST turbulence model, consistent with

the WIND solver setup. A subsonic pressure inlet is imposed at the nozzle entrance, while a subsonic pressure outlet and a Riemann-type farfield boundary condition are applied, respectively, at the exit and the free-stream inflow.

We adopted the provided 257-point grid, which corresponds to NASA's second-finest resolution dataset.

Comparison of Flow Profiles

Figure 3.6 presents comparisons between CHAMPS results and WIND predictions for streamwise velocity, radial velocity, and turbulent kinetic energy profiles at various downstream positions. The subtle differences observed between the two datasets may stem from variations in the numerical treatment of convective fluxes. Nevertheless, the overall agreement confirms that the solver accurately captures the jet development, turbulence distribution, and velocity gradients in the near-sonic regime.

3.4.2 Verification of the Species Transport Solver

To verify the implementation of the species transport model, a method of manufactured solutions (MMS) was employed. The verification procedure ensures that the solver correctly handles convection, diffusion, and source terms in the species transport equations.

Computational Setup

The test case consists of a unit cube domain with a two-species system, where the species mass fractions are prescribed as:

$$y_1(x,t) = 0.5 + 0.4x^2, \tag{3.71}$$

$$y_2(x,t) = 0.5 - 0.4x^2. \tag{3.72}$$

To enforce this solution, the required source term $\overline{S_1}(x,t)$ is derived by substituting the manufactured solution into the species transport equation (3.14), yielding

$$\frac{\partial \rho_\infty u_\infty \widetilde{y_1}}{\partial x} = \left[\frac{\mu_\infty}{Sc_t} + \frac{\mu_{t\,\infty}}{Sc_t}\right] \frac{\partial^2 \widetilde{y_1}}{\partial x^2} + \overline{S_1} \tag{3.73}$$

$$\overline{S_1}(x) = 0.4 \times 2 \left(\rho_\infty u_\infty x - \left[\frac{\mu_\infty}{Sc_t} + \frac{\mu_{t\,\infty}}{Sc_t}\right]\right) \tag{3.74}$$

The domain is bounded by four slip walls, with a velocity inlet: Dirichlet inlet for the species mass fractions, and a pressure outlet: free outlet for the species. The velocity field is uniform, with velocity, density, viscosity, and turbulent viscosity set to, respectively, U_∞, ρ_∞, μ_∞, and $\mu_{t\,\infty}$.

Convergence Analysis

To assess numerical accuracy, simulations were conducted on three progressively refined meshes with 6171, 41921, and 312667 tetrahedrons elements. Figure 3.7 presents the results of these simulations. The first row shows 2D slice contour plots of the mass fraction $y_1(x, y)$ for each mesh, while the second row presents 1D line plots of the centerline mass fraction $y_1(x)$ along with the exact imposed solution.

The observed error L2 norm, summarized in Table 3.2, confirm first-order accuracy when using the upwind scheme. Additionally, incorporating gradient-based reconstruction for facet fluxes improves accuracy by approximately one order of magnitude.

Table 3.2 L2 error norms and convergence rates for species transport MMS test case

Elements	Characteristic Length (cm)	Base Upwind		Gradient Reconstruction	
		L2 Error	Convergence	L2 Error	Convergence
6171	5.69	1.05×10^{-4}		3.56×10^{-5}	
41921	2.99	3.10×10^{-5}	1.04	9.40×10^{-6}	0.95
312667	1.52	9.98×10^{-6}	0.88	2.86×10^{-6}	0.84

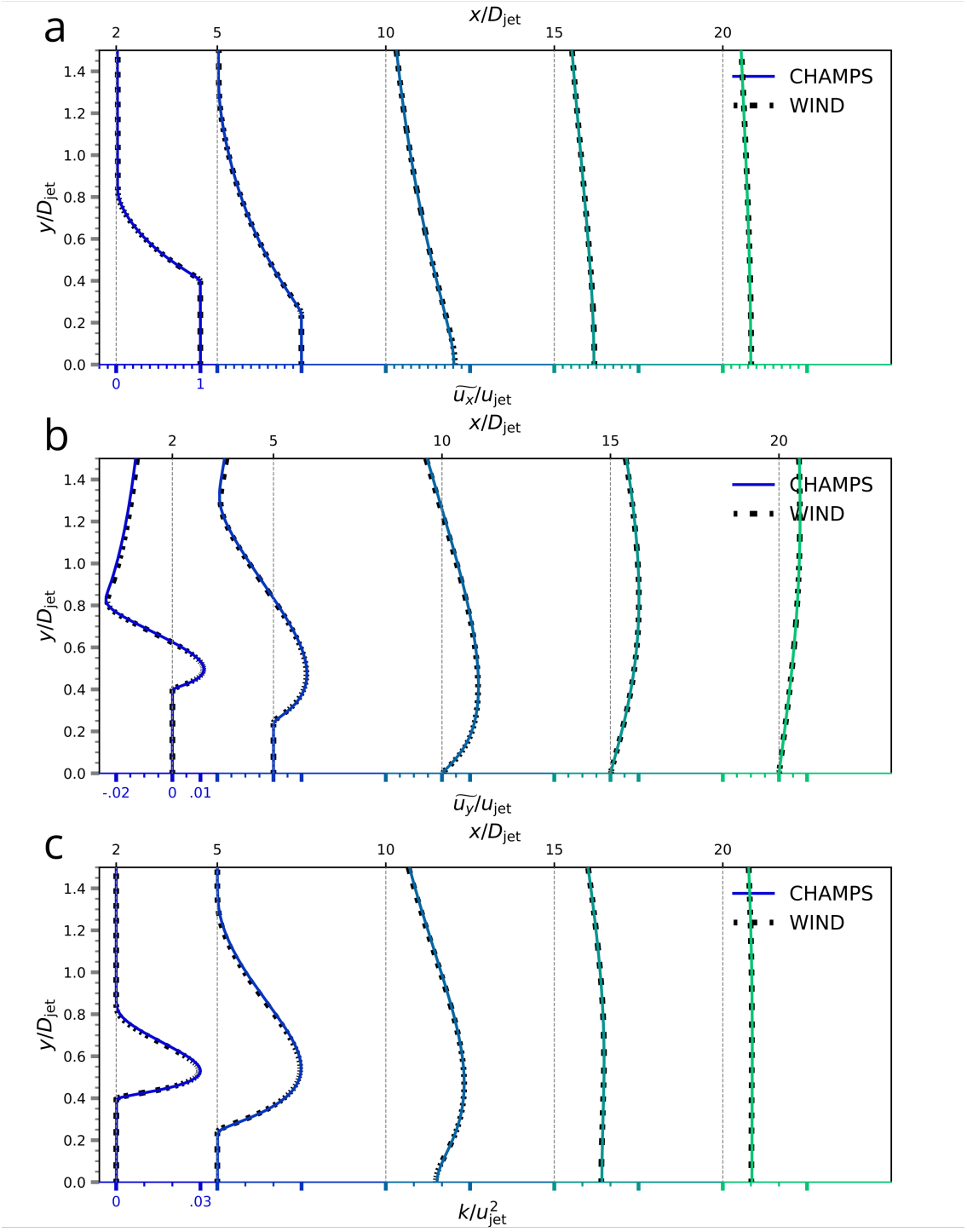

Figure 3.6 Comparison of CHAMPS and WIND [61] results for the near-sonic jet test case at various downstream positions. a) Streamwise velocity, b) Radial velocity, c) turbulent kinetic energy

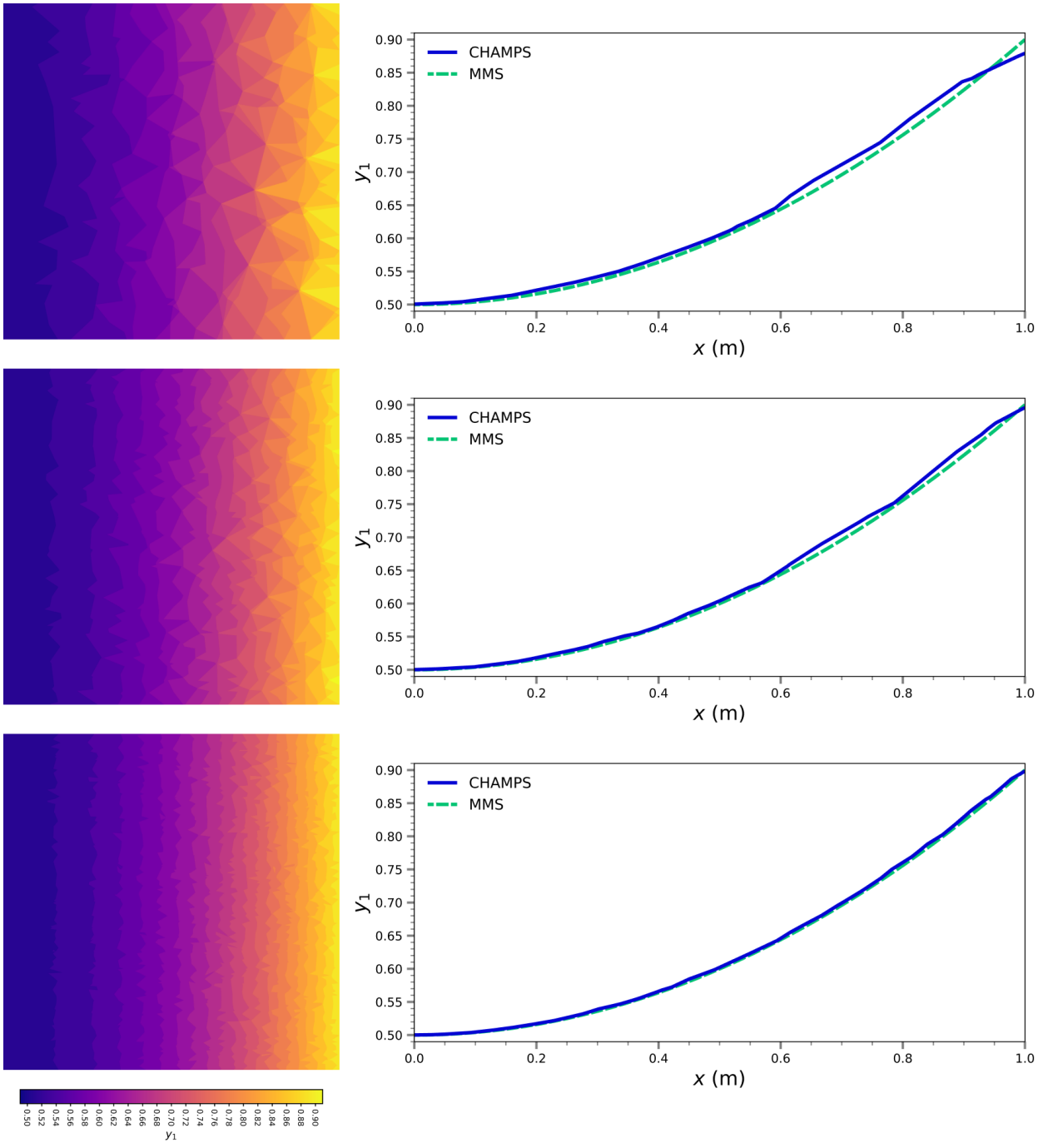

Figure 3.7 Species transport MMS verification, from top to bottom : 6171, 41921 and 312667 3D elements. Left : 2D contour plots of $y_1(x, y, z = 0.5)$ for different mesh resolutions. Right : 1D centerline profiles of $y_1(x, y = 0.5, z = 0.5)$ compared with the exact solution.

CHAPTER 4 CONTRAIL RESULTS

This chapter presents the results of the proposed model, starting with a comparison of the conventional RANS/Streamtrace Lagrangian approach and the novel methodology on a baseline physical case to highlight their differences. The model is then applied to variations of the base case to examine the sensitivity of contrail evolution to key parameters such as temperature, soot density, and atmospheric relative humidity.

4.1 Airflow Simulation of a CFM56-5B3 Plume

The CFM56 engine is one of the most widely used turbofan engines in commercial aviation, powering fleets of Boeing and Airbus aircraft around the globe. Through our collaboration with Safran, we gained access to detailed engine operating data, enabling a realistic and data-driven simulation of the CFM56-5B3 plume under typical cruise conditions. In particular, this specific engine configuration is employed on the Airbus A320.

4.1.1 Atmospheric Conditions

We consider standard cruise conditions at an altitude of 35,000 feet with a Mach number of $\mathrm{Ma}_\infty = 0.8$. The ambient pressure p_∞ is set according to the International Standard Atmosphere (ISA) [62]. However, instead of the temperature prescribed by ISA of 218.81 K, we adopt $T_\infty = 215\,\mathrm{K}$ to facilitate later sensitivity analyses.

The far-field velocity, corresponding to the cruise speed, is determined from the Mach number as $U_\infty = \mathrm{Ma}_\infty\sqrt{\gamma R_\mathrm{a} T_\infty}$, where $\gamma = 1.4$ is the air heat capacity ratio.

The dynamic viscosity μ_∞ is calculated using the Sutherland law [63]. The ambient density ρ_∞ is derived from the perfect gas law $\rho_\infty = \frac{P_\infty}{R_a T_\infty}$. Finally, the Reynolds number, based on the diameter of the bypass nozzle D_bp, defined in 4.1.3, is given by

$$Re_\infty = \frac{\rho_\infty U_\infty D_\mathrm{bp}}{\mu_\infty} \tag{4.1}$$

The values for these freestream conditions, along with the Reynolds number computed, are summarized in Table 4.1.

Table 4.1 Gas-phase : Freestream Conditions and Characteristic Numbers for the Simulation

Mach number	Ma_∞	0.8
Reynolds number	Re	1.10×10^7
Pressure (Pa)	p_∞	23842
Temperature (K)	T_∞	215
Density ($\mathrm{kg\,m^{-3}}$)	ρ_∞	0.386
Dynamic viscosity ($\mathrm{Pa\,s}$)	μ_∞	1.41×10^{-5}
Velocity ($\mathrm{m\,s^{-1}}$)	U_∞	235.16
Turbulent intensity	$I_{k,\infty}$	1%
Viscosity ratio	$\mu_{t,\infty}/\mu_\infty$	1

4.1.2 Engine Operating Point

Through collaboration with Safran, which employed a thermodynamic model of the engine, we obtained realistic operating conditions for the turbofan. This model provided total pressure and temperature values for each nozzle inlet, ensuring accurate boundary conditions for the simulation. The corresponding values are summarized in Table 4.2.

Table 4.2 Gas-phase : Nozzle boundary and exhaust conditions for the CFM56-5B3 engine

Bypass nozzle	Total pressure	$p_{t,\mathrm{bp}}/p_\infty$	2.473
	Total temperature	$T_{t,\mathrm{bp}}/T_\infty$	1.322
	Exhaust velocity ($\mathrm{m\,s^{-1}}$)	$U_{t,\mathrm{bp}}$	359.4
	Turbulent intensity	$I_{k,\mathrm{bp}}$	10%
	Viscosity ratio	$\mu_{t,\mathrm{bp}}/\mu_{\mathrm{bp}}$	500
Core nozzle	Total pressure	$p_{t,\mathrm{core}}/p_\infty$	2.329
	Total temperature	$T_{t,\mathrm{core}}/T_\infty$	3.244
	Exhaust velocity ($\mathrm{m\,s^{-1}}$)	$U_{t,\mathrm{core}}$	545.5
	Turbulent intensity	$I_{k,\mathrm{core}}$	10%
	Viscosity ratio	$\mu_{t,\mathrm{core}}/\mu_{\mathrm{core}}$	1000

A key observation was that, at such low ambient temperatures, variations in relative humidity had a negligible impact on engine performance due to the extremely low water vapor mass fractions in the ingested air. Consequently, only temperature was considered when adjusting the exhaust conditions.

In addition to inlet data, Safran also provided exit-plane velocity, allowing for an independent verification of our simulation results.

4.1.3 Computational Domain

Reconstructed CFM56-5B3 Rear Body Geometry

The turbofan rear body comprises the rear section of the nacelle along with the core and bypass nozzles. Its geometry is defined on the basis of a cut view of the engine, from which the aerodynamic lines of the bypass and core nozzles were extracted. These profiles were scaled using the exhaust dimensions: the bypass exit diameter is set to $D_{\text{bp}} = 1.71\,\text{m}$ and the core exit diameter to $D_{\text{core}} = 0.649\,\text{m}$, with adjustments made to yield the required sonic neck and exit plane area. A side view of these aerodynamic lines is presented in Figure 4.1.

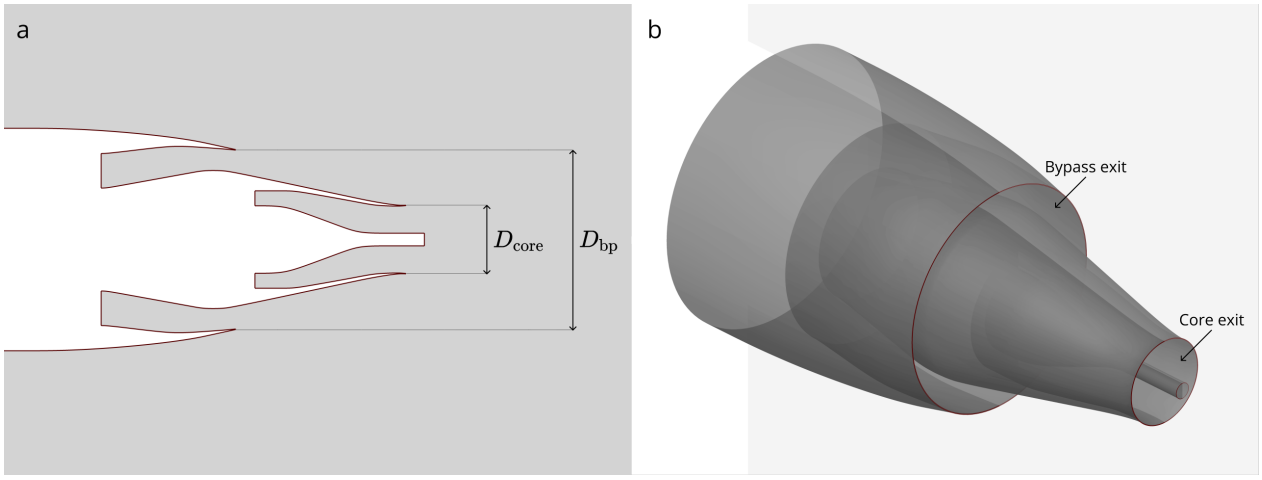

Figure 4.1 Reconstructed aerodynamic profiles of the bypass and core nozzles from the CFM56-5B3. a) side view, b) isometric view with the 360 geometry for reference

Full Domain

The computational domain then consists of a 30 ° sector of the exhaust geometry, which is then extended axially to 237 m and radially to 24 m. This configuration is designed to capture contrails up to 1 second old. Buffer zones have been incorporated to ensure a smooth transition to the boundary conditions, and the top boundary is inclined to promote incoming flow. A comprehensive view of the entire domain is shown in Figure 4.2 a).

Boundary Conditions

Adiabatic no-slip conditions are applied on the surfaces of the nozzle and nacelle. Additionally, extrusion buffers with slip-wall conditions extend the domain to move the inlet further upstream and enhance numerical stability. Subsonic pressure inlets are imposed for the

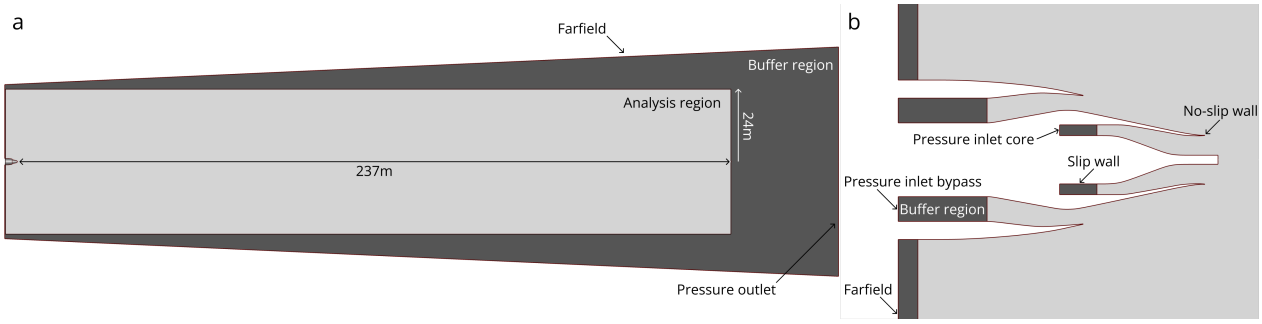

Figure 4.2 Overview of the computational domain and boundary conditions. a) Full domain and buffer zones, b) Zoom on turbofan

bypass and the core nozzle with, respectively, total pressures $p_{\text{tot,bp}}$, $p_{\text{tot,core}}$, and total temperature $T_{\text{tot,bp}}$, $T_{\text{tot,core}}$. A Riemann-type boundary condition is prescribed at the farfield, while a subsonic pressure outlet with ambient pressure is imposed at the domain exit. Symmetry conditions are enforced on the lateral boundaries at $-15°$ and $+15°$, as illustrated in Figure 4.2.

Furthermore, the k $-\,\omega$ SST inflow boundary conditions are imposed through the turbulence intensity $I_{k,\text{bc}}$ and the viscosity ratio $\mu_{t,\text{bc}}/\mu_{\text{bc}}$. This leads to

$$k = \frac{3}{2}\,|\mathbf{u}_{\text{bc}}|^2\; I_{k,\text{bc}}^2 \tag{4.2}$$

$$\omega = \frac{\rho\, k_{\text{bc}}}{\mu_{t,\text{bc}}} \tag{4.3}$$

where the velocity $\mathbf{u}_{\text{bc}}$, the density ρ_{bc} and the viscosity μ_{bc} are extrapolated from the domain.

Tables 4.1 and 4.2 summarize all values required to impose the boundary conditions for, respectively, the freestream and the engine.

Mesh

In this study, the computational mesh was generated using Fidelity Pointwise [64] with great care. A block topology was adopted to enable structured meshing of critical regions—such as the flow veins, the nacelle boundary layer, and the jet plume—which ensures high regularity along streamlines. Simultaneously, the far field is meshed in an unstructured manner, thereby reducing the total cell count and fully exploiting CHAMPS' capabilities for hybrid mesh handling. Special attention was given to accommodating the post-trailing edge expansion of

the boundary layers by smoothly uniformizing the cell size. A diamond-like topology was adopted for the axis to prevent the formation of degenerate, overly small cells, while a 10-cell rotational extrusion was applied to the remainder of the domain.

Refinement levels were chosen to properly capture key aerodynamic features. The first cell at the wall has a thickness of 2 µm to ensure proper boundary layer resolution. Additional refinement is applied near the nozzle neck and at the slip/no-slip interface, with an axial resolution of 1 mm in these regions to accurately capture potential sonic effects. Further refinement is concentrated around the core plug and the blunt trailing edges, which induce recirculation zones, to improve turbulence model accuracy.

The mesh meets stringent quality criteria: the maximum cell growth rate in both axial and radial directions does not exceed 1.2, and the skewness remains below 0.5. The final mesh comprises 7 884 125 mixed elements (tetrahedrons and hexahedrons), and preliminary simulations confirm that the wall y^+ remains below 1, ensuring proper resolution of the k $-$ ω SST turbulence model.

Figure 4.3 presents several views of the mesh, including two side views, an isometric view, and a zoom on the core plug diamond-like structure.

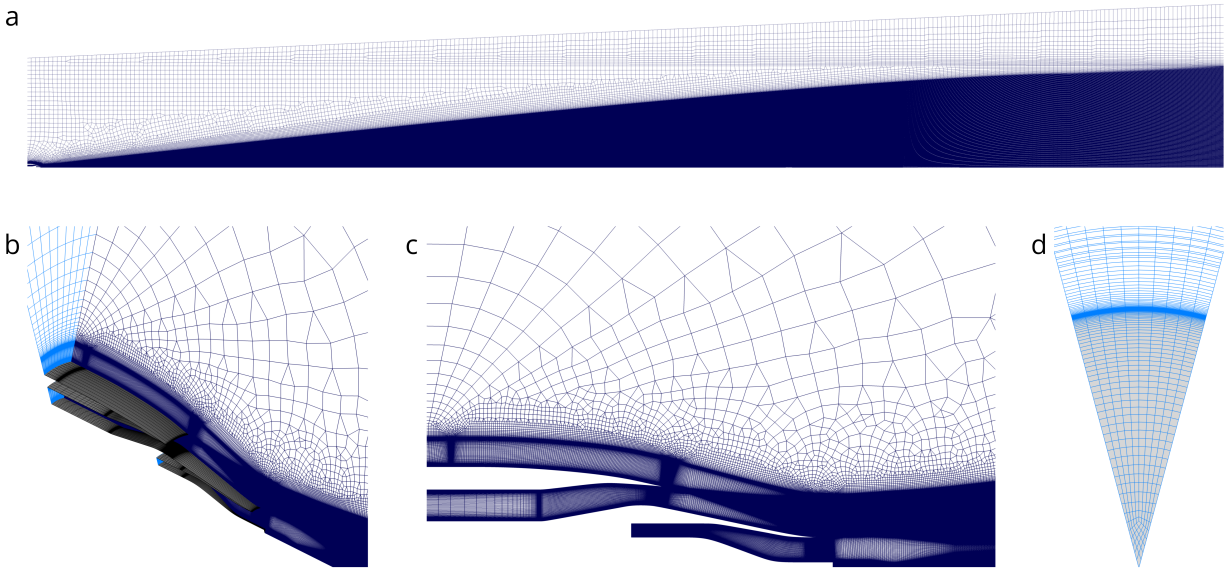

Figure 4.3 Overview of the computational mesh. a) Side view of the full domain, b) Isometric view, c) Side view zoomed in on the turbofan, d) Rear view of the diamond-like mesh structure around the core plug.

4.1.4 Convergence Strategy and Numerical Stabilization

Selective Frequency Damping (SFD) [65] was employed to suppress mesh-induced instabilities at the slip/no-slip interface. Since SFD acts as a low-pass filter, it primarily damps high-frequency numerical oscillations, stabilizing the solution without affecting the steady-state flow features.

A key challenge in the simulation was the strong coupling between the imposed inflow conditions and the interior flow field at the pressure inlets, where the total pressure and the total temperature are prescribed [40]. This coupling requires a precise Jacobian evaluation for implicit solving, as variations in the inlet conditions directly influence the internal flow solution. This issue is particularly critical near the inlets, where flow properties change rapidly, whereas far-field boundaries are less sensitive to such variations.

To further improve robustness, a boundary condition ramping approach was adopted, gradually transitioning the domain from its initial state to the target total pressure and temperature. This progressive adjustment helped prevent abrupt variations that could introduce instabilities and even unphysical values in the domain.

The RANS simulation was performed using a partitioned mesh distributed across 400 computing cores, with final convergence achieved through a residual reduction of eight orders of magnitude, ensuring a well-resolved and physically meaningful steady-state solution.

4.1.5 Calibrated Airflow Results

Figure 4.4 presents side views of key flow quantities—axial velocity, pressure, and temperature. Shock and expansion waves are observed just downstream of the nozzles, which is expected since both nozzle throats reach sonic conditions, which influences the flow evolution.

Normalized axial velocity profiles along selected cross-stream sections are shown in Figure 4.5. These profiles highlight two distinct regions typical of coaxial jet flows [20, 66]: a primary potential core that extends approximately $6.4\,D_{\mathrm{bp}}$ downstream, and a secondary potential core that fades after about $3.8\,D_{\mathrm{bp}}$.

Moreover, the predicted total pressure loss agrees within 1% with the operating conditions provided by Safran, as does the core exit velocity. The bypass exit velocity shows a 4% deviation, attributed to differences between the 1D thermodynamic model and the 2D simulation. This validation of key aerodynamic parameters underpins the reliability of the simulation results. The obtained aerodynamic flow field serves as the basis for subsequent computations in this study, except for two additional cases at lower and higher temperatures that required

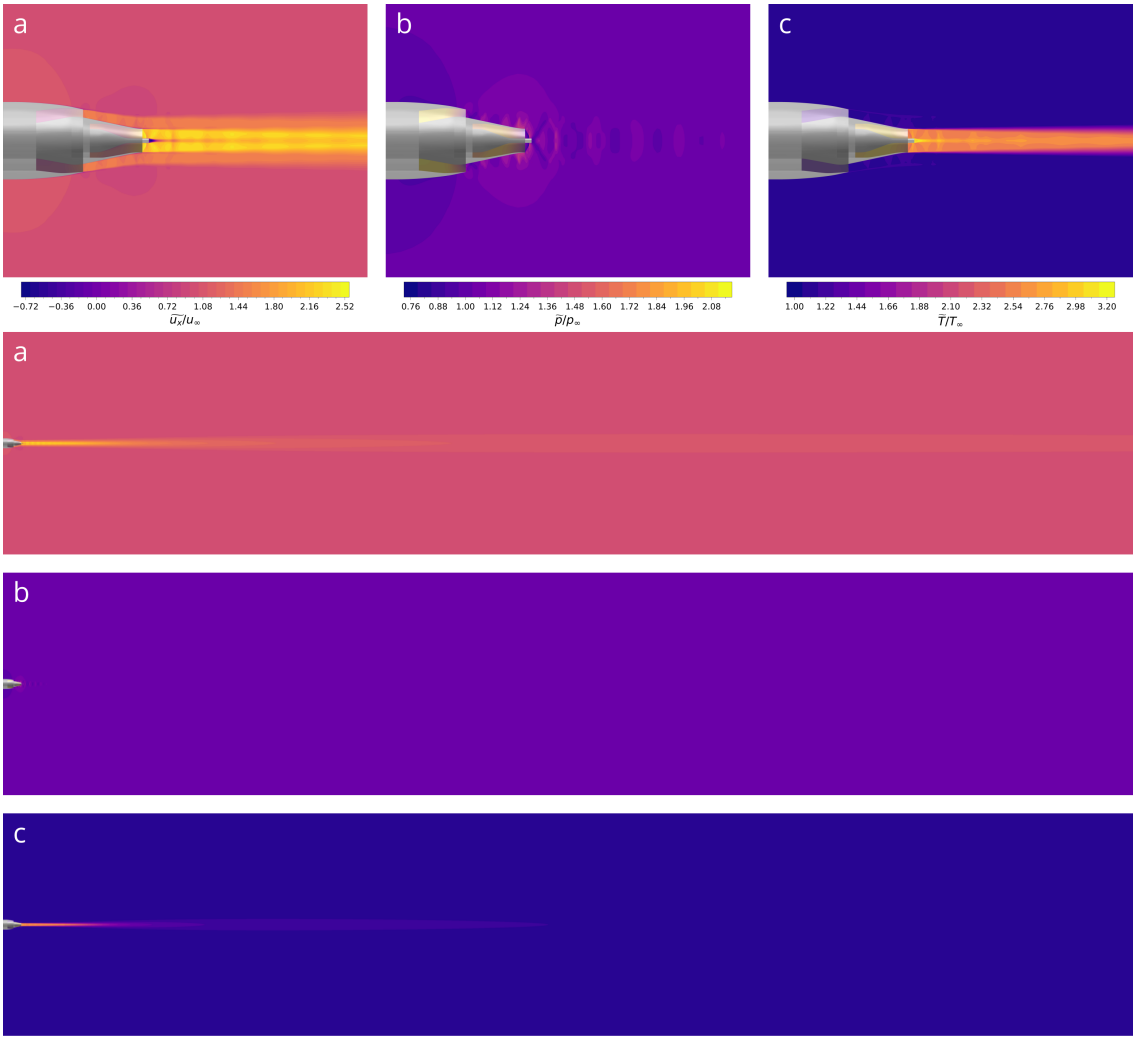

Figure 4.4 Mean flow contours of : a) axial velocity, b) pressure, c) temperature

separate RANS calculations.

4.2 Base Case Exhaust Composition and Ambient Vapor Conditions

This section defines the base case for contrail formation. We detail how inputs, such as the water vapor mass fraction, are derived for the simulation and provide the base case conditions.

4.2.1 Freestream Vapor Mass Fraction

To ensure contrail formation in our base case, the relative humidity over ice is set to RHI = 110%. The ambient vapor pressure is then obtained using $p_{\mathrm{v},\infty} = p_{\mathrm{v,I}}(T_\infty) \cdot \mathrm{RHI}$, where $p_{\mathrm{v,I}}(T_\infty)$ is the saturation vapor pressure over ice, as defined by Equation (2.18). This results

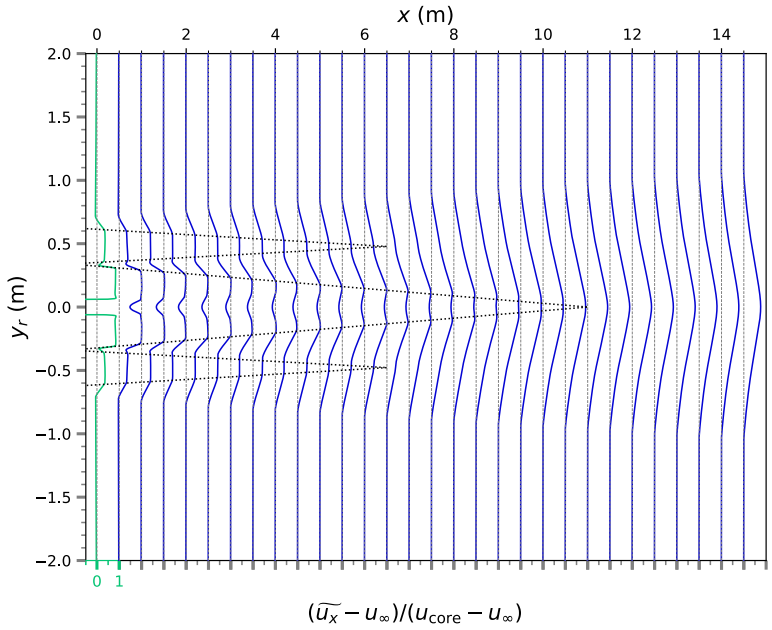

Figure 4.5 Normalized axial velocity profiles at various downstream locations. The dashed triangles indicate the extent of the primary and secondary potential cores.

in $p_{\text{v},\infty} = 1.525\,\text{Pa}$. The far-field water vapor mass fraction is then determined from the ratio of vapor partial pressure and air pressure as $y_{\text{v},\infty} = \frac{p_{\text{v},\infty} M_\text{v}}{p_\infty M_\text{a}}$, where M_v and M_a are the molar masses of water vapor and dry air, respectively. This yields $y_{\text{v},\infty} = 3.98 \times 10^{-5}$.

4.2.2 In-Flight Exhaust Composition

As mentioned in 1.1.1, to assess and mitigate aviation environmental effects, several fuels are considered. These fuels can affect contrail formation by impacting exhaust composition. In this study, we focus on conventional Jet-A1 fuel as the base case for exhaust properties.

Water Vapor Emissions

To determine the water vapor content in the exhaust, we use an average chemical formula for the fuel molecule, as measured by [67]: $C_{10.8}H_{21.6}$. For simplicity, we assume perfect combustion and derive the stoichiometric reaction for the fuel

$$C_{10.8}H_{21.6} + 16.2\,O_2 + 16.2\,(79/21)\;N_2 \rightarrow 10.8\,CO_2 + 10.8\,H_2O + 16.2\,(79/21)\;N_2 \qquad (4.4)$$

From this reaction, we calculate the mass of water vapor produced per unit mass of fuel burned using the following formula

$$\mathrm{EI}_{\mathrm{H_20,m}} = \frac{10.8 \times (2\,M_\mathrm{H} + M_\mathrm{O})}{1 \times (10.8\,M_\mathrm{C} + 21.6 M_\mathrm{H})} \tag{4.5}$$

Here, $M_\mathrm{H} = 1.008\,\mathrm{g\,mol^{-1}}$, $M_\mathrm{O} = 15.999\,\mathrm{g\,mol^{-1}}$, and $M_\mathrm{C} = 12.011\,\mathrm{g\,mol^{-1}}$ represent the molar masses of hydrogen, oxygen, and carbon atoms, respectively. This calculation gives us the water vapor mass emission index, $\mathrm{EI}_{\mathrm{H_20,m}} = 1.284\,\mathrm{kg\,kg^{-1}}$.

Finally, to determine the mass fraction of water vapor in the exhaust gases, we use the fuel-to-air ratio at the core exit $\mathrm{FAR}_\mathrm{core}$ and compute

$$y_\mathrm{v,core} = \mathrm{EI}_{\mathrm{H_20,m}} \times \frac{\mathrm{FAR}_\mathrm{core}}{\mathrm{FAR}_\mathrm{core} + 1} \tag{4.6}$$

This results in a water vapor mass fraction of $y_\mathrm{v,core} = 2.121 \times 10^{-2}$.

Soot Emissions

Similarly to water vapor, the quantity and mass of soot in exhaust gases are characterized by emission indices. The ICAO Emission Databank [9] collects emission indices for various flight phases, based on ground-level measurements performed at several engine ratings and subsequently extrapolated to in-flight conditions. Typically, the P3–T3 method [68], which exploits manufacturer's proprietary cycle data, is used to perform this extrapolation. For this study, Safran provided us with extrapolated indices that correspond precisely to our operating point. For the base case, the mass-based emission index is $\mathrm{EI}_\mathrm{soot,m} = 14.486\,\mathrm{mg\,kg^{-1}}$ and the number-based emission index is $\mathrm{EI}_\mathrm{soot,n} = 2.755 \times 10^{14}\,\#/\mathrm{kg}$.

Using the fuel-to-air ratio, we determine the soot particle emission rate at engine exit to be $S_\mathrm{soot} = 1.17 \times 10^{14}\,\#/\mathrm{s}$, which corresponds to a density of $6.89 \times 10^{11}\,\#/\mathrm{m^3}$ at the core nozzle exit. Since our computational domain comprises only a 30° section of the full exhaust, we scaled this value accordingly. The effective emission rate in our domain is given by $S_{\mathrm{soot},30^\circ} = 1/12\,S_\mathrm{soot} = 9.75 \times 10^{12}\,\#/\mathrm{s}$ ensuring that the particle density remains consistent within the simulated sector.

Soot Radius

Since soot particles are agglomerates of black carbon smaller particles, their effective density depends on the degree of compaction. For a few primary particles this density will tend

to carbon density, however the more the primary particles, the more the gaps. According to [11,69] this effective density, ρ_{eff}, relating soot mass to its equivalent diameter, d_m, follows the following power law :

$$\rho_{eff} = \begin{cases} \rho_{eff,100} \left(\frac{d_m}{d_{m,100}}\right)^{\zeta-3}, & \text{if } d_m < 140\,\text{nm}, \\ \rho_{eff,c}, & \text{if } d_m \geq 140\,\text{nm} \end{cases} \tag{4.7}$$

where $\rho_{eff,100} = 786\,\text{kg}\,\text{m}^{-3}$, $d_{m,100} = 100\,\text{nm}$, $\rho_{eff,c} = 651\,\text{kg}\,\text{m}^{-3}$ and $\zeta = 2.44$. Since $\rho_{eff} = \frac{6m_{soot}}{\pi d_m^3}$, we can deduce the following relation between m_{soot} and d_m,

$$d_m = \begin{cases} \left(\frac{6m_{soot}d_{m,100}^{\zeta-3}}{\pi\rho_{eff,100}}\right)^{1/\zeta}, & \text{if } m_{soot} < \frac{\rho_{eff,c}\pi d_{m,140}^3}{6}, \\ \left(\frac{6m_{soot}}{\pi\rho_{eff,c}}\right)^{1/3}, & \text{if } m_{soot} \geq \frac{\rho_{eff,c}\pi d_{m,140}^3}{6} \end{cases} \tag{4.8}$$

where $d_{m,140} = 140\,\text{nm}$.

Using emission indices, we can deduce the mass of a single soot particle : $m_{soot} = \frac{\text{EI}_{\text{soot,m}}}{\text{EI}_{\text{soot,n}}} = 5.258 \times 10^{-20}\,\text{kg}$. Finally, we deduce $d_m = 43.03\,\text{nm}$ which correspond to an effective density of $\rho_{eff} = 1260\,\text{kg}\,\text{m}^{-3}$.

We so obtain an initial radius $r_{soot} = 21.52\,\text{nm}$, very close to 20 nm, the value used by [20,22].

Table 4.3 summarizes the key base case parameters used in the simulation.

Table 4.3 Contrail base-case : Exhaust Composition and Ambient Vapor Conditions

Freesteam	Vapor mass fraction	$y_{\text{v},\infty}$	3.98×10^{-5}
Core nozzle	Vapor mass fraction	$y_{\text{v,core}}$	2.121×10^{-2}
	Soot particle emission rate (#/s)	S_{soot}	1.17×10^{14}
		$S_{\text{soot},30^\circ}$	9.75×10^{12}
	Soot initial radius (nm)	r_{soot}	21.52

4.3 Models Comparison

To evaluate the improvements offered by the newly proposed framework, several models are defined for comparison. In the first model, particles follow streamlines based on the mean velocity, with ice growth calculated using the mean fields for temperature and vapor mass fraction. In the second model, the Langevin equation is solved to generate turbulent trajectories, but ice growth is still calculated using mean fields. Finally, the third model represents the complete framework, incorporating the IEM equation to account for turbulent

diffusion of temperature and vapor.

Particle Phase Simulation Configuration The simulations were conducted with an emission rate of 25,000 computational particles per second. Since the domain length is defined based on the distance traveled by the aircraft in one second under cruise conditions, the number of active particles remains approximately the same as the seeding rate throughout the simulation. Each computational particle represents $N_{\#} = 3.90 \times 10^8$ soot particles. A total simulation time of 5 seconds was considered after the initial population phase, allowing mean radius fluctuations to decrease by nearly two orders of magnitude. Local statistics, such as the generated turbulent kinetic energy, were obtained through a window averaging between 1.15s and 5s. Additional statistics were derived from a set of 10,000 particle trajectories exported at the end of the simulation, following the methodology described in Section 3.3.3.

4.3.1 Mean Velocity - Mean Composition

In this first computation, particles are advected by mean flow velocity $\widetilde{\mathbf{u}}$, while ice growth is computed using the equations presented in Section 2.1.2 with $y_\mathrm{v} = \widetilde{y_\mathrm{v}}$ and $T = \widetilde{T}$. This implementation is inspired by the model proposed in [20], though there are some important differences. First, this study uses a steady-state gas-phase solution, whereas Cantin's model solves the unsteady RANS equations. Secondly, the growth rate equations differ slightly: in this work, the growth rate is scaled by the difference between the vapor pressure and the saturation vapor pressure over ice, whereas Cantin's model scales it by the difference between the vapor pressure and the saturation vapor pressure over liquid water. Due to these differences, a direct comparison of the results is not advisable. Instead, this calculation serves as a baseline for evaluating the effects of the stochastic model introduced in this study.

Figure 4.6 illustrates the particle trajectories following the mean velocity. In this configuration, particles travel almost in a straight line to the end of the domain. This is further supported by the spatial distribution of contrail particle radii, as shown in Figure 4.7, where the particle density remains nearly uniform even further downstream.

These distributions reflect the expected contrail formation process. Initially, high temperatures inhibit ice formation until mixing with ambient air cools the plume to saturation, allowing particles to grow, particularly at the edges of the plume, where jet-supplied vapor meets relatively lower temperatures. Figure 4.8 a) shows the evolution of the mean particle radius alongside the local mean saturation ratios for particles at the same downstream position. Growth begins once liquid saturation exceeds unity, after which vapor is depleted, driving saturation toward equilibrium at $p_\mathrm{v}/p_{\mathrm{v,I}}^{\mathrm{sat}} \approx 1$. These trends, along with Figure 4.8

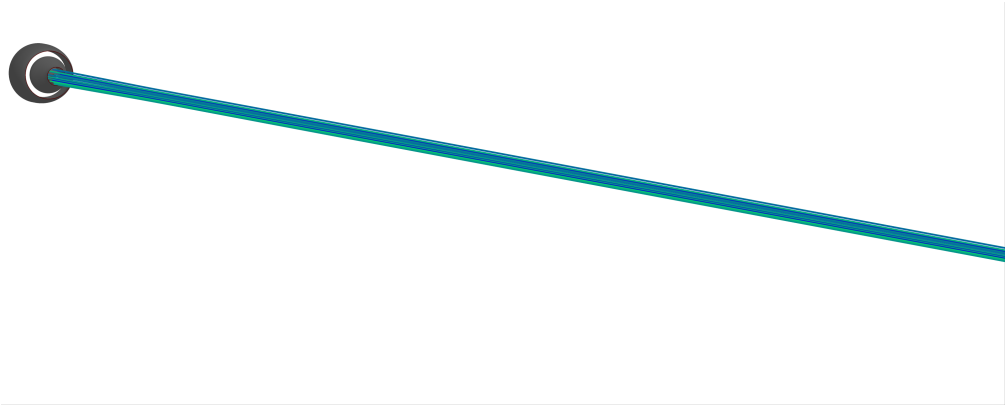

Figure 4.6 Reconstructed trajectories of 40 particles seeded in the core following the mean velocity. Rotation is accounted for by tracking periodic boundary crossings with an initial offset. Colors distinguish individual trajectories.

b), which maps particles on the vapor pressure-temperature diagram, confirm that the model implementation captures the overall ice growth dynamics.

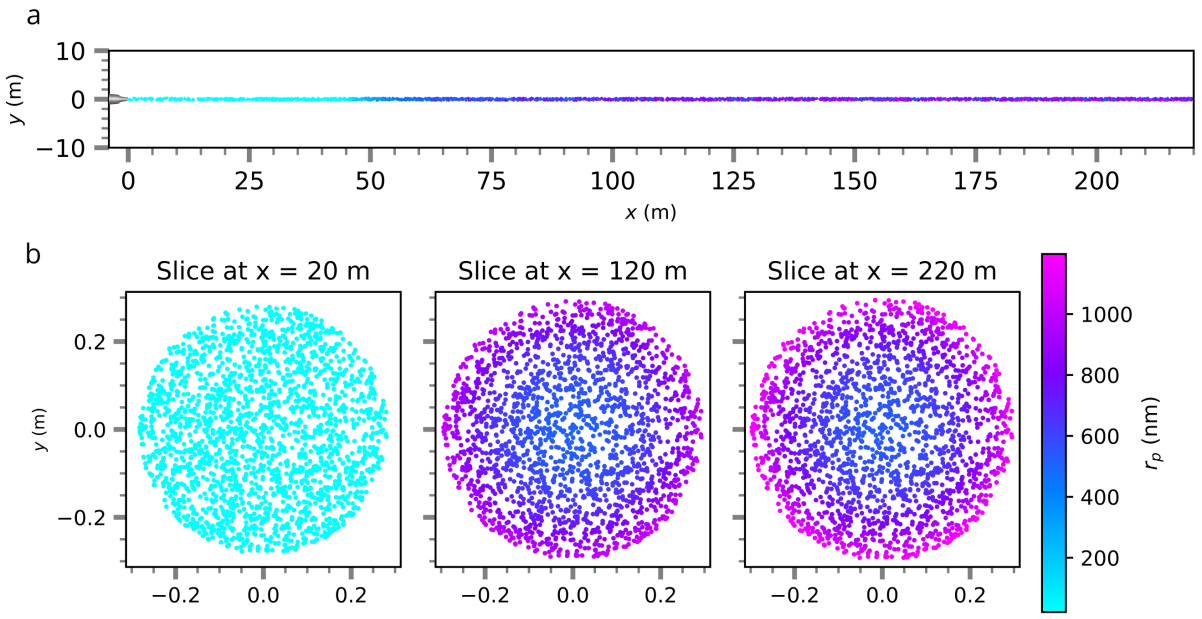

Figure 4.7 Mean velocity - Mean composition model : Spatial distribution of particles, colored by crystal radius. a) Side view, b) Cross-sectional distribution

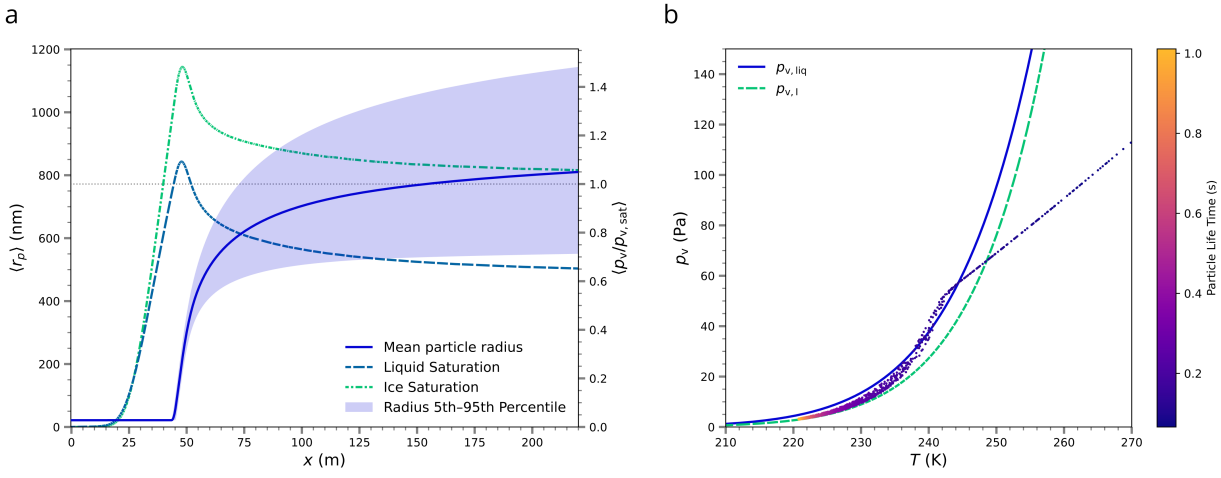

Figure 4.8 Mean velocity - Mean composition model : a) Evolution of the mean particle radius alongside mean saturation ratio over liquid water and over ice. b) Scatter plot of particles colored by life time in the thermodynamic diagram $T - p_v$

4.3.2 Turbulent Velocity - Mean Composition

In this second computation, the Simplified Langevin Model (3.41) is used to simulate particle velocity, capturing the effect of turbulent dispersion. However, the composition is still based on mean-field values, allowing us to isolate the impact of particle dispersion on ice growth. Figure 4.9 shows the contour of coefficient C_0 used for the Langevin equation calculation.

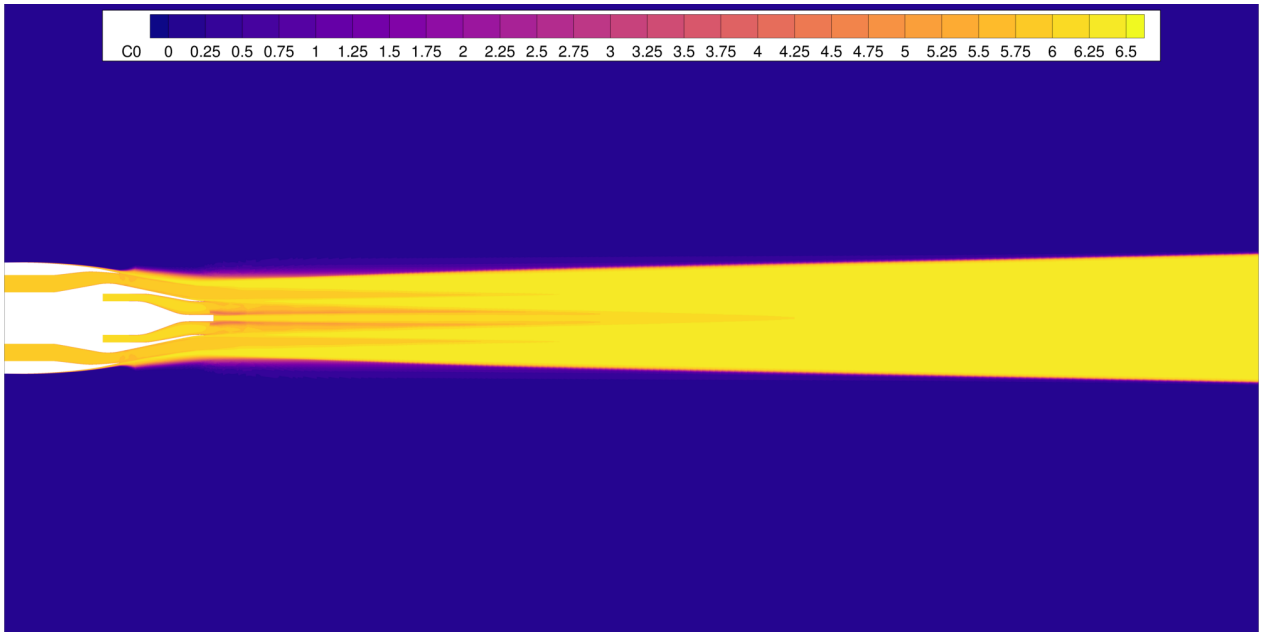

Figure 4.9 Contour plot of the model coefficient C_0 computed with equation (3.49)

Velocity Generated by Langevin Figure 4.10 illustrates the particle trajectories driven by the velocity generated using the Langevin equation. Turbulence was effectively introduced, leading to noticeable particle dispersion.

Further insight about the generated velocity field is obtained through an analysis of its statistical properties. The velocity statistics produced by the Langevin model are compared to the Favre-averaged quantities provided as input. One should note that, since only particles originating from the core nozzle were simulated, the Lagrangian phase averages are conditioned, as discussed in Section 3.3.2, leading, for example, to a positive mean radial velocity in mixing regions, where fluid particles from the freestream—entering the jet with negative velocity—would have strongly influenced the statistics. Figures 4.11 a) and b) compare, respectively, the mean axial velocity ($\widetilde{u_x}$ versus $\overline{u_x^P}$) and the turbulent kinetic intensity (k against $\frac{1}{2}\overline{u_i'^P u_i'^P}$). Overall, the generated statistics show good agreement with the input data, particularly in regions with high particle density, where the ensemble average is dominated

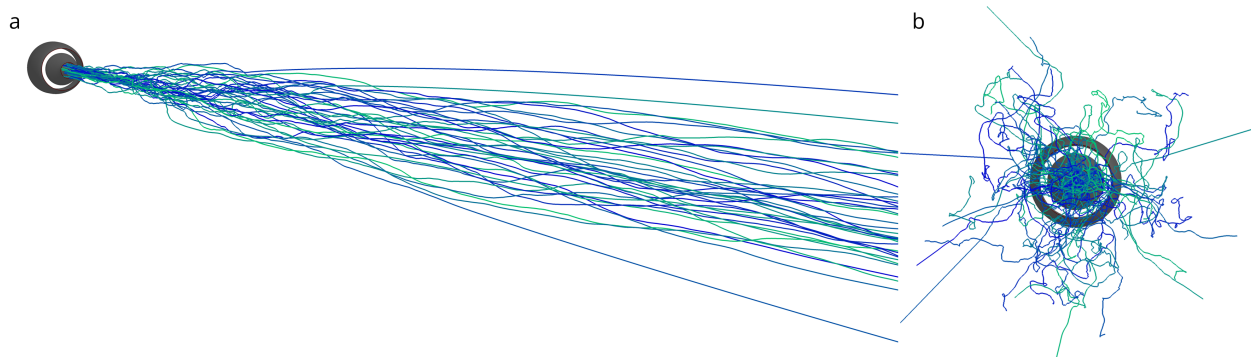

Figure 4.10 Reconstructed trajectories of 40 particles seeded in the core nozzle following the velocity generated by the Langevin equation. a) Isometric view, b) View from behind. Rotation is accounted for by tracking periodic boundary crossings with an initial offset. Colors distinguish individual trajectories.

by core nozzle particles. Some particles leaving the mixing layer exhibit slightly higher velocities than expected. While this theoretically increases local velocity variance and could lead to stronger relaxation, our model does not adapt due to the one-way coupling assumed. Nevertheless, even in simulations coupled with self-generated statistics, similar deviations were observed [39], and artificial corrections were introduced, an approach not explored in this work.

Contrail Results Figure 4.12 illustrates the contrail obtained using turbulent trajectories. The Langevin model effectively opens the plume, while most particles remain within a disk of diameter $D_{\text{core}} = 0.649\,\text{m}$ at $x = 20\,\text{m}$, the plume expands to approximately $7.4\,\text{m}$ at $x = 220\,\text{m}$. However, the particle radii appear significantly larger than those predicted by the Mean Velocity model.

As shown in Figure 4.13 a), the thermodynamic response is slower in this case, with a higher peak saturation, leading to a higher particle growth rate. This occurs because the increased dispersion reduces local particle density, particularly at the plume edges, weakening their influence on the surrounding mean vapor concentration. Figure 4.13 b) indeed shows that, even if the particles eventually reach equilibrium, their evolution in the $T - p_{\text{v}}$ plane is much closer to the mixing line, indicating a more passive interaction with ambient water vapor.

This model is qualitatively inexact, as it approximates the ambient vapor pressure around the particles using its local average. Consequently, it fails to capture the instantaneous vapor depletion along the particle streamlines, where the instantaneous particle density can be significantly higher than the long-term local average.

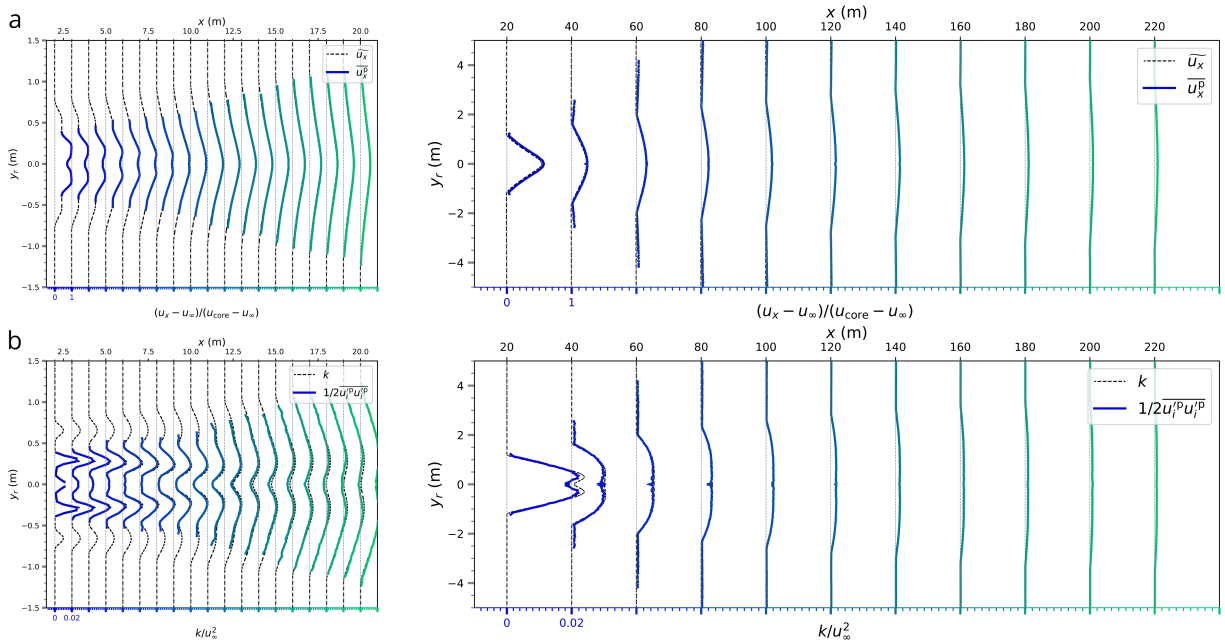

Figure 4.11 Comparison between RANS solver quantities and Eulerian particle statistics from the Langevin model. (a) Axial velocity normalized by the core nozzle excess velocity. (b) Turbulent kinetic energy normalized by the square of the freestream velocity.

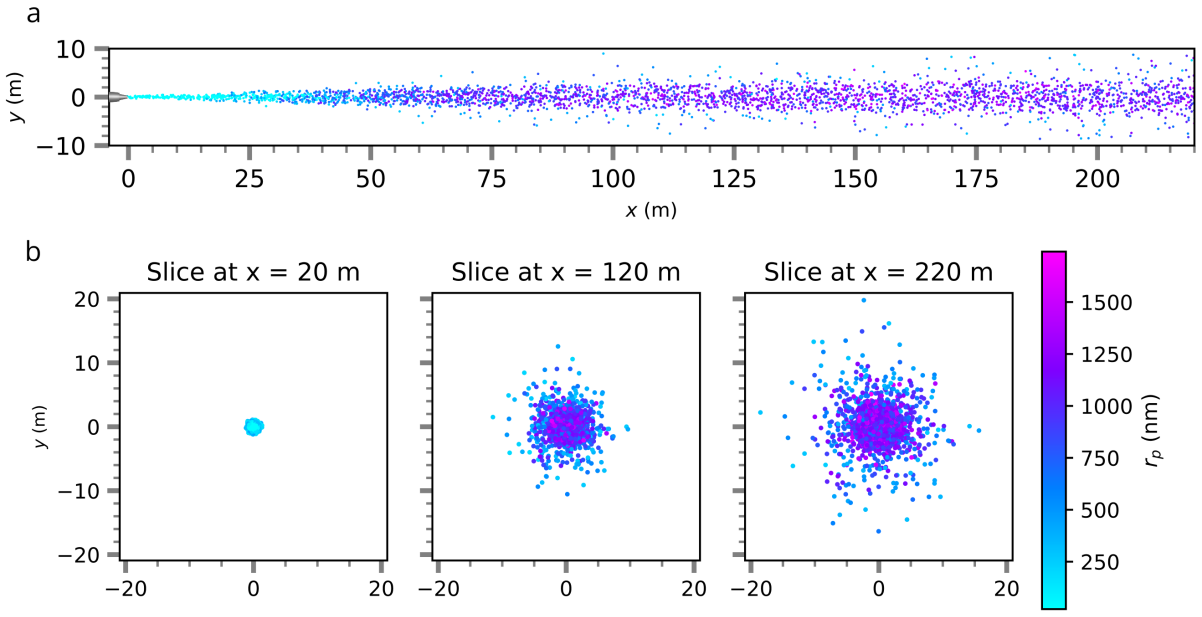

Figure 4.12 Turbulent velocity - Mean composition model : Spatial distribution of particles, colored by crystal radius. a) Side view, b) Cross-sectional distribution

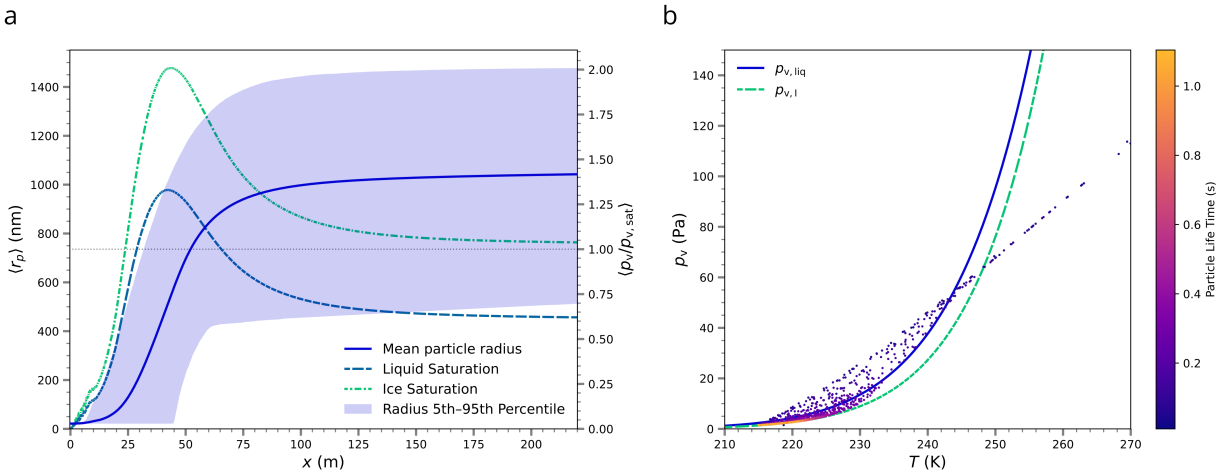

Figure 4.13 Turbulent velocity - Mean composition model : a) Evolution of the mean particle radius alongside mean saturation ratio over liquid water and over ice. b) Scatter plot of particles colored by life time in the thermodynamic diagram $T - p_{\mathrm{v}}$

4.3.3 Turbulent Velocity - Turbulent Composition

These observations motivate the introduction of the IEM mixing model presented in Section 3.2.2. This addition is expected to improve the results in two ways. First, it accounts for the instantaneous composition along particle streamlines, enabling a more accurate representation of the immediate depletion of water vapor around the particles. Additionally, the introduced variance in temperature and vapor mass fraction should better capture turbulence effects on microphysics, particularly during activation, where near-threshold conditions could result in a fraction of particles becoming activated. This implementation yields similarities to parcel models, the key difference being that mixing occurs with the local mean field state, which is itself influenced by the model, while usual parcel models exploit an input plume dilution history [29].

Figure 4.14 shows the spatial distribution of the crystal radii obtained with the new hybrid model. Contrail particles now exhibit more homogeneous radii, which can be attributed to each particle carrying its own water vapor content that evolves via a slower exchange with the ambient mean concentration. In previous simulations, ice growth was directly dictated by the local mean composition—resulting in a first-order dependence on position and larger discrepancies in crystal radii. This new behavior is physically plausible: initial ice growth is primarily driven by the engine-supplied water vapor, while subsequent evolution is governed by vapor diffusion, either by limiting the influx from supersaturated ambient regions or by controlling the rate of sublimation.

Figure 4.15 a) illustrates the evolution of the mean radius along with the 5th–95th percentile range, confirming a more homogeneous distribution and a smoother growth trend. In particular, the average saturation ratio over liquid water never exceeds unity, which can be attributed to the wide dispersion of activation times among the particles. Figure 4.15 b) further highlights the introduction of composition variance, showing a spread distribution of non-activated particles. This behavior bears qualitative similarities with LES results [14], though further tuning would be required for closer agreement.

Figure 4.16 shows the probability density function (PDF) of contrail particle radii at several downstream locations. It demonstrates a gradual transfer of non-activated soot nucleus to ice crystals with a radius of approximately 500 nm. Once the majority of particles have been activated, the PDF exhibits a slow shift towards larger radii, indicating the beginning of the diffusion-limited growth regime. The PDF observed by Khou in [22] exhibited the same transfer, confirming the qualitative behavior of the current simplified model.

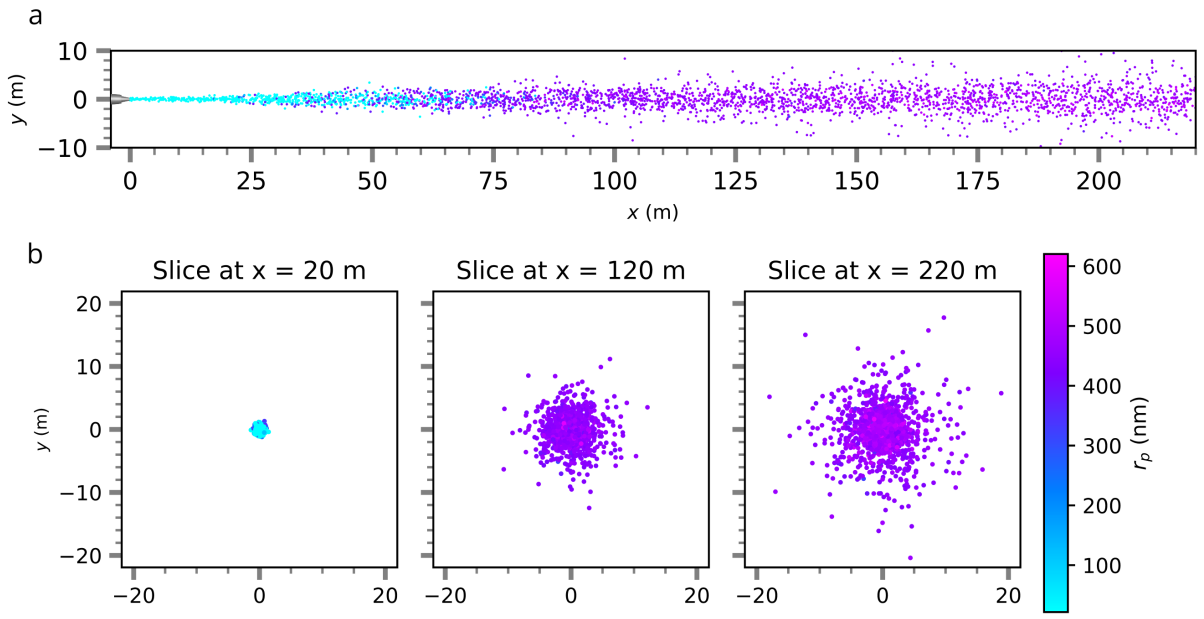

Figure 4.14 Turbulent velocity - Turbulent composition model : Spatial distribution of particles, colored by crystal radius. a) Side view, b) Cross-sectional distribution

Side-by-Side Comparison

A deeper understanding of the differences between the three models is gained through a direct comparison of their results. Figure 4.17 presents the same spatial distributions as before, but now using a uniform color scale and consistent axis limits across all cases. This visualization highlights key distinctions, such as the increased spatial dispersion of particles in the Langevin-based model and the more uniform crystal radii generated by the turbulent composition model.

Figure 4.18 shows the evolution of the number of activated particles as a function of downstream distance. In the Mean Velocity - Mean Composition model, activation occurs almost simultaneously for all particles, whereas the turbulent velocity models exhibit a more gradual activation process. This behavior is physically explained by the dispersion introduced by turbulence. Additionally, the first particles activate earlier in the turbulent cases because turbulent trajectories transport some particles to colder regions sooner than in the mean velocity case, where particles remain concentrated within the plume core. Finally, while nearly all particles are activated by $x \approx 45\,\mathrm{m}$ in both mean composition models, the Turbulent Velocity - Turbulent Composition model exhibits a delay. This can be attributed to the effect of turbulent mixing relaxation, which physically slows the mixing of composition variables.

Figure 4.19 compares the evolution of the mean particle radius in the three simulations. It

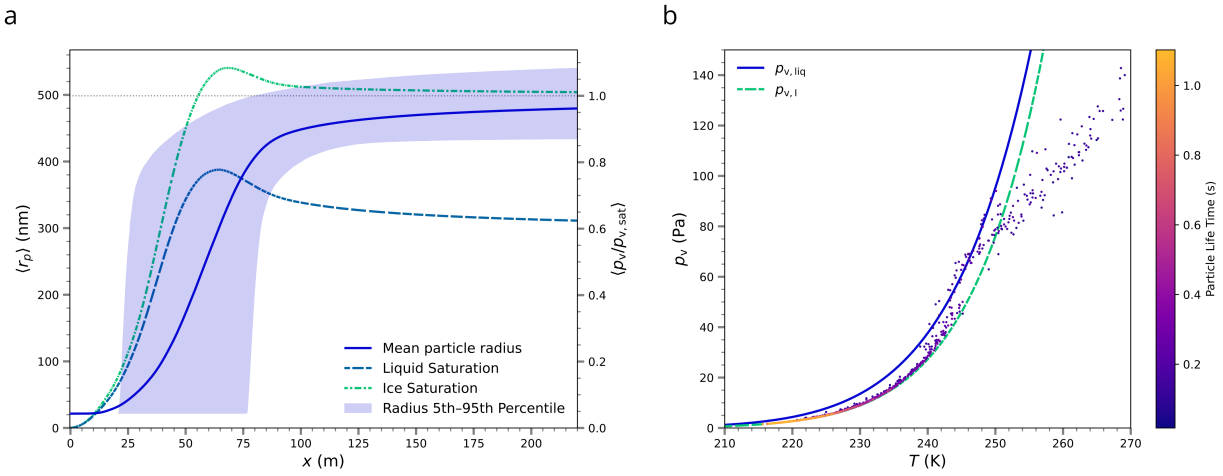

Figure 4.15 Turbulent velocity - Turbulent composition model : a) Evolution of the mean particle radius alongside mean saturation ratio over liquid water and over ice. b) Scatter plot of particles colored by life time in the thermodynamic diagram $T - p_v$

confirms the smoother initial growth in the turbulent velocity cases because of the more progressive activation of the particles. In addition, it reveals key trends. First, the Turbulent Velocity - Mean Composition model clearly overestimates particle radii. This over prediction stems from the approximation of the instantaneous particle density by the local mean density, which leads to an artificially higher availability of water vapor for ice growth. On the other hand, the Turbulent Velocity - Turbulent Composition model appears to underestimate particle radii. This highlights a limitation of the current approach: the assumption that the density of contrails particles within a given fluid volume remains relatively constant. This assumption accelerates water vapor depletion along the streamline, ultimately limiting ice particle growth.

Furthermore, since the relaxation rate toward the mean composition directly influences ice growth by compensating for vapor loss, the choice of mixing model and its associated coefficients requires further investigation.

These findings motivate the introduction of the physical particle density as an evolving composition field, similar to the vapor mass fraction and temperature, to better account for particle diffusion effects.

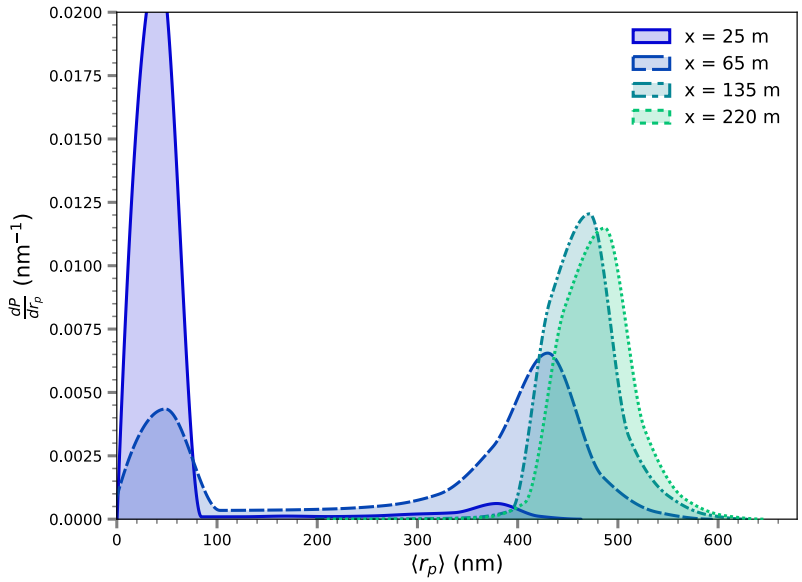

Figure 4.16 Turbulent velocity - Turbulent composition model : Probability density function of particle radii at several downstream locations

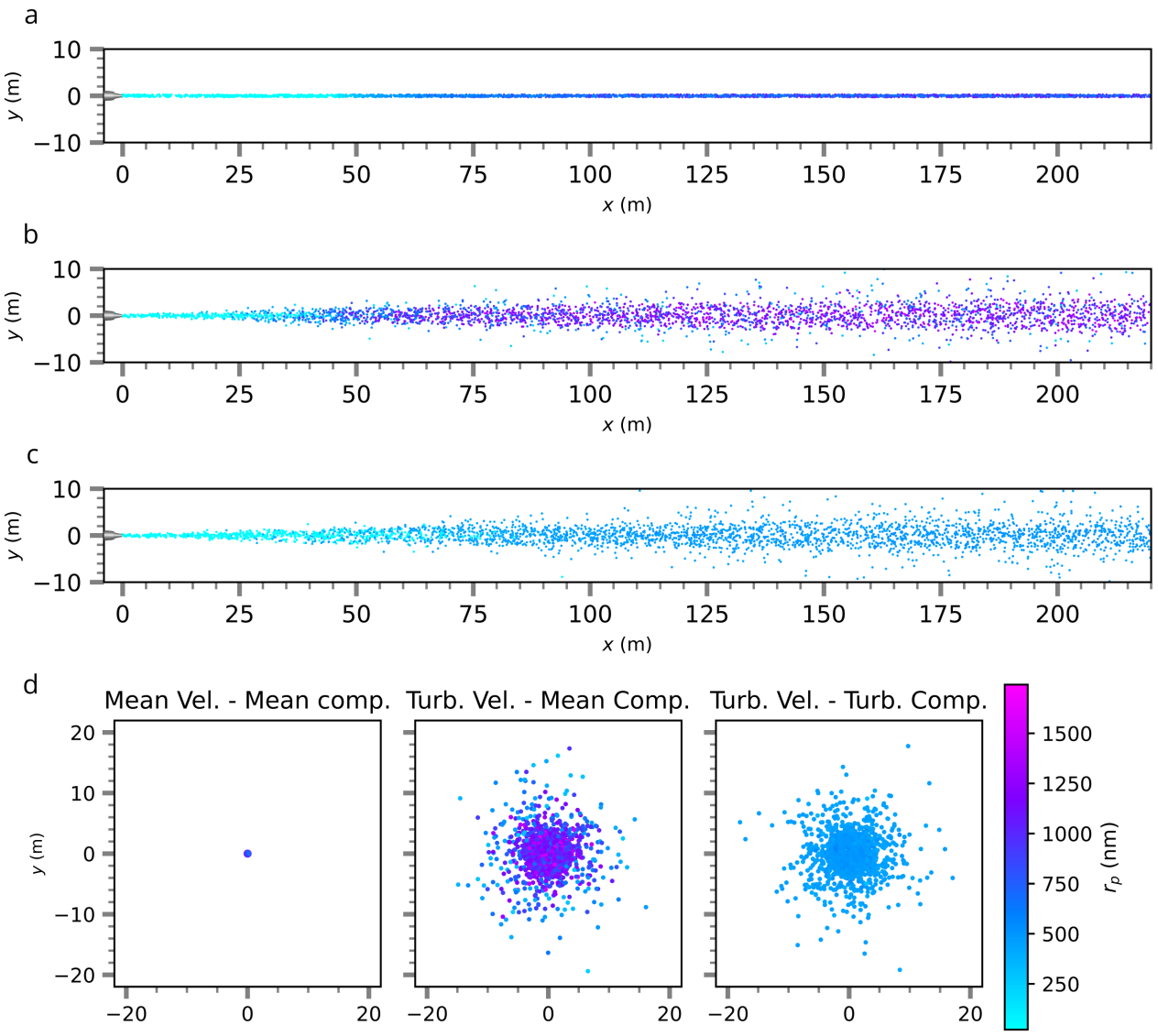

Figure 4.17 Spatial distribution of particles, colored by crystal radius. a) Mean Velocity - Mean composition b) Turbulent Velocity - Mean composition, c) Turbulent Velocity - Turbulent composition, d) Cross-sectional distribution at x=220m

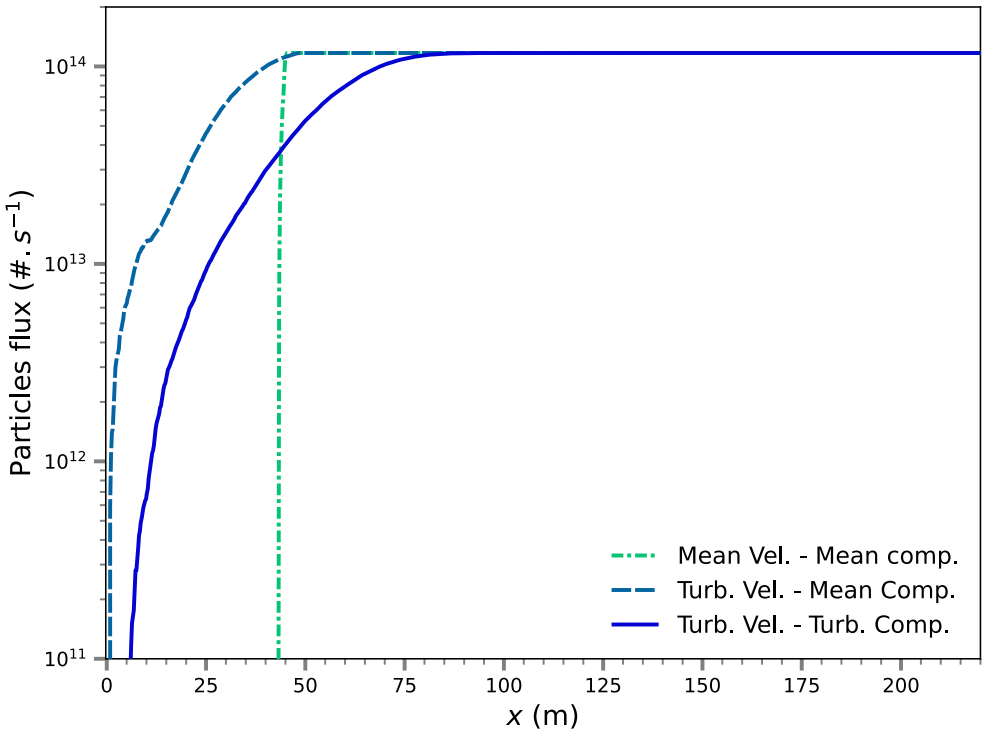

Figure 4.18 Comparison of the number of activated particles evolution for the three models

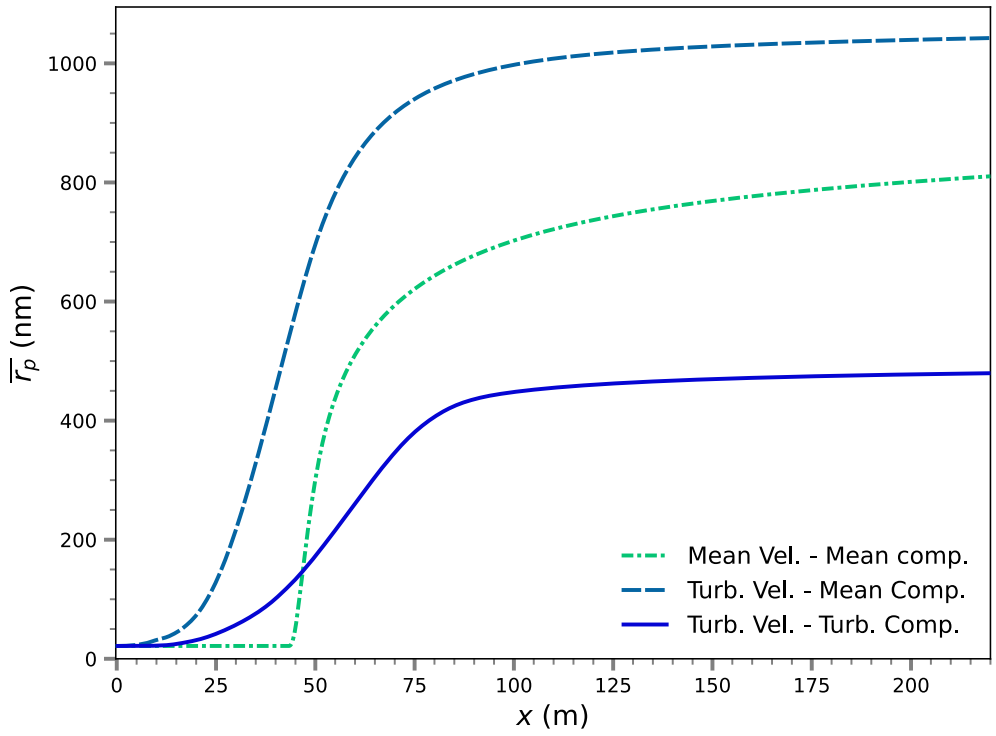

Figure 4.19 Comparison of the mean particle radius evolution for the three models

4.4 Sensitivity Studies

To assess the model ability to capture contrail formation sensitivities to physical conditions, six additional cases are simulated as variations of the reference case, using the complete stochastic model. The variations focus on three key parameters: ambient temperature T_∞, ambient relative humidity over ice (RHI), and the soot particle emission rate. A new metric, the total ice mass flux which measures the mass of ice crossing a section over time, is introduced for case-to-case comparison.

4.4.1 Cases Properties

Table 4.4 presents the variations of the three key parameters in the six additional cases considered.

Table 4.4 Sensitivity studies cases : key parameters variations

	Case Ref	Case T1	Case T2	Case R1	Case R2	Case S1	Case S2
T_∞	215K	210K	220K	215K	215K	215K	215K
RHI_∞	110%	110%	110%	100%	130%	110%	110%
$S_{\mathrm{soot}}/S_{\mathrm{soot,ref}}$	100%	100%	100%	100%	100%	80%	120%

Additionally, to reflect a realistic engineering process, the induced variations in other parameters due to the engine adapting its operating point to temperature changes are considered in cases T1 and T2. For instance, combustion efficiency improves at lower temperatures, leading to a lower total temperature at the core nozzle exhaust. This change in efficiency also affects fuel consumption, resulting in adjusted soot particle emission rates. Furthermore, ambient temperature influences the saturation pressure, leading to higher vapor mass fractions at increased temperatures. All affected parameters are listed in Table 4.5.

While most variations in airflow parameters are expected to have a second-order effect on contrail formation, particular attention should be given to differences in vapor mass fraction in both the exhaust gases and the freestream between cases, as these may contribute to the observed changes in contrail properties.

4.4.2 Soot Particles Emission Rate

First, we compare results from cases S1, Ref, and S2, in which only the soot particle emission rate was varied while all other parameters remained unchanged. The emission rates were set to 9.36×10^{13} #/s, 1.17×10^{14} #/s, and 1.40×10^{14} #/s, corresponding to deviations of -20% and +20% from the reference case at $T_\infty = 215\,\mathrm{K}$.

Table 4.5 Sensitivity studies cases : engine operating point related parameters variations

	Case T1	Case Ref	Case T2
T_∞ (K)	210	215	220
Re	1.14×10^7	1.14×10^7	1.07×10^7
ρ_∞ kg m^{-3}	0.396	0.386	0.378
μ_∞ Pa s	1.38×10^{-5}	1.41×10^{-5}	1.44×10^{-5}
Ma_∞	0.8	0.8	0.8
U_∞ m s^{-1}	232.4	235.2	237.9
$y_{\mathrm{v},\infty}$	2.015×10^{-5}	3.979×10^{-5}	7.621×10^{-5}
$p_{t,\mathrm{bp}}/p_\infty$	2.471	2.473	2.474
$T_{t,\mathrm{bp}}/T_\infty$	1.322	1.322	1.323
$p_{t,\mathrm{core}}/p_\infty$	2.324	2.329	2.333
$T_{t,\mathrm{core}}/T_\infty$	3.239	3.244	2.250
$y_{\mathrm{v,core}}$	2.06×10^{-2}	2.12×10^{-2}	2.18×10^{-2}
S_{soot} (#/s)	1.17×10^{14}	1.17×10^{14}	1.19×10^{14}
r_{soot} (nm)	19.7	21.5	22.9

Figure 4.20 presents a comparison of the mean radius of the contrail particles between the three cases at two downstream positions. As expected, a lower soot emission rate results in larger particle radii, indicating that with fewer particles, more water per particle was available for growth.

Additionally, Figure 4.21 shows the total ice mass flux through the same downstream cross sections. Although the total ice mass flux varies only weakly, it exhibits a subtle increase with the number of soot particles. This suggests that, although the same total amount of water vapor was present in all simulations, a higher initial number of condensation nuclei may slightly enhance overall ice formation efficiency.

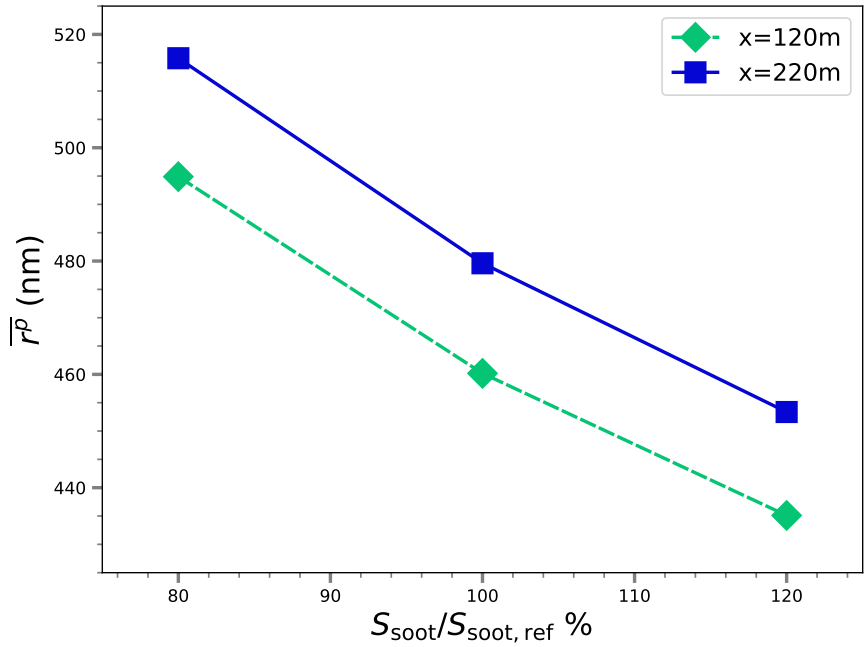

Figure 4.20 Dependence of contrail particle mean radius on soot particle emission rate at x=120m and x=220m. Cases S1, Ref and S2

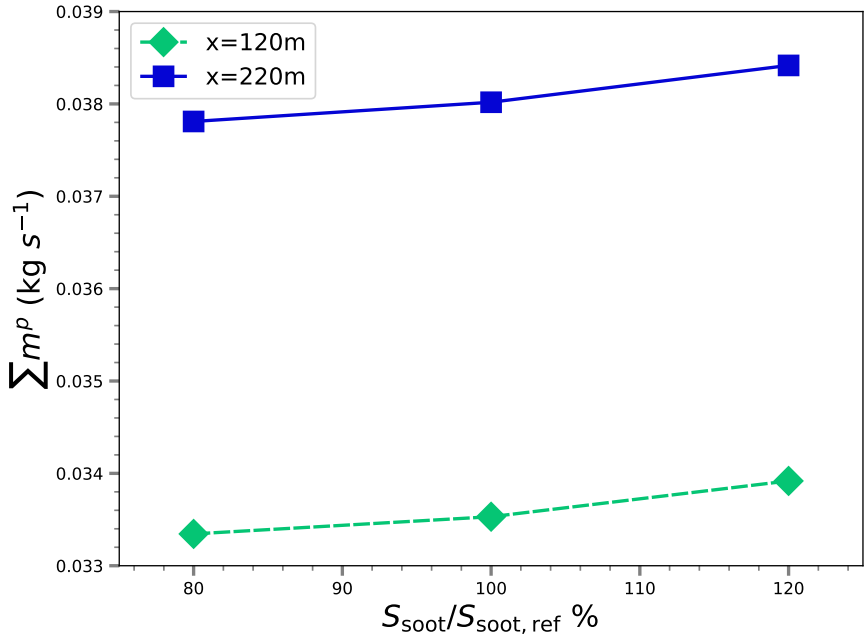

Figure 4.21 Dependence of total ice mass flux on soot particle emission rate at x=120m and x=220m. Cases S1, Ref and S2

4.4.3 Atmospheric Relative Humidity

Next, we compare results from cases R1, Ref, and R2, in which only the ambient relative humidity was varied while all other parameters remained unchanged. The corresponding ambient vapor mass fractions were set to 3.618×10^{-5} , 3.979×10^{-5} , and 4.703×10^{-5} , yielding relative humidities over ice of 100%, 110%, and 130% at $T_\infty = 215\,\mathrm{K}$.

Figure 4.22 presents a comparison of the mean radius of the contrail particles between the three cases at two downstream positions. As expected, the mean radii increase with increasing ambient RHI, as more water is made available from the freestream, leading to enhanced particle growth.

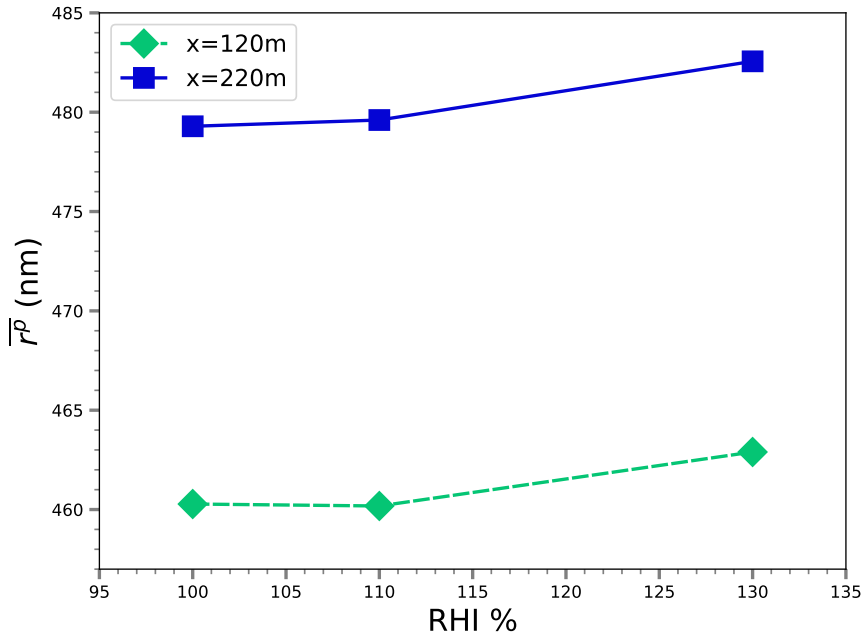

Figure 4.22 Dependence of contrail particle mean radius on freestream relative humidity over ice (RHI) at x=120m and x=220m. Cases R1, Ref and R2

Similarly, Figure 4.23 shows the total ice mass flux at the same downstream locations. Unlike the soot emission cases, the ice mass flux follows the same trend as the mean radii, increasing with ambient RHI. This behavior is expected since the same number of contrail particles is provided with more available water, allowing for greater total ice mass formation.

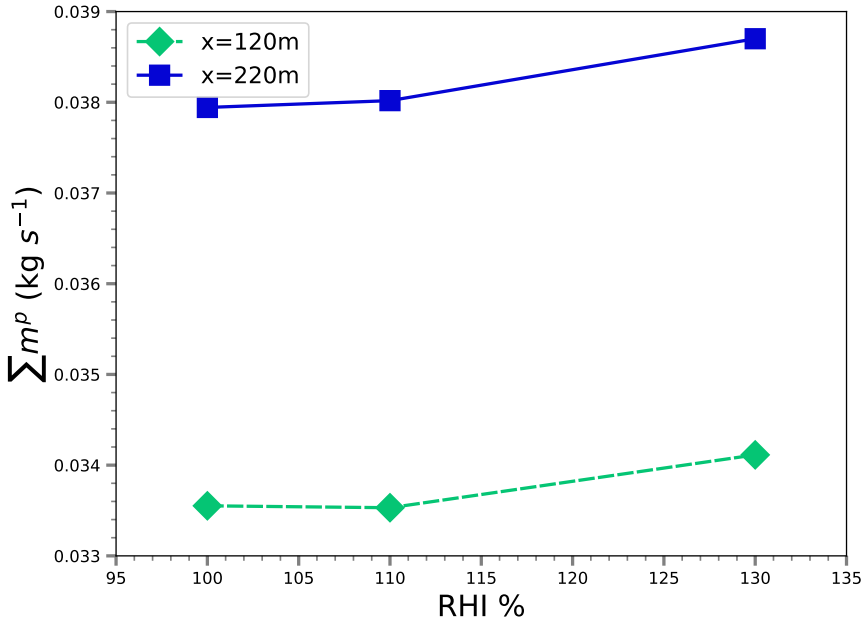

Figure 4.23 Dependence of total ice mass flux on freestream relative humidity over ice (RHI) at x=120m and x=220m. Cases R1, Ref and R2

4.4.4 Atmospheric Temperature

The impact of variations in ambient temperature is now examined by comparing the cases T1, Ref, and T2, where the freestream temperature is set to $T_\infty = 210$, 215, and $220K$, respectively. As noted earlier, these cases include additional variations in engine operating conditions, which are detailed in Table 4.5.

Figure 4.24 shows the mean radius of the contrail particles at two downstream positions for the three cases. The results indicate a strong decrease in mean radius with increasing ambient temperature. This trend is physically justified by the fact that warmer temperatures lead to a shorter thermodynamical growth range as well as a shorter effective growth period due to faster entrainment and mixing of the contrail with ambient air, reducing the time available for ice crystal growth.

Similarly, Figure 4.25 presents the total ice mass flux through two downstream cross sections. As observed in the RHI sensitivity study, the total ice mass follows the same trend as the mean radius. This is logical since the number of soot particles is nearly identical in the three cases.

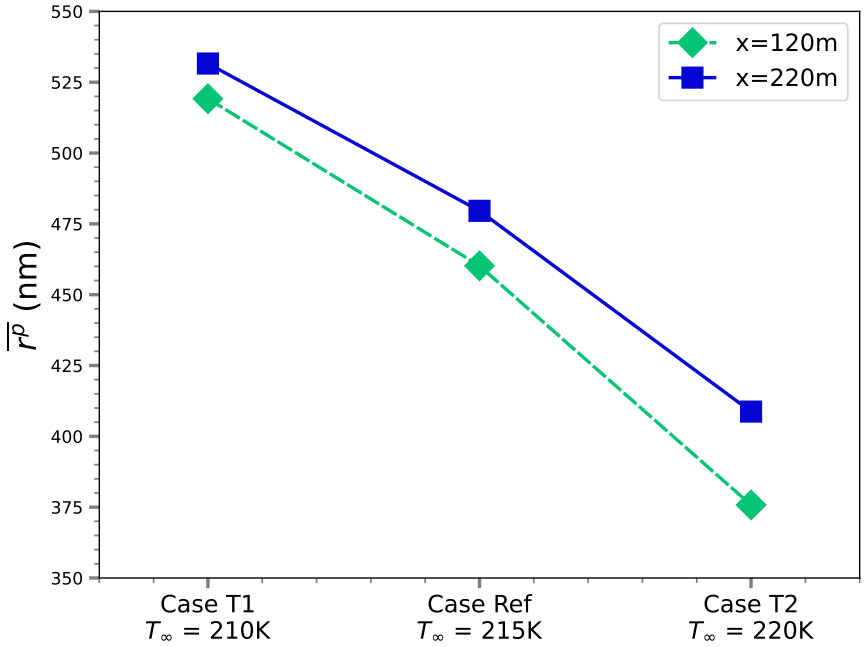

Figure 4.24 Dependence of contrail particle mean radius on freestream temperature at x=120m and x=220m. Cases T1, Ref and T2

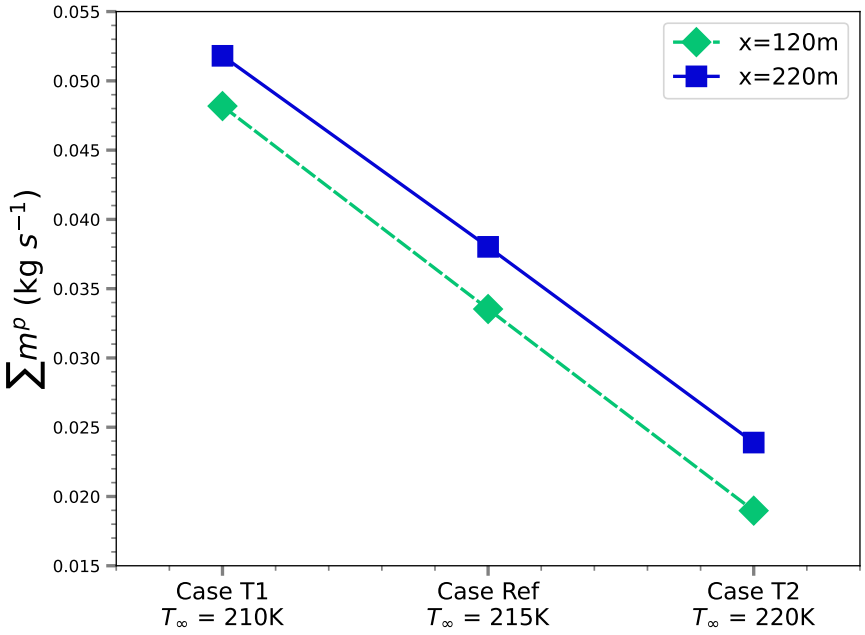

Figure 4.25 Dependence of total ice mass flux on freestream temperature at x=120m and x=220m. Cases T1, Ref and T2

4.4.5 Side-by-Side Comparison

Additional insight is gained by comparing the model sensitivity to the three parameters using consistent axis limits across all simulations.

Figure 4.26 presents the dependence of contrail particle mean radius on the three key parameters: a) soot particle emission rate, b) relative humidity over ice, and c) ambient temperature.

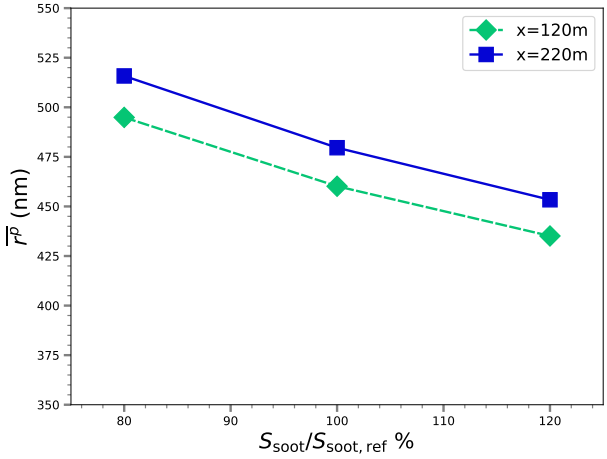

(a) Soot particles emission rate

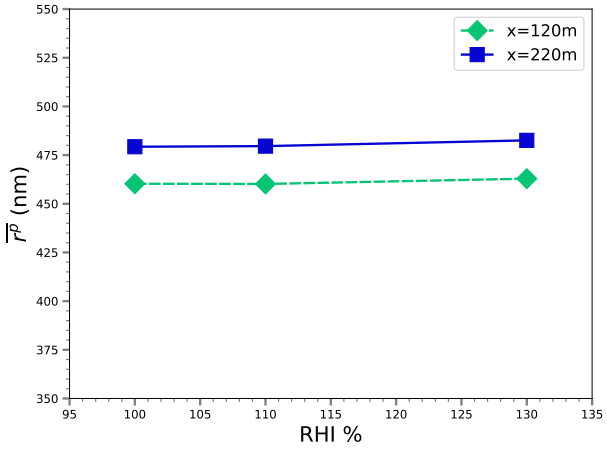

(b) Relative humidity over ice

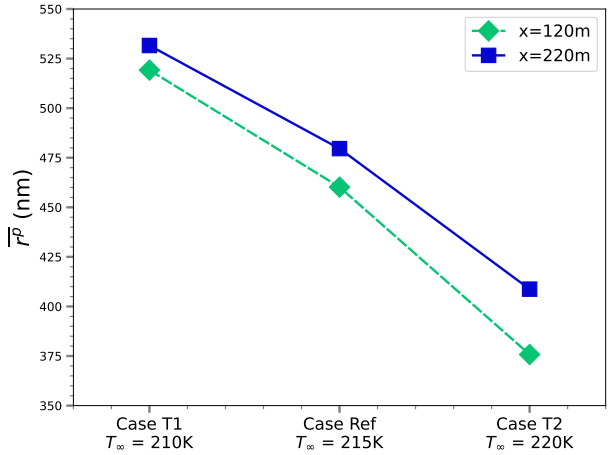

(c) Ambient temperature

Figure 4.26 Side-by-side comparison of the mean contrail particle radius dependence on the three key parameters.

Similarly, Figure 4.27 illustrates how the total ice mass flux varies with the three key parameters.

These additional comparisons highlight the greater sensitivity of early contrail formation to

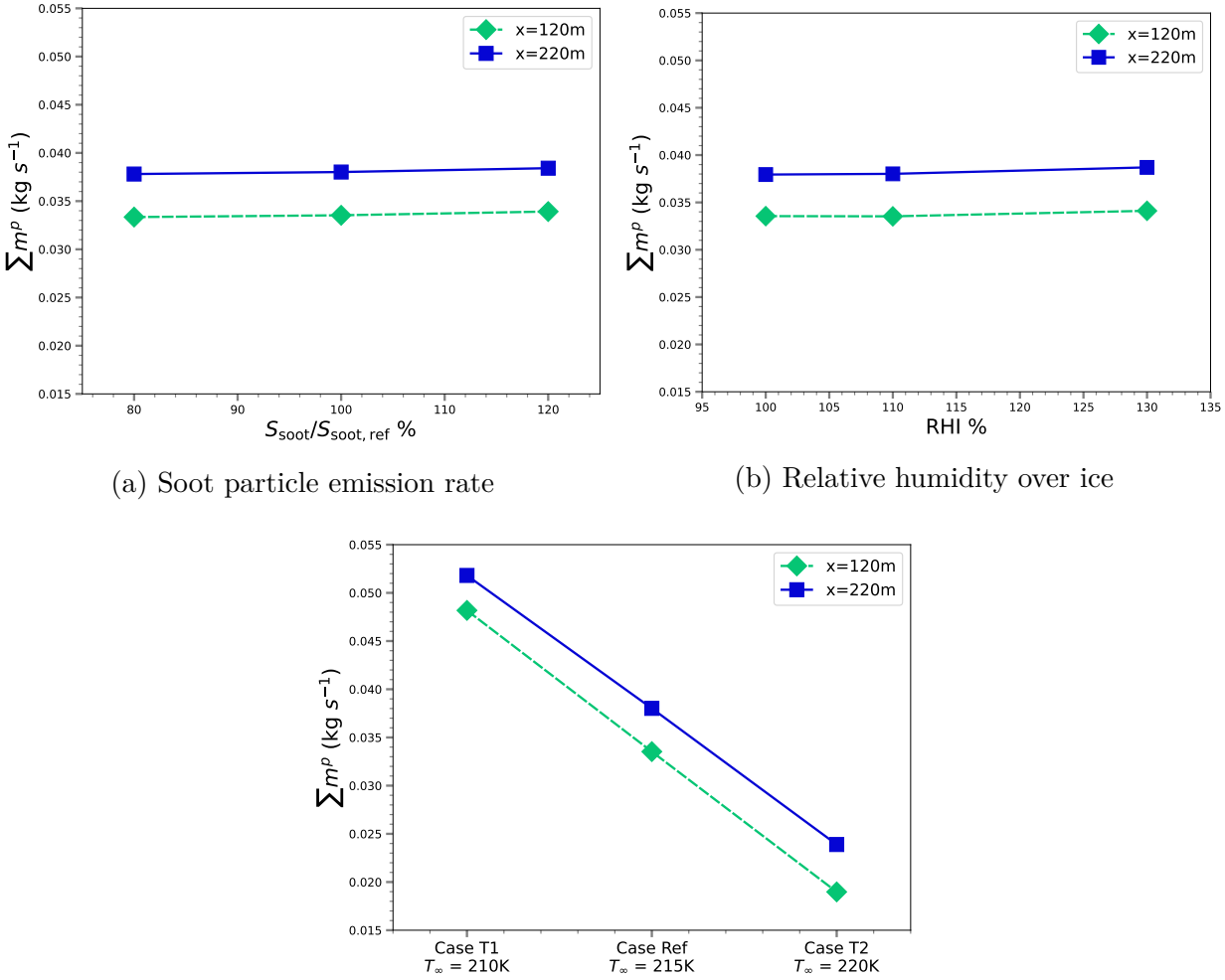

(a) Soot particle emission rate

(b) Relative humidity over ice

(c) Ambient temperature

Figure 4.27 Side-by-side comparison of the total ice mass flux dependence on the three key parameters.

ambient temperature. While, in the jet regime, relative humidity over ice (RHI) and soot particle emission rate play a lesser role compared to temperature—since growth is mainly governed by engine-supplied vapor excess—these parameters may have a more significant impact during later stages of contrail evolution. For example, although the ice mass flux remains nearly constant at this stage, a situation with more activated ice particles might lead to more effective consumption of ambient vapor as the plume starts to dilute. Similarly, the ambient saturation will have a stronger influence, as growth in the diffusion-limited regime, where saturation effects are prominent, occurs more slowly and requires longer timescales.

CHAPTER 5 CONCLUSION

5.1 Summary of Works

The overarching objective of this research is to assess the potential benefits of a stochastic approach to turbulence for modeling contrail formation in the turbulent near field of aircraft engines.

The first sub-objective is to propose a framework that accounts for the effects of turbulence on contrail microphysics with reasonable computational efficiency, thereby supporting sensitivity analysis at engineering design level. To accomplish this, a hybrid Stochastic Lagrangian-Eulerian model was developed and implemented within the CFD code CHAMPS. The model solves the RANS equations using a finite-volume solver, while the contrail particles are solved within a time-accurate Lagrangian framework. Contrail particles representing sets of potential ice nuclei are tracked using the Simplified Langevin Model, where mean flow statistics are derived from the RANS results. This approach accounts for turbulent fluctuations while keeping the overall model tractable. The fluid particle composition evolves on the basis of the Interaction by Exchange with the Mean (IEM) model, which governs how the contrail particles interact with the surrounding air and vapor. As the computational particle reaches saturation over liquid water, its physical particles begin to capture vapor from the surrounding environment, and ice begins to grow. The growth rate is computed using a detailed model, and closure is ultimately performed by providing the local mean vapor depletion term to the finite-volume solver.

The second sub-objective is to evaluate the model behavior in key mechanisms such as ice-growth activation and composition variance generation. To achieve this, different intermediate versions of the proposed framework are implemented and tested on a reference case, allowing for a comparative analysis of their predictions. In each case, the evolution of multiple computational particles is examined to assess the model response. First, the mean velocity – mean composition model confirms that the thermochemistry behaves as expected, approaching saturation equilibrium. The turbulent velocity – mean composition model then validates the performance of the Langevin equation, producing expected velocity statistics. However, this version of the model predicts contrails with unphysical properties attributed to an underestimate of the instantaneous particle density at computational particle location. Finally, the fully developed turbulent velocity – turbulent composition model successfully captures the expected evolution phases, from activation and rapid depletion of excess vapor provided by the engine to a slower growth phase limited by vapor diffusion. The results

obtained align with the numerical ranges of other frameworks, and the significant differences observed in numerical values for the same physical case further emphasize the influence of stochastic turbulence modeling.

The third sub-objective is to assess the model response to varying physical conditions, demonstrating its applicability in an engineering context. Several test cases were defined in collaboration with Safran, our industrial partner, to reflect realistic operational scenarios. The model predictions are analyzed through comparisons of the total ice mass exiting the domain and statistical descriptions of ice crystal properties, providing insights into its behavior across different conditions.

5.2 Limitations

The limitations identified throughout the previous chapters are listed below:

- The fluid particle model assumes a constant number of contrail particles within each computational particle. This leads to an overestimation of particle density further downstream, resulting in an exaggerated depletion of vapor within the fluid particle and ultimately limiting ice particle growth.
- The stochastic model employed in this study presents several constraints :
    1. The instantaneous density is approximated using the mean flow density. However, in regions near the exhaust where temperature gradients are significant, deviations from the mean may influence both particle trajectories and contrail microphysics by altering local vapor pressure.
    2. The stochastic model employed in this study determines relaxation rates based on turbulence quantities predicted by the RANS solver. As a result, it is highly dependent on the choice of turbulence model. In particular, since the k-ω SST formulation exhibits excessive turbulence decay in the freestream, the turbulence levels around particles that have escaped the jet may be underestimated, potentially affecting their interaction with the surrounding atmosphere.
- The microphysical model used in this study is simplified, particularly regarding the representation of nucleation mechanisms. The current implementation does not account for volatile aerosols or particle-chemistry interactions such as coating, coagulation, and aggregation.

- The simulations consider only the exhaust plume of a turbofan engine. In reality, the wake of the aircraft, particularly the influence of wingtip vortices, plays a role in shaping the plume and its subsequent evolution.
- The numerical implementation distributes particles between cores and nodes independently of their Eulerian region of origin. This results in multi-node communication of Eulerian statistical fields, which may pose scalability challenges if additional Eulerian fields, such as extra species, are introduced.

5.3 Future Research

The following research areas are proposed to refine hybrid stochastic Lagrangian-Eulerian modeling of contrail formation, based on the limitations identified in the current modeling approach.

- Future work should address the assumption of constant particle density by allowing it to vary locally, while also tuning the relaxation rates. This may involve exploring alternative RANS turbulence models to achieve more physically realistic turbulence levels in the freestream.
- The model could be enhanced by incorporating the actual physical particle density into the evolving composition of each fluid particle, while maintaining a constant number of particles per computational element for the Eulerian contribution. Furthermore, the microphysical model could be extended to include additional nucleation mechanisms, chemical interactions, and processes such as coating, coagulation, and aggregation.
- Extending simulations to include a full aircraft configuration would allow for the capture of wake dynamics and the influence of wingtip vortices on contrail formation, resulting in a more comprehensive representation of exhaust plume evolution.
- To improve scalability, particles should be computed locally in the Eulerian region stored in memory. Instead of exchanging full Eulerian statistical fields across nodes, only particle data would be exchanged between local domains, reducing communication overhead.
- Any extensions that leverage the flexibility of the Monte Carlo method are encouraged, as this approach readily accommodates additional stochasticity. For example, incorporating distributions for density and particle size at the nozzle exit would further refine the model.

REFERENCES

[1] R. Paoli and K. Shariff, "Contrail modeling and simulation," *Annual Review of Fluid Mechanics*, vol. 48, no. Volume 48, 2016, pp. 393–427, 2016. [Online]. Available: https://www.annualreviews.org/content/journals/10.1146/annurev-fluid-010814-013619

[2] Airports Council International and International Civil Aviation Organization, "Joint aci world-icao passenger traffic report: Trends and outlook," January 2025, accessed: 2025-03-31. [Online]. Available: https://aci.aero/2025/01/28/joint-aci-world-icao-passenger-traffic-report-trends-and-outlook/

[3] D. S. Lee *et al.*, "Aviation and global climate change in the 21st century," *Atmospheric Environment*, vol. 43, no. 22, pp. 3520–3537, 2009. [Online]. Available: https://www.sciencedirect.com/science/article/pii/S1352231009003574

[4] ——, "Uncertainties in mitigating aviation non-co_2 emissions for climate and air quality using hydrocarbon fuels," *Environmental Science: Atmospheres*, vol. 3, no. 12, pp. 1693–1740, 2023. [Online]. Available: http://dx.doi.org/10.1039/D3EA00091E

[5] R. Dischl *et al.*, "Measurements of particle emissions of an a350-941 burning 100 % sustainable aviation fuels in cruise," *Atmospheric Chemistry and Physics*, vol. 24, no. 19, pp. 11 255–11 273, 2024. [Online]. Available: https://acp.copernicus.org/articles/24/11255/2024/

[6] J. Faber and J. Király, "Potential for reducing aviation non-CO2 emissions through cleaner jet fuel," CE Delft, Tech. Rep., 2022.

[7] J. Khou *et al.*, "Cfd simulation of contrail formation in the near field of a commercial aircraft: Effect of fuel sulfur content," *Meteorologische Zeitschrift*, vol. 26, no. 6, pp. 585–596, 12 2017. [Online]. Available: http://dx.doi.org/10.1127/metz/2016/0761

[8] J. Ramsay *et al.*, "Assessing the environmental impact of aircraft/engine integration with respect to contrails," *Journal of Engineering for Gas Turbines and Power*, vol. 146, no. 11, p. 111026, 08 2024. [Online]. Available: https://doi.org/10.1115/1.4066150

[9] International Civil Aviation Organization (ICAO) and European Union Aviation Safety Agency (EASA), "Icao aircraft engine emissions databank," 2024, accessed: March 31, 2025. [Online]. Available: https://www.easa.europa.eu/en/domains/environment/icao-aircraft-engine-emissions-databank

[10] B. Kärcher, "Formation and radiative forcing of contrail cirrus," *Nature Communications*, vol. 9, no. 1, p. 1824, 2018. [Online]. Available: https://www.nature.com/articles/s41467-018-04068-0

[11] S. Cantin, M. Chouak, and F. G. and, "Eulerian–lagrangian cfd-microphysics modeling of aircraft-emitted aerosol formation at ground-level," *Aerosol Science and Technology*, vol. 58, no. 12, pp. 1347–1370, 2024. [Online]. Available: https://doi.org/10.1080/02786826.2024.2395940

[12] S. Cantin *et al.*, "Effect of nozzle chevron technology on the near-field contrail properties behind an aircraft engine using a cfd-microphysics coupling," in *Proceedings of the 25th ISABE Conference*, September 2022, accessed: 2025-03-31. [Online]. Available: https://espace2.etsmtl.ca/id/eprint/25684/

[13] S. Unterstrasser and A. Stephan, "Far field wake vortex evolution of two aircraft formation flight and implications on young contrails," *The Aeronautical Journal*, vol. 124, no. 1275, pp. 667–702, May 2020, publisher: Cambridge University Press. [Online]. Available: https://www.cambridge.org/core/journals/aeronautical-journal/article/far-field-wake-vortex-evolution-of-two-aircraft-formation-flight-and-implications-on-young-contrails/0CAAB32CF84A8A763018F4DEF7E4598E#figures

[14] R. Paoli *et al.*, "Effects of jet/vortex interaction on contrail formation in supersaturated conditions," *Physics of Fluids*, vol. 25, no. 5, p. 053305, 05 2013. [Online]. Available: https://doi.org/10.1063/1.4807063

[15] S. B. Pope, "Simple models of turbulent flowsa)," *Physics of Fluids*, vol. 23, no. 1, p. 011301, 01 2011. [Online]. Available: https://doi.org/10.1063/1.3531744

[16] R. R. Cao, S. B. Pope, and A. R. Masri, "Turbulent lifted flames in a vitiated coflow investigated using joint pdf calculations," *Combustion and Flame*, vol. 142, no. 4, pp. 438–453, 2005. [Online]. Available: https://www.sciencedirect.com/science/article/pii/S0010218005001173

[17] A. Krisman *et al.*, "A dns evaluation of mixing models for transported pdf modelling of turbulent nonpremixed flames," *Combustion and Flame*, vol. 161, no. 8, pp. 2085–2106, 2014. [Online]. Available: https://www.sciencedirect.com/science/article/pii/S0010218014000145

[18] H. Zhou *et al.*, "Investigation of mixing model performance in transported pdf calculations of turbulent lean premixed jet flames through lagrangian statistics and

sensitivity analysis," *Combustion and Flame*, vol. 181, pp. 136–148, 2017. [Online]. Available: https://www.sciencedirect.com/science/article/pii/S0010218017301037

[19] A. T. Norris, "Modeling of cavity residence time via modeled lagrangian particle tracking," in *Proceedings of the December 2023 Joint Army-Navy-NASA-Air Force (JANNAF) Meeting*, December 2023, accessed: 2025-03-31. [Online]. Available: https://ntrs.nasa.gov/citations/20230015773

[20] S. Cantin *et al.*, "Eulerian–lagrangian cfd-microphysics modeling of a near-field contrail from a realistic turbofan," *International Journal of Engine Research*, vol. 23, no. 4, pp. 661–677, 2022. [Online]. Available: https://doi.org/10.1177/1468087421993961

[21] R. Paoli *et al.*, "Large-eddy simulation of a turbulent jet and a vortex sheet interaction: Particle formation and evolution in the near field of an aircraft wake," *Meteorologische Zeitschrift*, vol. 17, pp. 131–144, 04 2008.

[22] J.-C. Khou, "Modélisation des traînées de condensation par interaction entre l'aérodynamique, la cinétique chimique et la microphysique," Theses, Université Pierre et Marie Curie - Paris VI, Jun. 2016. [Online]. Available: https://theses.hal.science/tel-01403100

[23] D. M. Murphy and T. Koop, "Review of the vapour pressures of ice and supercooled water for atmospheric applications," *Quarterly Journal of the Royal Meteorological Society*, vol. 131, no. 608, pp. 1539–1565, 2005. [Online]. Available: https://rmets.onlinelibrary.wiley.com/doi/abs/10.1256/qj.04.94

[24] M. Z. Jacobson, *Fundamentals of Atmospheric Modeling*. Cambridge University Press, 1999, google-Books-ID: QnzHkFN3v8AC.

[25] D. C. Lewellen, "Analytic solutions for evolving size distributions of spherical crystals or droplets undergoing diffusional growth in different regimes," *Journal of the Atmospheric Sciences*, vol. 69, no. 2, pp. 417 – 434, 2012. [Online]. Available: https://journals.ametsoc.org/view/journals/atsc/69/2/jas-d-11-029.1.xml

[26] H. R. Pruppacher and J. D. Klett, *Microphysics of Clouds and Precipitation*, 2nd ed. Springer, 1997. [Online]. Available: https://books.google.fr/books?id=Nk40jwEACAAJ

[27] P. M. Winkler *et al.*, "Condensation of water vapor: Experimental determination of mass and thermal accommodation coefficients," *Journal of Geophysical Research: Atmospheres*, vol. 111, no. D19, 2006. [Online]. Available: https://agupubs.onlinelibrary.wiley.com/doi/abs/10.1029/2006JD007194

[28] B. N. Hale and P. L. M. Plummer, "Molecular model for ice clusters in a supersaturated vapor," *The Journal of Chemical Physics*, vol. 61, no. 10, pp. 4012–4019, 11 1974. [Online]. Available: https://doi.org/10.1063/1.1681694

[29] B. Kärcher and F. Yu, "Role of aircraft soot emissions in contrail formation," *Geophysical Research Letters*, vol. 36, no. 1, 2009. [Online]. Available: https://agupubs.onlinelibrary.wiley.com/doi/abs/10.1029/2008GL036649

[30] J.-C. Khou *et al.*, "Spatial simulation of contrail formation in near-field of commercial aircraft," *Journal of Aircraft*, vol. 52, no. 6, pp. 1927–1938, 2015. [Online]. Available: https://doi.org/10.2514/1.C033101

[31] F. Garnier *et al.*, "Engine emission alteration in the near field of an aircraft," *Atmospheric Environment*, vol. 31, no. 12, pp. 1767–1781, 1997. [Online]. Available: https://www.sciencedirect.com/science/article/pii/S1352231096003299

[32] R. Paoli and H. Moet, "Temporal large-eddy simulations of the near-field of an aircraft wake," *Open J. Fluid Dyn.*, vol. 08, no. 02, pp. 161–180, 2018. [Online]. Available: https://doi.org/10.4236/ojfd.2018.82012

[33] D. Kolomenskiy, R. Paoli, and J.-F. Boussuge, "Hybrid rans–les simulation of wingtip vortex dynamics," in *Proceedings of the 29th Congress of the International Council of the Aeronautical Sciences (ICAS)*, 2014, accessed: 2025-03-31. [Online]. Available: https://www.researchgate.net/publication/266379175_Hybrid_RANS-LES_simulation_of_wingtip_vortex_dynamics

[34] D. Kolomenskiy and R. Paoli, "Numerical simulation of the wake of an airliner," *Journal of Aircraft*, vol. 55, no. 4, pp. 1689–1699, 2018. [Online]. Available: https://doi.org/10.2514/1.C034349

[35] I. Sölch and B. Kärcher, "A large-eddy model for cirrus clouds with explicit aerosol and ice microphysics and lagrangian ice particle tracking," *Quarterly Journal of the Royal Meteorological Society*, vol. 136, no. 653, pp. 2074–2093, 2010. [Online]. Available: https://rmets.onlinelibrary.wiley.com/doi/abs/10.1002/qj.689

[36] T. Bräuer *et al.*, "Airborne measurements of contrail ice properties—dependence on temperature and humidity," *Geophysical Research Letters*, vol. 48, no. 8, p. e2020GL092166, 2021, e2020GL092166 2020GL092166. [Online]. Available: https://agupubs.onlinelibrary.wiley.com/doi/abs/10.1029/2020GL092166

[37] T. Bräuer *et al.*, "Reduced ice number concentrations in contrails from low-aromatic biofuel blends," *Atmospheric Chemistry and Physics*, vol. 21, no. 22, pp. 16 817–16 826, 2021. [Online]. Available: https://acp.copernicus.org/articles/21/16817/2021/

[38] C. Voigt *et al.*, "Cleaner burning aviation fuels can reduce contrail cloudiness," *Commun. Earth Environ.*, vol. 2, no. 1, Jun. 2021.

[39] H. Wang and S. B. P. and, "Lagrangian investigation of local extinction, re-ignition and auto-ignition in turbulent flames," *Combustion Theory and Modelling*, vol. 12, no. 5, pp. 857–882, 2008. [Online]. Available: https://doi.org/10.1080/13647830802056137

[40] J. Blazek, *Computational Fluid Dynamics: Principles and Applications: Third Edition*. Elsevier Science, Jan. 2001, journal Abbreviation: Computational Fluid Dynamics: Principles and Applications Publication Title: Computational Fluid Dynamics: Principles and Applications.

[41] F. Menter, "Zonal two equation k-w turbulence models for aerodynamic flows," in *23rd Fluid Dynamics, Plasmadynamics, and Lasers Conference*. Reston, Virigina: American Institute of Aeronautics and Astronautics, Jul. 1993.

[42] B. J. Delarue and S. B. Pope, "Application of pdf methods to compressible turbulent flows," *Physics of Fluids*, vol. 9, no. 9, pp. 2704–2715, 09 1997. [Online]. Available: https://doi.org/10.1063/1.869382

[43] D. C. Haworth and S. B. Pope, "A generalized langevin model for turbulent flows," *The Physics of Fluids*, vol. 29, no. 2, pp. 387–405, 02 1986. [Online]. Available: https://doi.org/10.1063/1.865723

[44] S. B. Pope, *Turbulent flows*. Cambridge ; New York: Cambridge University Press, 2000.

[45] P. Jenny *et al.*, "Pdf simulations of a bluff-body stabilized flow," *Journal of Computational Physics*, vol. 169, no. 1, pp. 1–23, 2001. [Online]. Available: https://www.sciencedirect.com/science/article/pii/S002199910196704X

[46] M. M. Rogers and R. D. Moser, "Direct simulation of a self-similar turbulent mixing layer," *Physics of Fluids*, vol. 6, no. 2, pp. 903–923, 02 1994. [Online]. Available: https://doi.org/10.1063/1.868325

[47] S. Pope, "Pdf methods for turbulent reactive flows," *Progress in Energy and Combustion Science*, vol. 11, no. 2, pp. 119–192, 1985. [Online]. Available: https://www.sciencedirect.com/science/article/pii/0360128585900024

[48] M. Muradoglu, S. B. Pope, and D. A. Caughey, "The hybrid method for the pdf equations of turbulent reactive flows: Consistency conditions and correction algorithms," *Journal of Computational Physics*, vol. 172, no. 2, pp. 841–878, 2001. [Online]. Available: https://www.sciencedirect.com/science/article/pii/S0021999101968615

[49] "Chapel: Productive Parallel Programming." [Online]. Available: https://chapel-lang.org/

[50] M. Parenteau *et al.*, "Development of parallel CFD applications with the chapel programming language," in *AIAA Scitech 2021 Forum*. Reston, Virginia: American Institute of Aeronautics and Astronautics, Jan. 2021.

[51] M. K. Zayni, M. Blanchet, and E. Laurendeau, "Lagrangian particle tracking for ice accretion applications," in *AIAA AVIATION FORUM AND ASCEND 2024*. Reston, Virginia: American Institute of Aeronautics and Astronautics, Jul. 2024.

[52] P. Roe, "Approximate riemann solvers, parameter vectors, and difference schemes," *Journal of Computational Physics*, vol. 43, no. 2, pp. 357–372, 1981. [Online]. Available: https://www.sciencedirect.com/science/article/pii/0021999181901285

[53] H. Papillon Laroche, E. Radenac, and E. Laurendeau, "Stochastic ice accretion model using an unstructured advancing front technique," *International Journal of Multiphase Flow*, vol. 163, p. 104420, 2023. [Online]. Available: https://www.sciencedirect.com/science/article/pii/S0301932223000435

[54] W. Press, *Numerical Recipes 3rd Edition: The Art of Scientific Computing*, ser. Numerical Recipes: The Art of Scientific Computing. Cambridge University Press, 2007. [Online]. Available: https://books.google.fr/books?id=1aAOdzK3FegC

[55] T. Rendall and C. Allen, "Finite-volume droplet trajectories for icing simulation," *International Journal of Multiphase Flow*, vol. 58, pp. 185–194, Jan. 2014. [Online]. Available: https://linkinghub.elsevier.com/retrieve/pii/S0301932213001262

[56] A. Haselbacher, F. Najjar, and J. Ferry, "An efficient and robust particle-localization algorithm for unstructured grids," *Journal of Computational Physics*, vol. 225, no. 2, pp. 2198–2213, 2007. [Online]. Available: https://www.sciencedirect.com/science/article/pii/S002199910700126X

[57] J. Crank and P. Nicolson, "A practical method for numerical evaluation of solutions of partial differential equations of the heat-conduction type," *Mathematical Proceedings of the Cambridge Philosophical Society*, vol. 43, no. 1, p. 50–67, 1947.

[58] R. Courant, K. Friedrichs, and H. Lewy, "On the partial difference equations of mathematical physics," *IBM Journal of Research and Development*, vol. 11, no. 2, pp. 215–234, 1967.

[59] "Turbulence Modeling Resource." [Online]. Available: https://turbmodels.larc.nasa.gov/index.html

[60] D. C. Jespersen, T. H. Pulliam, and M. L. Childs, "OVERFLOW turbulence modeling resource validation results," NASA Ames Research Center, Tech. Rep. NAS-2016-01, 2016.

[61] R. Bush, G. Power, and C. Towne, *WIND - The production flow solver of the NPARC Alliance*, ser. Aerospace Sciences Meetings. American Institute of Aeronautics and Astronautics, Jan. 1998. [Online]. Available: https://arc.aiaa.org/doi/10.2514/6.1998-935

[62] T. M. Young, "International standard atmosphere (isa) table," in *Performance of the Jet Transport Airplane: Analysis Methods, Flight Operations, and Regulations*. Wiley, 2018, pp. 583–590. [Online]. Available: https://onlinelibrary.wiley.com/doi/abs/10.1002/9781118534786.app1

[63] W. S. and, "Lii. the viscosity of gases and molecular force," *The London, Edinburgh, and Dublin Philosophical Magazine and Journal of Science*, vol. 36, no. 223, pp. 507–531, 1893. [Online]. Available: https://doi.org/10.1080/14786449308620508

[64] "Fidelity Pointwise User Manual." [Online]. Available: https://www.pointwise.com/user-manual/

[65] V. Liguori, "Analysis and implementation of the coupled and encapsulated selective frequency damping method," Master's thesis, Polytechnique Montréal, avril 2021. [Online]. Available: https://publications.polymtl.ca/6281/

[66] E. Murakami and D. Papamoschou, "Mean flow development in dual-stream compressible jets," *AIAA Journal*, vol. 40, no. 6, pp. 1131–1138, 2002. [Online]. Available: https://doi.org/10.2514/2.1762

[67] R. Xu *et al.*, "A physics-based approach to modeling real-fuel combustion chemistry – ii. reaction kinetic models of jet and rocket fuels," *Combustion and Flame*, vol. 193, pp. 520–537, 2018. [Online]. Available: https://www.sciencedirect.com/science/article/pii/S0010218018301317

[68] A.-. A. N. M. A. E. Modeling, *Procedure for the Calculation of Aircraft Emissions*, Jul. 2009. [Online]. Available: https://doi.org/10.4271/AIR5715

[69] T. A. Sipkens and J. C. Corbin, "Effective density and packing of compacted soot aggregates," *Carbon*, vol. 226, p. 119197, Jun. 2024. [Online]. Available: https://www.sciencedirect.com/science/article/pii/S0008622324004160